Available online at www.sciencedirect.com
ScienceDirect
Nuclear Physics B Proceedings Supplement 00 (2015) 1–40
Nuclear Physics B Proceedings Supplement

NLO corrections to processes with electroweak bosons at hadron colliders

F. Campanario[b], M. Kerner[a,c], L. D. Ninh[a,d], M. Rauch[a], R. Roth[a], D. Zeppenfeld[a]

[a] *Institute for Theoretical Physics, Karlsruhe Institute of Technology (KIT), 76128 Karlsruhe, Germany*
[b] *Theory Division, IFIC, University of Valencia-CSIC, E-46980 Paterna, Valencia, Spain*
[c] *Max Planck Institute for Physics, Föhringer Ring 6, D-80805 München, Germany*
[d] *Humboldt-Universität zu Berlin, Institut für Physik, Newtonstraße 15, D-12489 Berlin, Germany*

Abstract

For many processes with electroweak bosons in the final state, next-to-leading order QCD and, in some cases, electroweak corrections have been calculated for differential cross sections at hadron colliders. The calculational techniques and some phenomenological implications are reviewed in this contribution. Processes discussed include vector boson fusion and vector boson scattering, production of two and three electroweak bosons, potentially with jets, (VVj, $VVjj$ and VVV events) and some Higgs production processes. All QCD corrections are implemented in the publicly available `VBFNLO` program package.

Keywords: LHC phenomenology, NLO QCD and electroweak corrections, Gauge boson and Higgs production

1. Introduction

The Large Hadron Collider (LHC) at CERN, Geneva, will provide a wealth of information on physics at the energy frontier in coming years. During the next decade or longer, proton-proton scattering at a center-of-mass energy of 13 to 14 TeV will provide insight into the nature of the Higgs boson discovered at 125 GeV. It will allow to test Standard Model (SM) predictions in a new energy domain and it may possibly find hints for new physics beyond the SM. However, the hadronic nature of the LHC beams and the energy regime pose an extraordinary level of complexity both at the experimental and the theoretical level. Searches for new physics signatures will often involve the production of multiple particles in the final state, consisting of jets, leptons, photons and missing energy. Coherent searches will require not only a precise knowledge of the signals, but also of all the SM model backgrounds with the same or experimentally similar final states. However, theoretical predictions suffer from severe uncertainties in their normalization and their kinematical dependencies, if limited to leading order (LO) approximation in the perturbative series expansion. Thus, theoreticians face the challenge of providing results for many processes at next-to-leading order (NLO) accuracy in the strong coupling constant, and in many cases also electroweak corrections are needed. For a long time, these NLO corrections were only accessible for at most three particles in the final state. In the last decade, the field has experienced an enormous progress and NLO cross section calculations for processes with an unprecedented level of complexity have been performed.

To this program we have contributed within the B5 project, with predictions for a host of processes relevant at the LHC. In this chapter, we will review these calculations and some of their phenomenological implications. Broadly speaking, the calculations have been focused on processes with several electroweak bosons, either in the final state or in t-channel exchange. Examples for the latter are vector boson fusion (VBF) and vector boson scattering (VBS) processes, i.e. quark-(anti)quark scattering via t-channel W or Z exchange with a Higgs boson or up to two electroweak gauge bosons being emitted off the t-channel exchange. The calculation of NLO QCD corrections to distributions for Higgs production via VBF [1] stood at the beginning of our program of improving predictions for multi-parton cross sections,

and it has provided the name for the program package, VBFNLO, which has been developed over the years to make the results of our efforts available to the physics community [2, 3].

Higgs production via VBF is a promising process at the LHC to measure the spin and *CP*-properties of the recently discovered 125 GeV resonance and to measure its couplings to vector bosons and fermions. We will use this process in Section 2 for a somewhat pedagogical introduction into the calculational methods which we employ for NLO QCD corrections. All the calculations presented in this review use the Catani-Seymour subtraction method [4]. VBF Higgs, W or Z production and all vector boson scattering processes exhibit identical (and particularly simple) structures for the subtraction of infrared and collinear divergences from the real emission graphs, which will be discussed in Section 2. Beyond a review of the calculations we will also discuss phenomenological aspects of VBF and VBS processes in Section 3.1. For Higgs production in VBF, we will focus on the on-shell production mode, but results including the most relevant decay channels have also been studied and provided. Additionally, to facilitate the discrimination of the SM versus beyond SM (BSM) scenarios, we have studied the effect of introducing anomalous couplings (AC). These anomalous couplings parametrize BSM physics through higher dimensional operators and they are an excellent method to constrain and set limits on new physics effects. Anomalous couplings are implemented in VBFNLO. The choice of basis and operators will be described in Section 2.6.

VBS is one representative of a class of processes which will play an important role at the LHC, namely electroweak di-boson production in association with two jets, which we generically call $VVjj$ production in the following. These processes not only are backgrounds when searching for signals of BSM physics but also to SM searches. For example, $WWjj$ production is an irreducible background of Hjj production, with the Higgs boson decaying into two (potentially virtual) W bosons. On the other hand, $VVjj$ production is interesting as a signal process. In the form of vector boson scattering, $VV \to VV$, it is sensitive to triple and quartic gauge couplings, thereby providing us with an excellent way to understand the electroweak (EW) sector of the SM and possibly to get hints of physics beyond the SM.

There are two mechanisms to produce EW di-boson plus two jet events at the LHC. The first mechanism is EW-induced of order $O\left(\alpha^4\right)$ (for on-shell vector boson production), which can be further classified into the $t-$channel VBF or VBS contributions and tri-boson production with a hadronic decay of one of the vector bosons. For the former class, results have been provided at NLO QCD for all the production modes [5–10], including the leptonic decays of the weak bosons and spin correlations, with the exception of $Z\gamma jj$ production, for which results are in progress. AC have been taken into account for a large fraction of the processes and sensitivity studies have been performed. Additionally, for selected processes, spin-2 resonances, Kaluza-Klein excitations (as manifestations of spin-1 resonances) and two Higgs models have been considered. The VBF and VBS processes will be reviewed in Section 3.1.

The second production mechanism of $VVjj$ events is the QCD-induced mechanism of order $O\left(\alpha_s^2\alpha^2\right)$ (for on-shell production) [11–21]. We have contributed to the program of calculating the differential cross sections for these processes, including the leptonic decays of the vector bosons and all off-shell and spin-correlation effects. Predictions for the $W^\pm Zjj$, $W^\pm\gamma jj$, $W^\pm W^\pm jj$, $ZZjj$ and $Z\gamma jj$ production processes have been provided and the codes are available in the VBFNLO program package [14, 15, 18, 20, 21]. They constitute background channels to the EW-induced mechanisms. Technically, they are the most difficult to compute due to the occurrence of six-point one-loop integrals up to rank 5 and complicated real-emission processes. NLO QCD corrections to QCD-induced $VVjj$ production will be discussed in Section 3.2.

Tri-boson production processes are by themselves of great relevance at the LHC. They give rise to multi-lepton signatures, possibly accompanied by missing transverse energy or photons, or also both of them, which are a background to many new-physics searches, e.g. in supersymmetry, where the decay cascades of the supersymmetric particles lead to final states with leptons and missing transverse energy. Processes with photons appear in gauge-mediated supersymmetry breaking scenarios, where for example the lightest neutralino can be the next-to-lightest supersymmetric particle and will then decay into a photon plus a gravitino, which manifests itself as missing energy [22, 23]. But tri-boson production is also important as a signal process in its own right. The appearance of triple and quartic gauge couplings allows to study anomalous couplings and either discover or constrain their size. We have provided results at NLO QCD for all tri-boson processes. First, they were computed considering the leptonic decay channels of the vector bosons [24–29], and, recently, within certain approximations [30], with a hadronic decay of one of the vector bosons. This important class of processes is reviewed in Section 3.3. The NLO corrections turn out to be par-

ticularly large for these processes, and in general, for processes with a color singlet final state at LO. At NLO, new partonic sub-processes appear as part of the real corrections, accessing the enhanced gluon parton distribution functions (PDFs) and resulting in large corrections to the total cross section. Additionally, new kinematical configurations open up, as for example, one hard jet recoiling against the electroweak system, with possible soft and collinear weak boson emissions, yielding the well known large Sudakov logarithms, and resulting in large corrections in the tails of relevant differential distributions.

At this point, we would like to stress that the best prediction for $VVjj$ production channels at NLO QCD can be obtained, within the `VBFNLO` program, by summing the VBF, tri-boson with one hadronic decay and QCD-induced mechanisms. The interferences between these three channels are not included since they are separately calculated. These effects are cut dependent, but generally small for most analyses. The maximal interference effects are expected for the same-sign $W^\pm W^\pm jj$ process where the gluon-induced sub-processes are absent at LO and only the left-chiral fermions contribute. Here, the LO interference between the EW and QCD induced mechanisms can be as large as 10%.

In Section 3.4, results for several multi-boson production processes in association with one jet will be reviewed, in particular for $W^\pm Hj$, W^+W^-j, WZj, $W^\pm\gamma j$ and $W^\pm\gamma\gamma j$ [31–37] production. Multi-boson plus one-jet inclusive samples are important for several reasons. First, one-jet events are responsible for the large NLO corrections at the integrated and differential level for processes with color singlet final states at LO – among them the tri-boson production processes as discussed above. Thus, studying one-jet events at NLO provides an essential piece of the NNLO corrections of the corresponding processes without a jet, namely, the double real and virtual-real contributions to them. Furthermore, it allows us to study the convergence of perturbation theory: As the jet multiplicity of a given production mode increases, more partonic sub-processes and kinematical configurations are covered at LO. Thus, we expect smaller NLO corrections as the number of jets increases. In Section 3.4, this will be shown for $W\gamma\gamma j$ production. Second, NLO one-jet predictions allow us to address with sufficient precision theoretical uncertainties of the exclusive multi-boson cross sections. As a by-product, due to the nature of the selected processes, we can study their sensitivity to physics beyond the SM through AC.

Among the selected processes, we present the calculation of Higgs boson production in association with a W boson and a jet. This process is of particular interest to study the production of the Higgs boson, and its couplings to both the electroweak bosons on the production side and fermions on the decay side. The leptonic decay of the W boson can be used to tag events and allows to study Higgs decays to b quarks with less background than in other production channels [38, 39].

NLO EW corrections will become important when the experimental errors are reduced to the level of a few percent. This will soon be the case at the LHC run 2 for di-boson production [40]. The need to have NLO EW corrections for the tri-boson processes has also been indicated in Ref. [40]. We have recently provided first results for the full NLO EW corrections to on-shell VV (with $V = W^+, W^-, Z$) [41] and W^+W^-Z [42] production modes. The most important features and results will be reviewed in Section 3.5. NLO EW corrections to the di-boson channels have also recently been calculated in Refs. [43–45].

Finally, in Section 4, we will show a few examples of the effect of considering anomalous couplings for selected processes. In particular, we will present results at NLO QCD for the W^+Zj, $W^+\gamma j$, and VBF Hjj production processes. In the first two, a dynamical jet veto is introduced [31], which shows its potential to increase the sensitivity to anomalous couplings in these processes while keeping the size of the logarithms, which depend on the veto scale, under control.

2. Calculational setup

At hadron colliders the cross section for producing a final state X from the original hadrons, H_i, is given by

$$\sigma(H_1 H_2 \to X) = \sum_{a,b,\tilde{X}} \int_0^1 \mathrm{d}x_a\, \mathrm{d}x_b\, f_{a/H_1}(x_a, \mu_\mathrm{F}^2)\, f_{b/H_2}(x_b, \mu_\mathrm{F}^2)\, \sigma_{ab}(ab \to \tilde{X}; \mu_\mathrm{F}^2)\, \Theta(C(X))\, F(\tilde{X} \to X), \quad (1)$$

where the f_i are the parton distribution functions (PDFs) which can be interpreted at LO as the probability density of finding a parton a, b inside the hadron H_i ($i = 1, 2$), with a fraction of the hadron energy, $x_{a,b}$. $\Theta(C(X))$ stands for the cuts or selection criteria imposed for the final-state particles at the experimental or theoretical level and $F(\tilde{X} \to X)$ determines how the partons of the partonic state $\tilde{X}$ are recombined into observable jets of the state X in an infrared safe manner. The universal collinear singularities associated with the initial partons are factorized into the PDFs, introducing an unphysical factorization scale, μ_F. The scale, although arbitrary in principle, in fixed order perturbation theory has to be

chosen such that it is not very different from the typical scale that characterizes the hard process, otherwise large logarithms can show up spoiling the convergence of perturbation theory. $\sigma_{ab}(ab \to \tilde{X})$ is the partonic cross section which, for a contribution with n final state particles, $f_1 \dots f_n$, is given by

$$\sigma_{ab}(ab \to f_1 \dots f_n) = \frac{1}{4 p_a p_b} \int \mathrm{d}\Phi_n(p_a, p_b; p_{f_1}, \dots, p_{f_n}) \, |\langle a, b|T|f_1 \dots f_n\rangle|^2 \,, \quad (2)$$

where $\Phi_n(p_a, p_b; p_{f_1}, \dots, p_{f_n})$ represents the phase-space integration and the last term contains the interaction matrix element $\mathcal{M} = \langle a, b|T|f_1 \dots f_n\rangle$, typically computed perturbatively, in terms of Feynman diagrams. In perturbation theory, the cross section is written as an expansion in powers of the coupling constants of each interaction,

$$\sigma = \sum_{m,n} \alpha_s^m(\mu_R^2)\, \alpha^n(\mu_{R,EW}^2)\, \sigma_{m,n}(\mu_R^2, \mu_F^2). \quad (3)$$

EW interactions for almost all processes presented here involve massive gauge bosons or high-virtuality photons. Also, at tree-level not all electroweak parameters are independent of each other. Therefore, a useful choice for α, which we adopt here, is the so-called G_F scheme, where the masses of the W and Z boson as well as the Fermi constant G_F are an input value, and α is derived from those via the tree-level relation $\alpha_{G_F} = \sqrt{2} M_W^2 G_F (1 - M_W^2/M_Z^2)/\pi$. For QCD corrections we use the momentum subtraction scheme instead, which corresponds to the $\overline{\mathrm{MS}}$ scheme except that heavy quarks are decoupled. At each order in the perturbative expansion, this renormalization procedure introduces a dependence on the renormalization scale μ_R which disappears, however, when all orders are summed. As in the case of μ_F, the renormalization scale, although arbitrary in principle, has to be chosen such that it is not very different from the typical scale of the hard process.

The LO contribution to cross sections is given by the first term of the expansion in Eq. (3). The NLO corrections are obtained including an additional order for one coupling constant at a time. However, due to the strength of the QCD coupling, α_s, around 10 times higher than the electroweak coupling constant, for many processes at the LHC, the NLO QCD corrections are more important. In this section, we focus on the calculation of NLO QCD corrections. The calculation of NLO EW corrections follows similar steps and will be briefly mentioned in Section 3.5. At LO, the cross section is given by

$$\sigma^{LO} = \sum_{a,b} \int_0^1 \mathrm{d}x_a \, \mathrm{d}x_b \, f_a^{LO}(x_a, \mu_F^2)\, f_b^{LO}(x_b, \mu_F^2)\, \sigma_{ab}^B, \quad (4)$$

where σ^B is given by the LO partonic contribution to the interaction matrix elements, called "Born-amplitude" $\mathcal{M}_B$,

$$\sigma_{ab}^B = \frac{1}{4 p_a p_b} \sum_{\{f_n\}} \int \mathrm{d}\Phi_{2\to n} |\mathcal{M}_B|^2. \quad (5)$$

At NLO, we have

$$\sigma^{NLO} = \sum_{a,b} \int_0^1 \mathrm{d}x_a \, \mathrm{d}x_b \, f_a^{NLO}(x_a, \mu_F^2)\, f_b^{NLO}(x_b, \mu_F^2) \left[\sigma^B + \sigma^{\mathrm{NLO}}\right]_{ab}. \quad (6)$$

As a handy measure to quantify the size of the NLO corrections, we also define a K factor as the ratio of the NLO cross section over the LO one. For a differential distribution with observable x, it is given by

$$K = \frac{\mathrm{d}\sigma^{NLO}/\mathrm{d}x}{\mathrm{d}\sigma^{LO}/\mathrm{d}x}\,. \quad (7)$$

2.1. Cancelation of infrared divergences

In order to determine $\sigma_{ab}^{\mathrm{NLO}}$, we have to calculate two new contributions, the virtual corrections to the Born amplitude and the real emission contributions, which, individually, are infrared divergent. Additionally, due to the factorization of initial state singularities into a redefinition of the PDFs, an additional term, σ^C, is introduced. Thus, for a process with n particles in the final state, $\sigma_{ab}^{\mathrm{NLO}}$ is given by

$$\sigma_{ab}^{NLO} = \int_n \mathrm{d}\sigma^V + \int_{n+1} \mathrm{d}\sigma^R + \int_n \mathrm{d}\sigma^C, \quad (8)$$

where the subscripts n and $n+1$ denote the number of final state particles in the phase space integral. σ^V denotes the virtual contributions, which result from the interference of the Born with the virtual amplitude,

$$\sigma^V = \frac{1}{4 p_a p_b} \sum_{\{f_n\}} \int \mathrm{d}\Phi_{2\to n}\, 2\,\mathrm{Re}\left(\mathcal{M}_V \mathcal{M}_B^*\right). \quad (9)$$

σ^R denotes the corrections due to the emission of an extra real particle, which are determined by the modulus of the corresponding amplitude, $\mathcal{M}_{RE}$,

$$\sigma^R = \frac{1}{4 p_a p_b} \sum_{\{f_{n+1}\}} \int \mathrm{d}\Phi_{2\to n+1} |\mathcal{M}_{RE}|^2. \quad (10)$$

To compute the σ^i, we use the Feynman diagrammatic approach and the helicity formalism of Ref. [46, 47] to calculate the amplitude numerically. This requires that we first isolate any ultraviolet and infrared divergences via dimensional regularization/reduction as poles in $\varepsilon = (4 - D)/2$. While the poles of UV origin are removed by the renormalization of the parton fields and the strong coupling constant g_s, infrared singularities only cancel in the sum of all virtual, real emission and collinear contributions of Eq. (8). Since these contributions are separately divergent in four dimensions, they cannot be calculated using Monte Carlo techniques without further modifications. To cancel the divergences of the individual contributions, we use the dipole subtraction procedure by Catani and Seymour [4], where Eq. (8) is rewritten as

$$\sigma_{ab}^{NLO} = \int_{n+1} \left(\mathrm{d}\sigma^R\big|_{\varepsilon=0} - \mathrm{d}\sigma^A\big|_{\varepsilon=0} \right) + \int_n \left(\mathrm{d}\sigma^V + \mathrm{d}\sigma^C + \int_1 \mathrm{d}\sigma^A \right)_{\varepsilon=0}. \quad (11)$$

The subtraction term $\mathrm{d}\sigma^A$ is chosen such that it approaches the real emission contribution $\mathrm{d}\sigma^R$ in the soft and collinear limits,

$$\mathrm{d}\sigma^A \xrightarrow[\text{region}]{\text{soft/coll.}} \mathrm{d}\sigma^R, \quad (12)$$

which allows one to do the first integration of Eq. (11) numerically. Furthermore, it can be partially integrated analytically over the D-dimensional phase space of the additional parton emission. The Laurent series expansion of this integrated subtraction term then exactly cancels the divergences of the virtual and collinear contributions. These subtraction terms are particularly simple for Hjj production in VBF and will be discussed in more detail in the following. We note that this discussion taken from Ref. [1] can be used for all VBF and VBS processes with minor extensions.

Representative Feynman graphs for Hjj production are shown in Fig. 1. The final-state quarks lead to two well separated jets with high invariant mass, which allows us to neglect interferences of t- with u-channel or s-channel diagrams, which appear for identical quark flavors on the two fermion lines: the interference terms are strongly suppressed in the dominant phase-space regions. In this approximation, virtual corrections with a gluon exchange between both quark lines vanish due to the color structure. The NLO corrections to both quark lines can therefore be treated separately and we will only discuss the corrections to the upper quark line. The corrections to the lower one can then be obtained

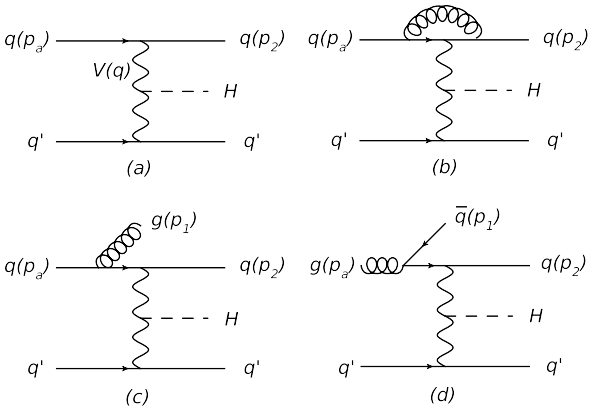

Figure 1: Representative contributions to Hjj production in VBF.

analogously. The virtual corrections only involve vertex corrections, Fig. 1(b), which factorize against the Born-level diagram,

$$2\,\mathrm{Re}(\mathcal{M}_V \mathcal{M}_B^*) = |\mathcal{M}_B|^2 \frac{\alpha_s}{2\pi} C_F \left(\frac{4\pi\mu_\mathrm{R}^2}{Q^2} \right)^\varepsilon \Gamma(1+\varepsilon) \left[-\frac{2}{\varepsilon^2} - \frac{3}{\varepsilon} + c_\mathrm{virt} \right], \quad (13)$$

with $C_F = 4/3$, $Q^2 = -q^2 = -(p_2 - p_a)^2$ and $c_\mathrm{virt} = \pi^2/3 - 7$ in dimensional reduction. The same factorization formula applies for the other VBF processes and multiboson production. However, there one obtains additional finite contributions, which are not proportional to the Born matrix element. Two classes of sub-processes appear in the real emission contribution, namely

$$q(p_a) + q' \to g(p_1) + q(p_2) + q' + H, \quad (14)$$
$$g(p_a) + q' \to \bar{q}(p_1) + q(p_2) + q' + H. \quad (15)$$

The additional parton can either be emitted from the initial state, see Fig. 1 (c)-(d), or from the final state quark. According to Ref. [4], the singular part of the quark-induced sub-process, Eq. (14), is given by the two dipoles $\mathcal{D}_{q_2}^{q_a g_1}$ and $\mathcal{D}_{q_2 g_1}^{q_a}$, which describe gluon emissions from the initial and final state, respectively. Their contribution can be written as

$$|\mathcal{M}^q|^2_\mathrm{sing} = \mathcal{D}_{q_2}^{q_a g_1} + \mathcal{D}_{q_2 g_1}^{q_a} = 8\pi\alpha_s C_F \frac{1}{Q^2} \frac{x^2 + z^2}{(1-x)(1-z)} |\mathcal{M}_B^q|^2, \quad (16)$$

where the momenta of the Born amplitude $\mathcal{M}_B^q$ of the LO process

$$q(\tilde{p}_a) + q' \to q(\tilde{p}_2) + q' + H, \quad (17)$$

are obtained from the real emission kinematics using

$$\tilde{p}_a = x p_a, \qquad \tilde{p}_2 = p_1 + p_2 - (1-x) p_a \tag{18}$$

and

$$x = 1 - \frac{p_1 \cdot p_2}{(p_1 + p_2) \cdot p_a}, \quad z = 1 - \frac{p_1 \cdot p_a}{(p_1 + p_2) \cdot p_a}. \tag{19}$$

The other momenta are unchanged. With this parametrization, the limits of collinear gluon emission from the initial or final state are given by $x \to 1$ and $z \to 1$, respectively, leading to singularities in Eq. (16). For soft gluon emission one obtains $x \to 1$ and $z \to 1$. Similarly, the singular part of the gluon-induced real emission sub-processes, Eq. (15), can be written as

$$|\mathcal{M}^g|^2_{\text{sing}} = \mathcal{D}^{g_a \bar{q}_1}_{q_2} + \mathcal{D}^{g_a q_2}_{\bar{q}_1} = 8\pi\alpha_s T_F \frac{1}{Q^2} \cdot \left[\frac{x^2 + (1-x)^2}{1-z} |\mathcal{M}^q_B|^2 + \frac{x^2 + (1-x)^2}{z} |\mathcal{M}^{\bar{q}}_B|^2 \right], \tag{20}$$

where $T_F = 1/2$, and $\mathcal{M}^{\bar{q}}_B$ corresponds to the LO process

$$\bar{q}(\tilde{p}_a) + q' \to \bar{q}(\tilde{p}_2) + q' + H \tag{21}$$

and $\mathcal{M}^q_B$ to the process in Eq. (17). Using the expressions of Eqs. (16) and (20) for the subtraction term $\mathrm{d}\sigma^A$ in Eq. (11), the integration over the phase space of the real emission can be done numerically. However, for the subtraction term, the jet definition function F (see Eq. (1)) must be applied using the Born kinematics defined in Eq. (18).

The analytic integration of the subtraction terms of Eqs. (16) and (20) over the phase space of the additional parton emission leads to the operator

$$\langle \mathbf{I} \rangle = |\mathcal{M}_B|^2 \frac{\alpha_s}{2\pi} C_F \left(\frac{4\pi\mu_R^2}{Q^2} \right)^{\varepsilon} \Gamma(1+\varepsilon) \left[\frac{2}{\varepsilon^2} + \frac{3}{\varepsilon} + 9 - \frac{4}{3}\pi^2 \right], \tag{22}$$

which cancels the singularities of Eq. (13), and additional contributions of collinear origin which can be combined with $\mathrm{d}\sigma^C$ into a redefinition of the PDFs. The convolution of the latter contributions with the PDFs results in the finite term

$$\sigma^C_{\text{fin}}(pp \to Hjj) = \sum_{a,b} \int_0^1 dx_a \int_0^1 dx_b \, f^c_a(x_a, \mu_F^2, \mu_R^2) \, f_b(x_b, \mu_F^2) \, \sigma^B_{ab}(ab \to Hjj), \tag{23}$$

with the modified PDF

$$f^c_q(x, \mu_F, \mu_R) = \frac{\alpha_s(\mu_R)}{2\pi} \int_x^1 \mathrm{d}z \left\{ f_g\left(\frac{x}{z}, \mu_F\right) A(z) + \left[f_q\left(\frac{x}{z}, \mu_F\right) - z f_q(x, \mu_F) \right] B(z) + f_q\left(\frac{x}{z}, \mu_F\right) C(z) \right\} + \frac{\alpha_s(\mu_R)}{2\pi} f_q(x, \mu_F) D(x). \tag{24}$$

The required integration kernels read

$$\begin{aligned}
A(z) &= T_F \left[z^2 + (1-z)^2 \right] \ln \frac{Q^2(1-z)}{\mu_F^2 z} + 2T_F \, z(1-z) \,, \\
B(z) &= C_F \left[\frac{2}{1-z} \ln \frac{Q^2(1-z)}{\mu_F^2} - \frac{3}{2} \frac{1}{1-z} \right] , \\
C(z) &= C_F \left[1 - z - \frac{2}{1-z} \ln z - (1+z) \ln \frac{Q^2(1-z)}{\mu_F^2 z} \right] , \\
D(x) &= C_F \left[\frac{3}{2} \ln \frac{Q^2}{\mu_F^2(1-x)} + 2 \ln(1-x) \ln \frac{Q^2}{\mu_F^2} + \ln^2(1-x) + \pi^2 - \frac{27}{2} - c_{\text{virt}} \right].
\end{aligned} \tag{25}$$

The term c_{virt} appearing here exactly cancels with its contribution in Eq. (13) and allows to shift finite terms between different parts of the calculation. The expressions above are given for PDFs defined in the prevalent $\overline{\text{MS}}$ scheme.

The structure found above can be taken over for all VBF and VBS processes discussed below, and also for the more complex processes the procedure is completely analogous. The main complication for VBF and VBS are additional finite contributions to the virtual amplitudes which do not factorize in terms of the Born amplitude. For more complex processes, like e.g. QCD $VVjj$ production, also many more subtraction terms arise, for which we refer to Ref. [4] and the original calculations for the various processes.

2.2. Electroweak decay currents

In the following, we present results for many processes such as Hjj, WHj, VVj, $VVjj$ and $VVV(j)$ ($V \in W, Z, \gamma$) production including leptonic decays of the massive gauge bosons. All off-shell and spin-correlation effects are fully taken into account. To describe the method for including these decay amplitudes, we will use as an example $VVjj$ production in VBF, which only includes diagrams involving t-channel exchanges of EW vector bosons.

Fig. 2 shows some representative Feynman diagrams. As shown in the figure, each diagram can be separated

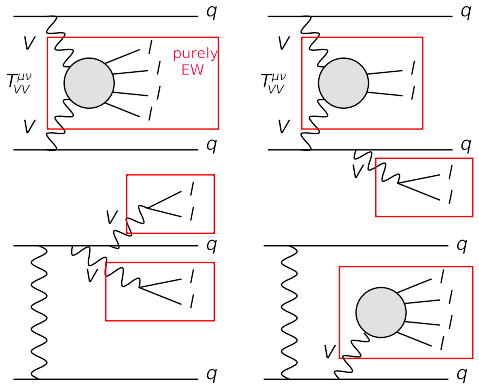

Figure 2: Representative Feynman diagrams for VBF production of a vector boson pair with two jets. The red boxes show purely EW contributions, which can be described by leptonic tensors.

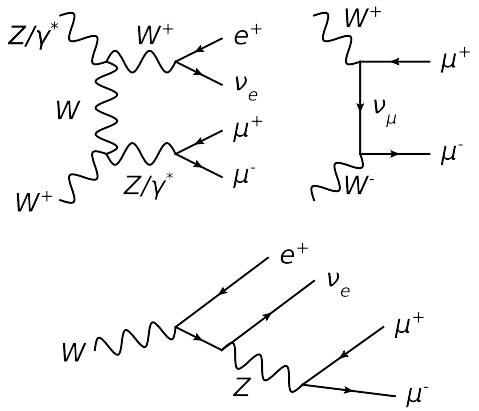

Figure 3: Representative contributions to the leptonic tensors appearing in VBF W^+Zjj production.

into purely EW parts, describing the decays of the vector bosons, and a part involving colored particles as well. This separation is common to all considered processes and can be exploited to obtain a modular structure for the implementation of the various processes. This is particularly useful for the inclusion of NLO QCD corrections, since these do not affect the purely EW parts. Since the virtual corrections can be grouped into building blocks, they can be used for various processes as discussed later. Furthermore, the implementation of modified gauge couplings to simulate physics beyond the SM only requires the modification of the purely EW parts (see Section 2.6).

First, we will focus on the EW parts of the diagrams, which can be further classified into different contributions as seen in Fig. 2: The processes with multiple vector bosons involve two- and multi-body decays of the vector bosons, which can be included in effective decay currents V^μ. VBF $VVjj$ production exhibits further contributions corresponding to $VV \to 2l$ and $VV \to 4l$ scattering, which can be described by leptonic tensors $T^{\mu\nu}_{VV}$. All off-shell contributions to these decay currents and tensors are included to obtain a valid description in all phase-space regions. Some representative diagrams, contributing to the EW structures in VBF W^+Zjj production are shown in Fig. 3. Since the effective decay vectors and tensors are the same for each partonic subprocess of a given process, it is convenient to calculate them only once for each phase-space point and use them for each sub-process. This improves the run-time of the numerical calculation significantly. Our implementation of the decay currents and tensors is based on HELAS routines [48] and uses the modified version of the complex-mass scheme [49] implemented in HELAS and MadGraph, where one substitutes $m_V^2 \to m_V^2 - im_V\Gamma_V$, while keeping a real value of the weak mixing angle. For example, the decay current of a vector boson V to a lepton anti-lepton pair ($l\bar{l}$) of fixed chirality reads

$$J^\mu = \frac{g_{Vlh}\,\bar{u}_l\gamma_\nu P_h v_{\bar{l}}}{q^2 - m_V^2 + im_V\Gamma_V}\left(-g^{\mu\nu} + \frac{q^\mu q^\nu}{m_V^2 - im_V\Gamma_V}\right), \quad (26)$$

where $P_h = (1 + h\gamma_5)/2$ is the projection operator and g_{Vlh} is the coupling constant of the corresponding Vll vertex. Except for the top quark, we neglect all fermion masses. This implies that in Eq. (26) the second term actually does not contribute at all. In our calculations we do not include final state interference terms due to identical leptons, since they are typically small. Technically, this means that we implement the processes for a fixed combination of final state leptons. Results for the other lepton combinations can then be obtained by applying appropriate combinatorial factors.

Another advantage of using leptonic tensors is the possibility to modify the EW structure without modifying the QCD calculations. Thus, the cross-checked implementation of a given process at NLO QCD in the SM can be reused to calculate amplitudes with a modified EW sector. Modifications in terms of anomalous couplings will be discussed below. Moreover, the technique has also been applied to obtain cross section calculations for models with extra spin-1 [50] and spin-2 [51, 52] resonances, which are included in the `VBFNLO` program.

2.3. Virtual corrections

After calculating the EW decay currents, the Born-level amplitudes can be generated using the helicity formalism of Refs. [46, 47]. A basic structure, which is repeated in many of the processes considered here, is n vector bosons being attached to a quark line. Considering the vector bosons as effective currents and stripping

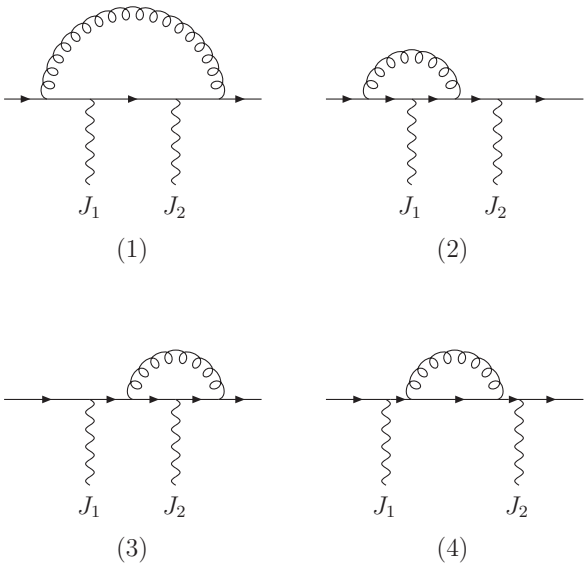

Figure 4: The "abelian BoxLine" combines the virtual QCD corrections to a quark line with two external vector bosons attached to it in a fixed order.

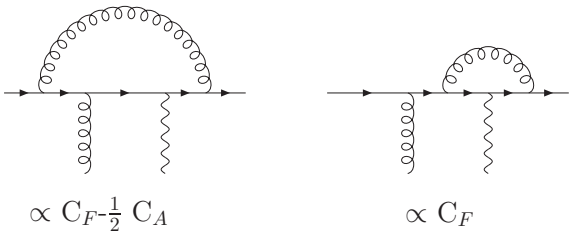

Figure 5: Color factors that appear when one gluon is emitted off the quark line.

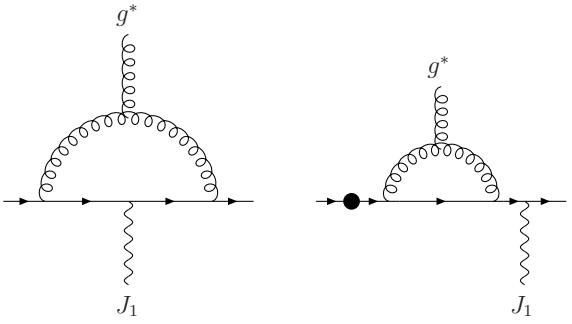

Figure 6: The "non-abelian BoxLine" comprises virtual corrections due to a quark line with two external bosons, which explicitly involve the non-abelian structure of QCD. The dot indicates a further position where the vector boson J_1 has to be attached.

off the coupling constants, these structures are universal. Since QCD corrections do not depend on the EW system, it is possible to implement process-independent

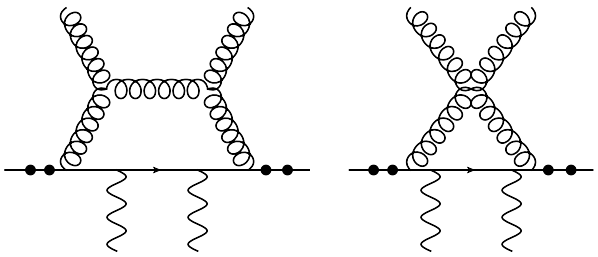

Figure 7: Additional non-abelian HexLine contributions appearing in QCD-induced $VVjj$ production. The dots indicate additional positions, where the external EW bosons have to be attached. One fixed permutation of the J_1 and J_2 currents is considered.

routines for calculating the virtual QCD corrections to these structures. For $n = 2$ these corrections, depicted in Fig. 4, are combined in one building block, which we call "abelian BoxLine" in the following. Similarly, the abelian PenLine and HexLine building blocks comprise the virtual corrections for $n = 3, 4$, respectively. The contribution of these building blocks can be decomposed as $\mathcal{M}_V = \widetilde{\mathcal{M}}_V + \mathcal{M}_V^{\mathrm{fac}}$, where $\mathcal{M}_V^{\mathrm{fac}}$ contains the IR divergent contributions and factorizes with respect to the corresponding Born diagram as given by Eq. (13). $\widetilde{\mathcal{M}}_V$ contains additional finite contributions and vanishes for vertex corrections ($n = 1$).

For processes where only EW bosons are attached to the quark line, i.e. VV and VVV production as well as the VBF and VBS processes, all virtual corrections can be calculated using these building blocks. The various topologies appearing in the VBS processes are depicted in Fig. 2. As mentioned earlier, we neglect interferences of t- and u-channel contributions. Thus, virtual corrections with a gluon exchange between the two quark lines vanish, allowing us to treat the virtual corrections to the upper and lower quark line separately. In the lower left diagram, three vector bosons are attached to the upper quark line. The corresponding virtual corrections, for a given permutation of the vector bosons, can be calculated using the PenLine routine. In addition, one has to calculate the vertex corrections to the lower line. Similarly, the virtual corrections to the lower quark line in the diagrams on the right are given by the BoxLine, while only vertex corrections are required for the upper quark line and the upper left diagram.

For processes with external gluons, the above building blocks provide a subset of the contributing diagrams, with one of the EW bosons being replaced by the gluon. This modification does not change the fundamental structure of the building block, but only alters the color factor associated with each diagram: While it is $(C_F - C_A/2)$ when the gluon is directly attached to the quark line in-

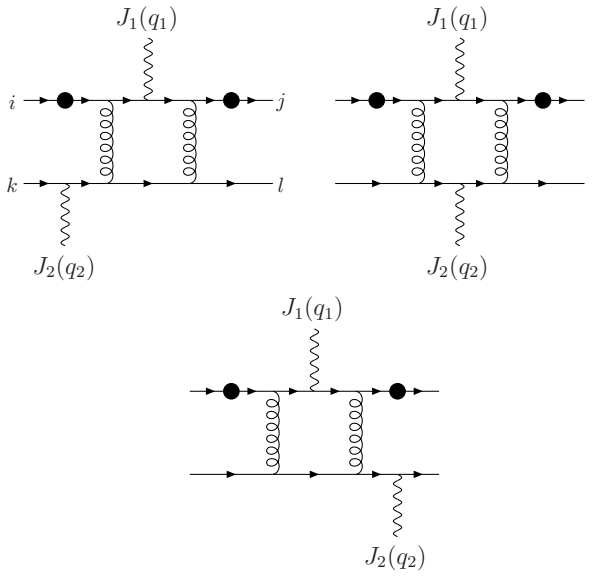

Figure 8: One group of "HexBox" contributions appearing in QCD-induced $VVjj$ production. The dots indicate additional positions, where the external boson on the upper line has to be attached. In addition, there is a similar group of six diagrams with both vector bosons being attached to the same quark line and the "PenBox" contributions, with a single vector current attached to one of the quark lines.

side the loop, it remains C_F for the other diagrams with the gluon not being attached to the loop (see Fig. 5). In QCD we have $C_A = 3$. In addition, due to the non-abelian nature of QCD, a new topology of virtual corrections appears, where the external gluon is attached to the gluon arc. This leads to a second set of building blocks, called "non-abelian BoxLine, PenLine and HexLine" (see Fig. 6).

With the above building blocks, the virtual amplitudes of many processes can be constructed. However, for some processes involving external gluons, there may also appear closed fermion loops. For this group, we apply Furry's theorem, wherever applicable, to reduce the number of contributions. Additional building blocks occurring in QCD-induced $VVjj$ production are further non-abelian PenLine and HexLine corrections (see Fig. 7) as well as contributions with two quark lines connected by double gluon exchange (Fig. 8).

For the implementation of the above building blocks a `Mathematica` package has been created using the methods presented in Ref. [53]: Algebraic manipulations of the Dirac structures are applied in D dimensions to contract repeated Lorentz indices and to identify all terms proportional to $\gamma^\mu\gamma_\mu = D$. Furthermore, scalar products of the loop momentum with a second momentum appearing in the numerator are canceled with the corresponding denominators of the loop propagators. The amplitude is then split into the contribution one obtains when setting $D = 4$ and a contribution proportional to $(D-4)$. This allows to obtain results in dimensional reduction and to identify the additional rational terms appearing in conventional dimensional regularization. Both parts are then decomposed into Standard Matrix elements, involving the spinor products of the quark line, which are multiplied with functions depending on the external momenta and polarization vectors. The latter functions are further decomposed into contributions involving scalar and tensor one-loop integrals and contributions dependent on the polarization vectors and/or the decay currents. This separation allows us to calculate the building blocks for various helicity configurations with minimal number of calls to time-consuming tensor integral routines. The reduction of the tensor integrals is done using the method of Passarino-Veltman [54] for up to box contributions and of Denner-Dittmaier [55] (see also Ref. [53]) for pentagons and hexagons.

The tensor reduction of the one-loop integrals can lead to numerical instabilities due to vanishing Gram- and Cayley-determinants. To obtain a numerically stable calculation of cross sections, these instabilities have to be identified and the corresponding contributions require further treatment. We tag instabilities in the building blocks using "gauge tests" based on Ward identities, which relate n-point functions of rank m to a difference of two $(n-1)$-point functions of rank $(m-1)$ by replacing an external current with its momentum:

$$p_i^\mu \mathcal{M}^n_\mu(\{p\}; p_{i-1}, p_i, p_{i+1}) = \mathcal{M}^{n-1}(\{p\}; p_{i-1}, p_i + p_{i+1}) - \mathcal{M}^{n-1}(\{p\}; p_{i-1} + p_i, p_{i+1}). \quad (27)$$

These Ward identities are inherited by the building blocks, so that, for example, a "Penline" can be expressed as the difference of two "boxlines". Checking Eq. (27) numerically serves as a strong and efficient test of the accuracy of the corresponding building blocks. By using a cache system for loop integrals, this test can be efficiently done without reevaluation of the loop integrals, since they had already been calculated before the above replacement. For many processes such instabilities only occur for a negligible fraction of the phase-space points. In this case we can just neglect these contributions by setting the amplitude to zero. However, for QCD-induced $VVjj$ production, the number of unstable points is not so small and hence a rescue system is needed. When the above test fails in double precision, the tensor reduction and scalar integrals of the unstable contributions are

reevaluated using quadruple precision and the gauge test is applied once more. The percentage of unstable points is then reduced to a negligible level.

2.4. Phase-space integration

The squared amplitudes have to be integrated over the phase space of the n final state particles and the two variables $x_{a,b}$ (see Eq. (1)), which leads to $3n-3$ non-trivial integrations. This multidimensional integration is most efficiently done using Monte Carlo techniques, which also allows the generation of arbitrary distributions without further runs of the program. In our implementation, we use a modified version of the VEGAS algorithm [56], which uses importance sampling to improve the convergence of the integration. A phase-space generator is needed to map the integration variables to the momenta of the particles. This mapping should take into account general features of the amplitudes such that more phase-space points are calculated in the regions with large contributions to the cross section. In particular the invariant mass of particles which can result from the decay of a massive particle should be mapped according to a Breit-Wigner distribution. This can be obtained using the factorization of the n-particle phase space

$$\mathrm{d}\Phi_n(P;p_1,\ldots,p_n) = (2\pi)^4\delta\left(P-\sum_j p_j\right)\left(\prod_i \frac{\mathrm{d}^3 p_i}{(2\pi)^3 2E_i}\right) \mathrm{d}\Phi_{i+1}(P;p_1,\ldots,p_i,q)\,\frac{\mathrm{d}q^2}{2\pi}\,\mathrm{d}\Phi_{n-i}(q;p_{i+1},\ldots,p_n), \tag{28}$$

where q^2 can be calculated as

$$q^2 = M\Gamma\tan x + M^2, \tag{29}$$

with a uniformly distributed variable x to obtain phase-space points which follow a Breit-Wigner distribution in q^2. The phase-space of the two-body decay $\mathrm{d}\Phi_2$ can be easily obtained in the center-of-mass system of the decaying particle. For the three-body decay one has the Dalitz representation

$$\mathrm{d}\Phi_3(P;p_1,p_2,p_3) = \frac{1}{(2\pi)^5}\frac{1}{32P^2} \mathrm{d}m_{12}^2\,\mathrm{d}m_{23}^2\,\mathrm{d}\alpha\,\mathrm{d}\cos\beta\,\mathrm{d}\gamma \tag{30}$$

with the three Euler angles α, β, γ and the particle pair invariant masses, m_{ij}. Special care has to be taken in the phase-space mapping of decay chains, in particular if Higgs resonances are involved. Due to the small value of Γ_H, Higgs resonances are not adequately accounted for in the Monte Carlo integration if they are not explicitly accounted for in the phase space mapping. In particular, for decay chains such as

$$H/Z/\gamma \to W^+W^- \to l^+\nu_l l^-\bar{\nu}_l, \tag{31}$$

the mapping for the invariant mass of the four leptons should take into account the resonances at M_H and M_Z. Furthermore, the invariant masses of the two W bosons have to be mapped appropriately, where one contribution might be far off-shell.

2.5. Final-state real photons

For processes with real photons in the final state some additional technicalities arise. First, a new set of scalar integrals not present in the off-shell photon case appears, as its invariant mass is exactly zero. Here we have cross-checked our implementation by comparing to a second independent calculation.

A second issue is photon radiation off the final-state charged leptons. While for the matrix elements this is straightforward and not different from the case with massive gauge bosons, it requires additional care to get an efficient phase space mapping for the Monte Carlo integration. Let us take $Z\gamma$ production as an example. The photon can be attached in two distinct parts: either at the initial-state quarks or at the final-state charged leptons. The second case corresponds to Drell-Yan production of the Z boson followed by a three-body decay into the $\ell^+\ell^-\gamma$ final state. Both options show a different kinematic behavior, and therefore we split the phase space accordingly. The invariant mass of the Z boson is always generated by a Breit-Wigner distribution with a low-energy flat part to account for the γ^* contribution. In the first case, the photon is implemented as parton radiation whose energy follows a $1/p_T$ law, and the Z simply decays into the two leptons. In the second case, we generate the leptons and the photon from a three-body decay of the Z. To avoid double-counting, the two phase space regions finally need to be separated, so that each configuration can be generated by exactly one of the two options. Therefore, after generating an event, we compare the invariant masses of the lepton pair and the three-particle system. Whichever is closer to the Z mass signifies from which phase-space generator this event should have come from. If this does not agree with the actual origin, the event is rejected.

When the Z boson is replaced by a W, a third distinct possibility arises: the photon can now also be radiated off the intermediate W boson. However, kinematically this configuration does not yield any new structures. Depending on whether the W after or before photon radiation is

closer to its mass shell, this can be assigned to the first or second option given above, respectively.

Finally, we need to ensure that the photons are hard and well separated from other particles to avoid IR divergences. Soft photon emission can easily be rejected by requiring a minimum transverse momentum of the photons. Radiation collinear to quarks however poses a problem. We need to ensure that events where photons and final-state quarks are collinear are rejected, while soft emission of final-state partons should be retained. In other words, we need to isolate the photons without spoiling infrared safety at the same time, which a naive R separation cut between photons and partons would do. Since we do not include any fragmentation contributions in processes with final-state photons, we choose to implement the procedure by Frixione given in Ref. [57]. If i denotes a parton with transverse energy $E_{T,i}$ and has a separation $R_{i\gamma}$ with a photon of transverse momentum $p_{T,\gamma}$, then the event is accepted only if

$$\sum_i E_{T,i}\Theta(\delta - R_{i\gamma}) \leq p_{T,\gamma}\frac{1-\cos\delta}{1-\cos\delta_0} \quad \forall\delta \leq \delta_0. \quad (32)$$

Hereby, δ_0 is a fixed separation which we set to 0.7. Eq. (32) allows final-state partons arbitrarily close to the photon axis as long as they are soft enough. Hence, the full QCD pole, which cancels against the virtual part, is retained, while at the same time QED IR divergences are avoided.

2.6. Anomalous couplings

Anomalous couplings allow to parametrize physics beyond the SM and are an excellent method to constrain and give limits on new physic effects which originate at some high energy scale, Λ. They can be described by an effective field theory Lagrangian,

$$\mathcal{L} = \mathcal{L}_{\rm SM} + \sum_{d>4}\sum_i \frac{f_i}{\Lambda^{d-4}}O_i^{(d)}, \quad (33)$$

where d is the energy dimension of the operator $O_i^{(d)}$ which describes the new physics effects. The leading order term is the SM Lagrangian. The free coupling strengths f_i of the individual operators allow to use a common new physics scale Λ. This means, however, that only the ratios f_i/Λ^{d-4} are meaningful quantities to be constrained experimentally. Different choices for a basis of operators exist. For the dimension-6 operators discussed in this review, we will use the basis presented and refined in Refs. [58–60]. A comprehensive list of the dimension-6 and dimension-8 operators as well as the relations between different parametrizations can be found in the Appendix of Ref. [61]. A few examples will suffice at this point.

Since we are concentrating on processes with electroweak bosons, only operators which can be constructed from the SM bosonic fields are considered in our calculations. More precisely, we use as building blocks the SM model Higgs doublet field, $\Phi = (0, (v+h)/\sqrt{2})^T$ in the unitary gauge, and the SU(2)×U(1) gauge fields in the form of either covariant derivatives, D_μ, or the field strength tensors

$$\begin{aligned}\widehat{W}_{\mu\nu} &= igT^a W^a_{\mu\nu}\\ \widehat{B}_{\mu\nu} &= ig'YB_{\mu\nu},\end{aligned} \quad (34)$$

where g and g' (T^a and Y) are the SU(2) and U(1) gauge couplings (generators), respectively, with the relation

$$[D_\mu, D_\nu] = \widehat{W}_{\mu\nu} + \widehat{B}_{\mu\nu}\,. \quad (35)$$

Examples of effective operators implemented in our calculations are

$$\begin{aligned}O_{WWW} &= \mathrm{Tr}\left[\widehat{W}_{\mu\nu}\widehat{W}^{\nu\rho}\widehat{W}_\rho{}^\mu\right]\\ O_W &= (D_\mu\Phi)^\dagger\widehat{W}^{\mu\nu}(D_\nu\Phi)\\ O_{WW} &= \Phi^\dagger\,\widehat{W}_{\mu\nu}\widehat{W}^{\mu\nu}\,\Phi\\ O_{\tilde{W}W} &= \Phi^\dagger\,\frac{1}{2}\varepsilon_{\alpha\beta\mu\nu}\widehat{W}^{\alpha\beta}\widehat{W}^{\mu\nu}\,\Phi\,.\end{aligned} \quad (36)$$

The first two induce anomalous $WW\gamma$ and WWZ triple gauge couplings, O_W also affects Higgs couplings to W, Z, and photon, while the last two only modify Higgs interactions with pairs of electroweak bosons (after a trivial, finite renormalization of the SM gauge fields and couplings).

Within our approach, these operators are incorporated via purpose-built HELAS effective currents. Thus, the SM electroweak decay currents of Section 2.2 are generalized to include anomalous couplings. For example, the SM decay current $\widetilde{W}^{SM} \to l^+\nu H$, would be replaced by $\widetilde{W} = \widetilde{W}^{SM} + \widetilde{W}^{AC}$, where $\widetilde{W}^{AC} \to l^+\nu H$ contains the contributions coming from dimension-6 operators. The QCD part of the calculation is not affected by these global changes. Thus, NLO QCD calculations for the SM can be directly transformed to AC computation.

AC effects through higher dimensional operators increase at large invariant masses. To preserve tree level unitarity, we use a dipole type form factor

$$F = \left(1 + \frac{s}{\Lambda^2_{\rm FF}}\right)^{-p}, \quad (37)$$

where $\sqrt{s}$ denotes the invariant mass of the produced electroweak boson system and with $p \geq d-4$ for a

dimension-d operator. The value for the form factor scale $\Lambda_{\rm FF}$ is derived from requiring that unitarity is preserved in $VV \to VV$ scattering, which can be evaluated with the form factor tool available on the VBFNLO website [62]. In Section 4, AC effects will be studied for selected processes.

3. Phenomenological aspects

To numerically evaluate cross sections, in the electroweak sector, we choose the W, Z and Higgs mass as well as the Fermi constant as input. The remaining electroweak parameters, the electromagnetic coupling and the weak mixing angle, are then derived via tree-level relations, i.e. we use:

$$\begin{aligned} m_W &= 80.398\,\text{GeV}, \quad & G_F &= 1.166\,37 \times 10^{-5}\,\text{GeV}^{-2}, \\ m_Z &= 91.1876\,\text{GeV}, \quad & \alpha^{-1} &\equiv \alpha_{G_F}^{-1} = 132.3407, \\ m_H &= 125.0\,\text{GeV}, \quad & \sin^2(\theta_W) &= 0.22264. \end{aligned} \tag{38}$$

The widths of the bosons are taken as

$$\begin{aligned} \Gamma_W &= 2.098\,\text{GeV}, \quad & \Gamma_Z &= 2.508\,\text{GeV}, \\ \Gamma_H &= 4.134\,\text{MeV}. \end{aligned} \tag{39}$$

As default we consider the LHC at 14 TeV. To mimic the generic capabilities of the experimental detectors, we impose a set of minimal cuts on the transverse momenta and rapidities of the final-state charged leptons and photons. Additionally, these objects as well as jets must be well separated from each other in the rapidity-azimuthal angle plane. Specifically, if not stated otherwise, we choose as cuts

$$\begin{aligned} p_{T,\ell(\gamma)} &> 20\,\text{GeV}, \quad & |y_{\ell(\gamma)}| &< 2.5, \\ R_{j\ell} &> 0.4, \quad & R_{\ell\gamma} &> 0.4, \\ R_{j\gamma} &> 0.7, \quad & R_{\gamma\gamma} &> 0.4, \\ M_{\ell^+\ell^-} &> 15\,\text{GeV}. \end{aligned} \tag{40}$$

We define jets as final-state partons clustered using the k_T algorithm [63, 64] with an R separation of 0.8 and require that they have a transverse momentum $p_{T,j} > 30\,\text{GeV}$ and rapidity $|y_j| < 4.5$. The last cut in Eq. (40) eliminates the singularity arising from a virtual photon, $\gamma^* \to \ell^+\ell^-$, by requiring that the invariant mass of a pair of oppositely charged leptons is larger than 15 GeV. The separation parameter of the Frixione cut, Eq. (32), is set to $\delta_0 = 0.7$. The parton distribution functions used are given in each process section.

3.1. Vector-boson fusion

Vector-boson fusion and vector-boson scattering processes (collectively dubbed VBF in this section) were the first ones to be considered, in the case of VBF Hjj [1] and Vjj [65] production even before the start of the SFB project. In subsequent years we have added NLO QCD corrections for almost all vector-boson scattering processes, i.e. for $VVjj$ final states originating from t-channel electroweak boson exchange between two quarks or anti quarks [5–8, 10]. For W^+W^+jj production, independent results were obtained in Ref. [9].

In all our calculations, leptonic decays of the final state W or (Z, γ^*) are included, as well as all off-shell effects, via the method of leptonic tensors described in Section 2.2. For the VBF production of a single "gauge boson", the basic processes are [65]

$$pp \to \ell^+\ell^- jj + X \qquad (\text{"VBF-}Z\text{"}), \tag{41}$$
$$pp \to \ell^\pm \nu jj + X \qquad (\text{"VBF-}W^\pm\text{"}), \tag{42}$$
$$pp \to \gamma jj + X \qquad (\text{"VBF-}\gamma\text{"}), \tag{43}$$

from which e.g. Zjj production with decay $Z \to \bar{\nu}\nu$ is obtained by a simple replacement of the leptonic tensors in the calculation of the process in Eq. (41). For Higgs production, a multitude of experimentally distinct decay modes exists, many of which are implemented in VBFNLO. For simplicity, and because the Higgs boson is a very narrow, scalar resonance without spin correlations between production and decay, we do not consider individual decay modes of the Higgs boson in the following, but rather treat it as a final state particle when discussing the production processes [1, 66–74]

$$pp \to Hjj + X \qquad (\text{"VBF-}H\text{"}), \tag{44}$$
$$pp \to Hjjj + X \qquad (\text{"VBF-}H\text{+ jet"}), \tag{45}$$
$$pp \to HHjj + X \qquad (\text{"VBF-}HH\text{"}), \tag{46}$$
$$pp \to H\gamma jj + X \qquad (\text{"VBF-}H\gamma\text{"}). \tag{47}$$

For vector-boson scattering, the basic production cross sections calculated at NLO QCD are [5–8, 10]

$$pp \to \ell_1^+ \nu_{\ell_1} \ell_2^- \bar{\nu}_{\ell_2} jj + X \qquad (\text{"VBF-}W^+W^-\text{"}), \tag{48}$$
$$pp \to \ell_1^+ \ell_1^- \ell_2^+ \ell_2^- jj + X \qquad (\text{"VBF-}ZZ\text{"}), \tag{49}$$
$$pp \to \ell_1^\pm \nu_{\ell_1} \ell_2^+ \ell_2^- jj + X \qquad (\text{"VBF-}W^\pm Z\text{"}), \tag{50}$$
$$pp \to \ell_1^\pm \nu_{\ell_1} \ell_2^\pm \nu_{\ell_2} jj + X \qquad (\text{"VBF-}W^\pm W^\pm\text{"}), \tag{51}$$
$$pp \to \ell^\pm \nu \gamma jj + X \qquad (\text{"VBF-}W^\pm\gamma\text{"}). \tag{52}$$

For the VBF-WZ and VBF-ZZ processes, $Z \to \bar{\nu}\nu$ decay is again obtained by a simple modification of the leptonic tensors and also discussed below. In addition, for VBF production of two massive electroweak bosons,

LHC	$\sqrt{s}$ = 8 TeV			$\sqrt{s}$ = 14 TeV		
Process	$\sigma_{\rm LO}$	$\sigma_{\rm NLO}$	K	$\sigma_{\rm LO}$	$\sigma_{\rm NLO}$	K
$pp \to Hjj$ ("VBF-H")	318.33(4) fb	328.73(15) fb	1.03	1033.67(11) fb	1079.5(5) fb	1.04
$pp \to Hjjj$ ("VBF-H+jet")	27.602(8) fb	27.05(7) fb	0.98	120.05(3) fb	118.7(4) fb	0.99
$pp \to HHjj$ ("VBF-HH")	0.14788(3) fb	0.14622(8) fb	0.99	0.71222(15) fb	0.7057(4) fb	0.99
$pp \to H\gamma jj$ ("VBF-$H\gamma$")	4.7603(7) fb	4.837(3) fb	1.02	17.141(2) fb	17.531(14) fb	1.02
$pp \to \ell^+\ell^- jj$ ("VBF-Z_ℓ")	77.54(4) fb	84.27(11) fb	1.09	258.33(14) fb	285.7(4) fb	1.11
$pp \to \nu\bar{\nu} jj$ ("VBF-Z_ν")	192.57(10) fb	212.0(3) fb	1.10	701.5(4) fb	785.3(10) fb	1.12
$pp \to \ell^+\nu jj$ ("VBF-W^+")	764.14(14) fb	816.9(5) fb	1.07	2279.2(4) fb	2486.0(17) fb	1.09
$pp \to \ell^-\bar{\nu} jj$ ("VBF-W^-")	409.06(7) fb	446.9(3) fb	1.09	1377.9(3) fb	1528.0(9) fb	1.11
$pp \to \gamma jj$ ("VBF-γ")	1824.5(5) fb	2033(2) fb	1.11	5221.3(15) fb	5918(7) fb	1.13
$pp \to \ell_1^+\nu_{\ell_1}\ell_2^-\bar{\nu}_{\ell_2} jj$ ("VBF-W^+W^-")	6.023(3) fb	6.268(10) fb	1.04	23.327(14) fb	24.52(6) fb	1.05
$pp \to \ell_1^+\ell_1^-\ell_2^+\ell_2^- jj$ ("VBF-$Z_\ell Z_\ell$")	49.95(4) ab	52.56(14) ab	1.05	233.24(17) ab	247.3(7) ab	1.06
$pp \to \ell_1^+\ell_1^-\nu_2\bar{\nu}_2 jj$ ("VBF-$Z_\ell Z_\nu$")	0.3693(2) fb	0.3892(7) fb	1.05	1.6151(10) fb	1.712(2) fb	1.06
$pp \to \ell_1^+\nu_{\ell_1}\ell_2^+\ell_2^- jj$ ("VBF-W^+Z_ℓ")	0.40346(15) fb	0.4172(4) fb	1.03	1.7220(6) fb	1.800(17) fb	1.05
$pp \to \ell_1^-\bar{\nu}_{\ell_1}\ell_2^+\ell_2^- jj$ ("VBF-W^-Z_ℓ")	0.19374(7) fb	0.2048(2) fb	1.06	0.9376(4) fb	0.9976(8) fb	1.06
$pp \to \ell_1^+\nu_{\ell_1}\ell_2^+\nu_{\ell_2} jj$ ("VBF-W^+W^+")	1.4085(4) fb	1.4454(14) fb	1.03	5.8299(18) fb	6.064(4) fb	1.04
$pp \to \ell_1^-\bar{\nu}_{\ell_1}\ell_2^-\bar{\nu}_{\ell_2} jj$ ("VBF-W^-W^-")	0.33950(10) fb	0.3705(3) fb	1.09	1.8047(5) fb	1.9666(14) fb	1.09
$pp \to \ell^+\nu\gamma jj$ ("VBF-$W^+\gamma$")	9.412(3) fb	9.885(18) fb	1.05	32.285(10) fb	34.28(5) fb	1.06
$pp \to \ell^-\bar{\nu}\gamma jj$ ("VBF-$W^-\gamma$")	4.8293(13) fb	5.155(5) fb	1.07	18.673(5) fb	20.17(2) fb	1.08
$pp \to q\bar{q}\ell^-\bar{\nu}_\ell jj$ ("VBF-$W^+_{\rm had}W^-$")	4.453(4) fb	5.059(16) fb	1.14	18.437(18) fb	21.88(6) fb	1.19
$pp \to \ell^+\nu_\ell q\bar{q} jj$ ("VBF-$W^+W^-_{\rm had}$")	4.239(4) fb	4.83(2) fb	1.14	17.486(16) fb	20.71(5) fb	1.18
$pp \to \ell^+\ell^- q\bar{q} jj$ ("VBF-$Z_\ell Z_{\rm had}$")	0.3759(4) fb	0.428(2) fb	1.14	1.826(2) fb	2.119(6) fb	1.16
$pp \to q\bar{q}\ell^+\ell^- jj$ ("VBF-$W^+_{\rm had}Z_\ell$")	0.3773(2) fb	0.4271(8) fb	1.13	1.6187(10) fb	1.912(4) fb	1.18
$pp \to \ell^+\nu_\ell q\bar{q} jj$ ("VBF-$W^+Z_{\rm had}$")	1.7041(10) fb	1.880(4) fb	1.10	7.530(4) fb	8.610(17) fb	1.14
$pp \to q\bar{q}\ell^+\ell^- jj$ ("VBF-$W^-_{\rm had}Z_\ell$")	0.17127(9) fb	0.1961(4) fb	1.14	0.8450(5) fb	1.0023(16) fb	1.19
$pp \to \ell^-\bar{\nu}_\ell q\bar{q} jj$ ("VBF-$W^-Z_{\rm had}$")	0.8004(5) fb	0.915(2) fb	1.14	3.996(2) fb	4.681(9) fb	1.17
$pp \to q\bar{q}\ell^+\nu_\ell jj$ ("VBF-$W^+_{\rm had}W^+$")	2.6714(11) fb	2.929(4) fb	1.10	11.055(5) fb	12.667(17) fb	1.15
$pp \to q\bar{q}\ell^-\bar{\nu}_\ell jj$ ("VBF-$W^-_{\rm had}W^-$")	0.6117(3) fb	0.7155(13) fb	1.17	3.3008(15) fb	3.953(4) fb	1.20

Table 1: Integrated cross sections for VBF production processes for the LHC running at a center-of-mass energy of 8 and 14 TeV. Results are given summed over all three lepton generations and, in case of quarks, all combinations which do not involve a top quark. The error in brackets is the statistical error from Monte Carlo integration.

semileptonic decays are very interesting experimentally, because of the increased branching ratios of e.g. $\bar{q}q'\ell\ell$ final states as compared to fully leptonic decays of both weak bosons. The increased rate becomes particularly attractive at large invariant masses of the scattered weak boson pair. For this reason, hadronic decays of one of the weak bosons have also been implemented, without full NLO corrections to the decays, however [30]. This means that at the amplitude level, the leptonic tensors have been modified to reflect the couplings of quarks to the Z or photon, and additional care has been taken to correctly match the jet clustering algorithm to the presence of two additional final state partons, i.e. to avoid spurious collinear singularities in the calculation. For details we refer the reader to Ref. [30].

A tell-tale signature for VBF processes are the tagging jets produced by the two scattered (anti)quarks (see Fig. 2). They, typically, are widely separated in rapidity and their invariant mass is much larger than for the QCD backgrounds. In order to suppress the latter, additional cuts on the tagging jets have to be imposed at the LHC. We therefore consider cross sections with the additional cuts

$$|y_{j_1} - y_{j_2}| > 4.0, \quad y_{j_1} \cdot y_{j_2} < 0, \quad M_{j_1 j_2} > 600\,\text{GeV} \tag{53}$$

on the two tagging jets which, for the purely leptonic

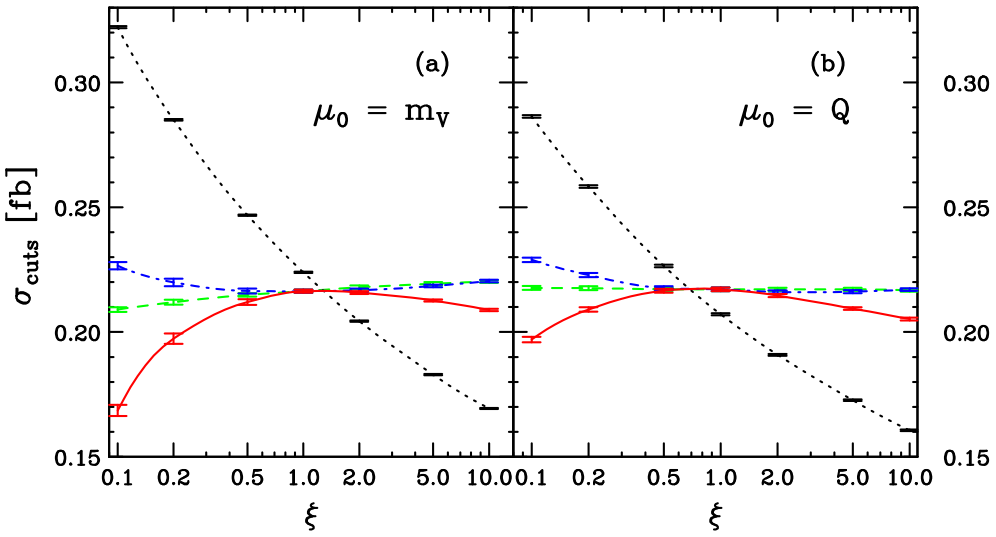

Figure 9: Scale dependence of the total $pp \to e^+\nu_e\,\mu^+\mu^-\,jj$ cross section for two different reference scales, $\mu_0 = m_W$ and $\mu_0 = Q_i$. The NLO curves show $\sigma^{\rm NLO}_{\rm cuts}$ as a function of the scale parameter ξ for three different cases: $\mu_R = \mu_F = \xi\mu_0$ (solid red), $\mu_F = \xi\mu_0$ and $\mu_R = \mu_0$ (dot-dashed blue), $\mu_R = \xi\mu_0$ and $\mu_F = \mu_0$ (dashed green). The LO cross sections depend only on μ_F (dotted black). From Ref. [8].

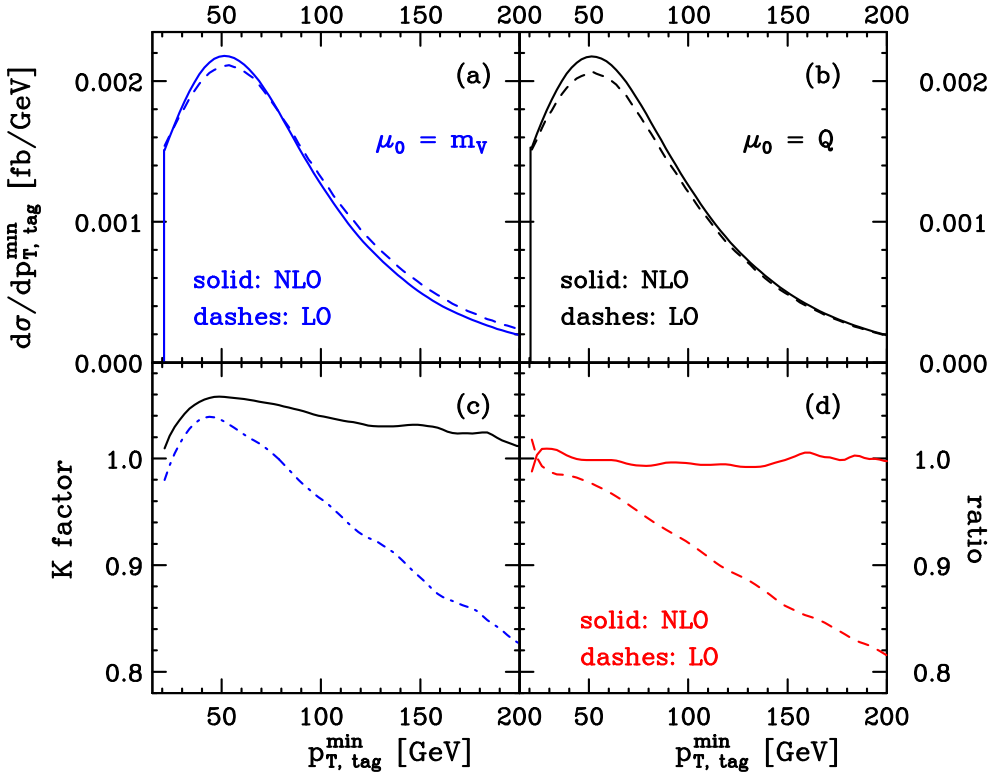

Figure 10: Transverse-momentum distribution of the softer tagging jet in VBF $e^+\nu_e\,\mu^+\mu^-\,jj$ production at the LHC for two different scale choices [panels (a) and (b)]. Panel (c) shows the K factors for $\mu_0 = m_V$ (dot-dashed blue line) and $\mu_0 = Q_i$ (solid black line). In panel (d) the ratio $[d\sigma/dp^{\rm min}_{T,\rm tag}(\mu_0 = m_V)/[d\sigma/dp^{\rm min}_{T,\rm tag}(\mu_0 = Q)]$ is plotted at LO (dashed red line) and NLO (solid red line). From Ref. [8]

decay modes (and for Higgs boson production), are defined as the two highest transverse momentum jets of the event. For the semileptonic decay modes in VBS, we first determine the jet pair whose invariant mass is closest to the mass of the hadronically decaying vector boson. The tagging jets are then chosen from the remaining jets as those with the highest transverse momentum.

In Table 1, we provide LO and NLO cross sections within this restricted phase space region, for pp collisions at $\sqrt{s} = 8$ and 14 TeV. As PDFs we choose the CTEQ6L1 [75] set at LO and the CT10 set [76] with $\alpha_s(m_Z) = 0.1180$ at NLO. Up to NLO QCD, an excellent scale choice for VBF processes is the virtuality Q_1^2 or Q_2^2 of the t-channel weak bosons in Feynman graphs such as the ones shown in Fig. 1. Since the QCD corrections to the upper and the lower quark lines can be separated up to NLO, two different scales can be used in the calculation, which we symbolically write as

$$\mu_{\rm F}^2 = \mu_{\rm R}^2 = Q_i^2 \,. \tag{54}$$

This scale choice has been used in Table 1. It is particularly helpful at LO and results in quite small QCD corrections in all VBF processes, as is apparent from the K factors between 0.98 and 1.2 in the table.

The scale variations of the integrated cross sections exhibit a very similar behavior for all VBF processes. As a typical example, the W^+Zjj case is depicted in Fig. 9. The variation of the LO and NLO $pp \to e^+\nu_e\,\mu^+\mu^-\,jj+X$ cross sections is shown as a function of the factorization and renormalization scales separately, and also for $\mu_{\rm F} = \mu_{\rm R} = \xi\mu_0$, where the reference scale is either held fixed ($\mu_0 = (m_W + m_Z)/2 = m_V$) or is chosen as $\mu_0 = Q_i$. The LO cross sections show an appreciable dependence on the factorization scale, while at NLO the variation is reduced to a very low level: varying scales by a factor of $\xi = 2^{\pm 1}$, one observes a cross section dependence of about $\pm 11\%$ at LO which is reduced to below 2% at NLO for all cases shown in the figure.

The scale dependence of infrared and collinear safe distributions is substantially reduced at NLO as well. As an example, the p_T-distribution of the softer tagging jet is shown in Fig. 10 for $e^+\nu_e\,\mu^+\mu^-\,jj$ events at the LHC 14, i.e. for VBF W^+Zjj production, for $\mu_0 = m_V$ and $\mu_0 = Q_i$. The relation of LO to NLO curves depends on the scale choice, as is clear from the K factor distribution shown in panel (c). However, this dependence is almost entirely due to the scale dependence of the LO curves. The ratio of the NLO curves, shown in panel (d), is indistinguishable from unity within the Monte Carlo error, while this ratio varies between 1 and 0.8 at LO. One finds very stable NLO predictions, which nicely demonstrate the value of the NLO QCD corrections.

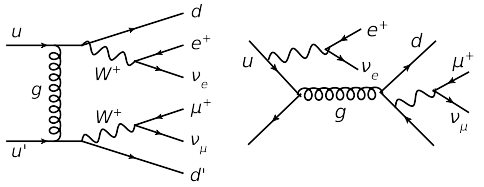

Figure 11: Representative tree-level 4-quark Feynman diagrams of the QCD-induced mechanisms for the process $pp \to e^+\nu_e\mu^+\nu_\mu jj + X$ ("QCD-W^+W^+jj"). Similar diagrams exist also for the processes (56-60).

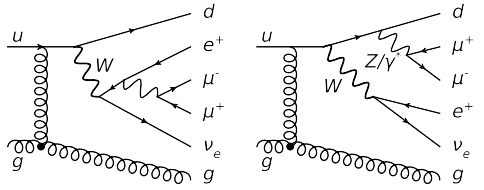

Figure 12: Representative tree-level 2-quark 2-gluon Feynman diagrams of the QCD-induced mechanisms for the process $pp \to e^+\nu_e\mu^+\mu^-\,jj + X$ ("QCD-W^+W^+jj"). Similar diagrams exist also for the processes (57-60).

3.2. QCD-induced $VVjj$ production

In this section, we discuss the QCD-induced mechanisms to produce either four leptons or two leptons and one photon in association with two jets at the LHC. Specifically, full NLO QCD calculations have been performed for the following processes with four-lepton final states,

$$pp \to jj\,\ell_1^+\nu_{\ell_1}\,\ell_2^+\nu_{\ell_2} + X \quad (\text{"QCD-}W^+W^+jj\text{"}), \tag{55}$$
$$pp \to jj\,\ell_1^+\nu_{\ell_1}\,\ell_2^+\ell_2^- + X \quad (\text{"QCD-}W^+Z_\ell jj\text{"}), \tag{56}$$
$$pp \to jj\,\ell_1^+\ell_1^-\,\ell_2^+\ell_2^- + X \quad (\text{"QCD-}Z_\ell Z_\ell jj\text{"}), \tag{57}$$

and for the final states containing two leptons and a photon,

$$pp \to jj\,\ell^+\nu_\ell\,\gamma + X \quad (\text{"QCD-}W^+\gamma jj\text{"}), \tag{58}$$
$$pp \to jj\,\ell^+\ell^-\,\gamma + X \quad (\text{"QCD-}Z_\ell\gamma jj\text{"}), \tag{59}$$
$$pp \to jj\,\nu_\ell\bar{\nu}_\ell\,\gamma + X \quad (\text{"QCD-}Z_\nu\gamma jj\text{"}). \tag{60}$$

The corresponding processes obtained from charge conjugation of the final state have also been calculated and are available in the `VBFNLO` program. Since their results are similar to the original ones, we will focus on the above specified processes only. Those processes are called $VVjj$ production, because the leptons come from intermediate EW gauge bosons. We will sometimes refer to them in short as "W^+W^+jj", "W^+Zjj", "$ZZjj$", "$W^+\gamma jj$" and "$Z\gamma jj$" for simplicity.

At LO, all Feynman diagrams are classified into two groups: one with two quark lines and the other

LHC	$\sqrt{s}$ = 8 TeV			$\sqrt{s}$ = 14 TeV		
Process	$\sigma_{\rm LO}$	$\sigma_{\rm NLO}$	K	$\sigma_{\rm LO}$	$\sigma_{\rm NLO}$	K
$pp \to \ell^+\ell^- jj$ ("QCD-$Z_\ell jj$")	123.0(1) pb	128.8(1) pb	1.05	293.4(1) pb	288.9(3) pb	0.98
$pp \to \nu_\ell\bar{\nu}_\ell jj$ ("QCD-$Z_\nu jj$")	314.3(1) pb	317.5(3) pb	1.01	862.9(1) pb	813.8(7) pb	0.94
$pp \to \ell^+\nu_\ell jj$ ("QCD-W^+jj")	549.3(1) pb	579.2(7) pb	1.05	1221(1) pb	1214(2) pb	0.99
$pp \to \ell^-\bar{\nu}_\ell jj$ ("QCD-W^-jj")	345.8(1) pb	367.4(5) pb	1.06	875.0(2) pb	882.2(12) pb	1.00
$pp \to \ell_1^+\ell_1^-\ell_2^+\ell_2^- jj$ ("QCD-$Z_\ell Z_\ell jj$")	3.738(2) fb	4.153(10) fb	1.11	10.36(1) fb	10.83(4) fb	1.05
$pp \to \ell_1^+\ell_1^-\nu_{\ell_2}\bar{\nu}_{\ell_2} jj$ ("QCD-$Z_\ell Z_\nu jj$")	20.25(1) fb	22.35(5) fb	1.10	60.60(2) fb	63.31(18) fb	1.04
$pp \to \ell_1^+\nu_{\ell_1}\ell_2^+\ell_2^- jj$ ("QCD-$W^+Z_\ell jj$")	33.17(2) fb	33.46(11) fb	1.01	91.34(1) fb	83.39(7) fb	0.91
$pp \to \ell_1^-\bar{\nu}_{\ell_1}\ell_2^+\ell_2^- jj$ ("QCD-$W^-Z_\ell jj$")	18.15(1) fb	18.19(7) fb	1.00	58.64(3) fb	53.52(20) fb	0.91
$pp \to \ell_1^+\nu_{\ell_1}\ell_2^+\nu_{\ell_2} jj$ ("QCD-W^+W^+jj")	3.149(2) fb	4.124(8) fb	1.31	7.023(2) fb	9.049(8) fb	1.29
$pp \to \ell_1^-\bar{\nu}_{\ell_1}\ell_2^-\bar{\nu}_{\ell_2} jj$ ("QCD-W^-W^-jj")	1.299(1) fb	1.767(2) fb	1.36	3.559(2) fb	4.714(5) fb	1.32
$pp \to \ell^+\ell^-\gamma jj$ ("QCD-$Z_l\gamma jj$")	283.2(2) fb	309.7(14) fb	1.10	698.2(6) fb	729.6(33) fb	1.04
$pp \to \nu_\ell\bar{\nu}_\ell\gamma jj$ ("QCD-$Z_\nu\gamma jj$")	350.2(1) fb	399.9(7) fb	1.14	940.8(2) fb	1023.6(22) fb	1.09
$pp \to \ell^+\nu_\ell\gamma jj$ ("QCD-$W^+\gamma jj$")	733.6(3) fb	801.5(25) fb	1.09	1868.1(3) fb	1815.0(9) fb	0.97
$pp \to \ell^-\bar{\nu}_\ell\gamma jj$ ("QCD-$W^-\gamma jj$")	477.8(2) fb	548.7(17) fb	1.15	1372.8(1) fb	1378.8(36) fb	1.00

Table 2: Integrated cross sections for QCD-induced Vjj and $VVjj$ production processes for the LHC running at a center-of-mass energy of 8 and 14 TeV. Results are given summed over all three lepton generations using the scale $\mu'_{\rm HT}$ defined in Eq. (63). The error in brackets is the statistical error from Monte Carlo integration. LHC predictions for Vjj production have been presented first in Ref. [77].

with one quark line. In other words, in terms of sub-processes, there are four-quark and two-quark two-gluon sub-processes, respectively. Representative Feynman diagrams are shown in Figs. 11 and 12. The same-sign lepton signature in process (55) is the simplest because only four-quark sub-processes exist at LO. The other processes have both contributions. Therefore, from both theoretical and experimental viewpoints, the same-sign lepton channel is easiest because of its small background. In fact, the first $VVjj$ analyses performed by ATLAS [78] and CMS [79] consider this final state already at 8 TeV.

Another important feature is that the total cross section of process (55) is well defined without any kinematic cut. This is because, as can be seen from Fig. 11, at LO each quark line radiates a W boson, whose mass acts as an infrared cutoff. This is not the case for the other sub-processes, where a minimum transverse momentum has to be imposed on every final state parton. This suggests that additional jet activity may have different impact on the same-sign lepton process than on the other ones. To quantify this, we will study the NLO QCD corrections to the m_{jj} and $\Delta y_{\rm tags}$ distributions of the two leading jets, which are defined as the two with the largest transverse momentum. Before that, we have to specify the cuts and address the issue of scale choice.

The input parameters are defined in Eqs. (38) and (39) and we use the MSTW2008 [80] parton distribution functions. Furthermore, we slightly modified the cuts of Eq. (40), requiring that

$$p_{T,j} > 20\ {\rm GeV}, \quad p_{T,\gamma} > 30\ {\rm GeV}, \tag{61}$$

where the anti-k_t algorithm [81] with a cone radius of $R = 0.4$ is used to cluster partons into jets. Instead of the cut on m_{ll}, we require $R_{ll} > 0.4$. For the cut on $R_{(l,\gamma)j}$, all reconstructed jets are taken into account. In addition, a cut on the missing transverse momentum associated with the neutrinos is applied, $\not{p}_T > 30$ GeV, when there is a neutrino in the final state. For processes with a final-state photon we use the photon isolation criterion à la Frixione [57] with a cone radius of $\delta_0 = 0.7$ as described in Subsection 2.5. Thereby, the use of photon fragmentation functions can be avoided.

We set the renormalization and factorization scales equal and study the following three choices:

$$\mu_{\rm HT} = \left(\sum_{\rm partons} p_{T,i} + \sum_{i=1}^{2} E_{T,V_i}\right)/2, \tag{62}$$

$$\mu'_{\rm HT} = \left(\sum_{\rm jet} p_{T,i} e^{|y_i - y_{12}|} + \sum_{i=1}^{2} E_{T,V_i}\right)/2, \tag{63}$$

$$\mu_{\rm ET} = \left[E_{T,jj} + E_{T,VV}\right]/2, \tag{64}$$

where $E_{T,V_i} = \sqrt{p_{T,V_i}^2 + m_{V_i}^2}$ with m_{V_i} being the invariant

mass of the corresponding leptons in case of W and Z bosons. Equivalent definitions are used for $E_{T,VV}$ and $E_{T,jj}$ of the system of the two hardest jets, and $y_{12} = (y_1 + y_2)/2$ is the average rapidity of the two hardest jets. We remark that the scale $\mu'_{\rm HT}$ approaches $\mu_{\rm HT}$ when the jets are produced close to each other. However, $\mu'_{\rm HT}$ becomes much larger when the jets are well separated. Indeed, the scale $\mu_{\rm HT}$ is too small when there are two well separated jets produced, because the invariant mass of these two jets is much larger than their transverse momenta as can be seen from the following relation

$$m_{ij}^2 \approx 2 p_{T,i} p_{T,j} \Big[\cosh(\Delta y_{ij}) - \cos(\Delta \phi_{ij}) \Big] . \qquad (65)$$

The third choice $\mu_{\rm ET}$ is similar to $\mu'_{\rm HT}$. The $E_{T,jj}$ term interpolates between the transverse momentum and the invariant mass of the tagging-jet system when $\Delta y_{\rm tags}$ is small or large, respectively. We have checked that $\mu'_{\rm HT}$ and $\mu_{\rm ET}$ indeed produce nearly identical results for various kinematic distributions at both LO and NLO.

In Table 2 we present integrated cross sections at LO and NLO for the LHC at a center-of-mass energy of 8 and 14 TeV. As central scale we use $\mu'_{\rm HT}$ defined in Eq. (63). K factors for all processes are fairly modest, with same-sign $WWjj$ production as the only exception. Here new channels with one gluon in the initial state appear for the real emission process, which give additional contributions not present at LO and therefore probably increase the K factor.

Let us now turn to studying scale variation and differential distributions. All plots in the following are for the LHC running at 14 TeV. In Fig. 13, we show the scale dependence of the integrated cross section for the above three scale choices and for two representative processes, the same-sign W^+W^+jj and the W^+Zjj production processes. Results for the other processes, (57-60), are very similar to the latter, hence will not be presented. By varying the renormalization and factorization scales independently, we find that the dependence on $\mu_{\rm R}$ is much stronger than on $\mu_{\rm F}$. We observe an obvious difference in shape between W^+W^+jj and W^+Zjj. This is due to the difference mentioned above, namely the two-quark two-gluon sub-processes occur in the latter, but not in the former. The differences between the three scale choices are also visible: the scales $\mu'_{\rm HT}$ and $\mu_{\rm ET}$ give similar cross sections already at LO and the result with $\mu_{\rm HT}$ is in general larger. This is clear from the definition of the scales as discussed above. The nearly identical LO cross section for W^+W^+jj production for $\mu'_{\rm HT}$ and $\mu_{\rm ET}$ is due to very similar differential distributions $\frac{{\rm d}\sigma}{{\rm d}\mu'_{\rm HT}}$ and $\frac{{\rm d}\sigma}{{\rm d}\mu_{\rm ET}}$ for this process. This symmetry is broken at NLO, leading to a more pronounced difference. The NLO results show

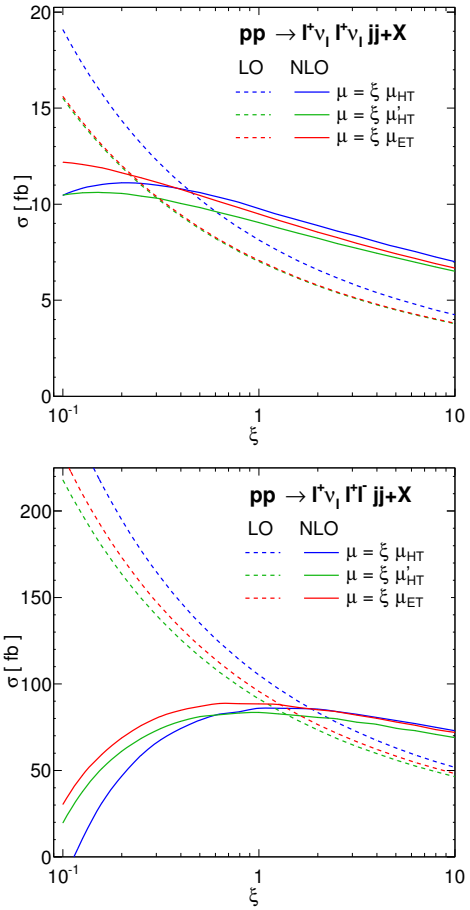

Figure 13: Scale dependence of the integrated cross section at LO and NLO for $pp \to \ell_1^+ \nu_{\ell_1} \ell_2^+ \nu_{\ell_2} jj + X$ ("QCD-W^+W^+jj") (top) and for $pp \to \ell_1^+ \nu_{\ell_1} \ell_2^+ \ell_2^- jj + X$ ("QCD-$W^+Z_\ell jj$") (bottom) around the central scale and for the three scale choices defined in Eqs. (62)-(64). All possible combinations of leptons of the three generations are included.

that there is a large range of ξ where the cross section is quite stable and nearly the same for all three scale choices. The W^+W^+jj cross section looks less stable, probably because there are new sub-processes with an initial-state gluon occurring at NLO. This result shows the importance of NLO calculations and that a sensible scale choice must be used.

We now discuss the NLO QCD corrections to the invariant mass m_{jj} and rapidity separation $\Delta y_{\rm tags}$ distributions of the two leading jets. We plot, again for W^+W^+jj and W^+Zjj production, the m_{jj} distributions in Fig. 14 and for $\Delta y_{\rm tags}$ in Fig. 15. In all these plots, we see as common feature that the uncertainty band due to scale variations is significantly reduced when NLO corrections are included. For the m_{jj} distributions, the QCD corrections are regular for both processes, with K factors

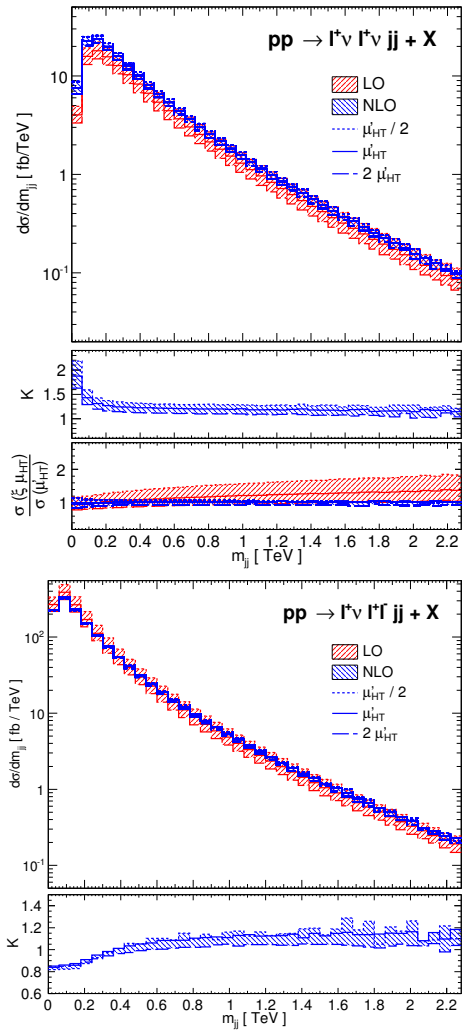

Figure 14: Differential cross sections for $pp \to \ell_1^+\nu_{\ell_1}\ell_2^+\nu_{\ell_2}jj + X$ ("QCD-W^+W^+jj") (top) and for $pp \to \ell_1^+\nu_{\ell_1}\ell_2^+\ell_2^-jj + X$ ("QCD-$W^+Z_\ell jj$") (bottom) production showing the invariant mass distribution of the tagging jets. The bands in the two big panels describe scale variations by a factor of two around the central scale. The K factor bands are due to the scale variation of the NLO results, with respect to $\sigma_{LO}(\mu'_{\rm HT})$. For the top plot, the upper and middle panels are produced using the scale $\mu'_{\rm HT}$, and in the lower panel we show the ratio of the differential cross sections using the scale $\xi\mu_{\rm HT}$ over $\mu'_{\rm HT}$ at LO and NLO with $\xi \in [1/2, 2]$.

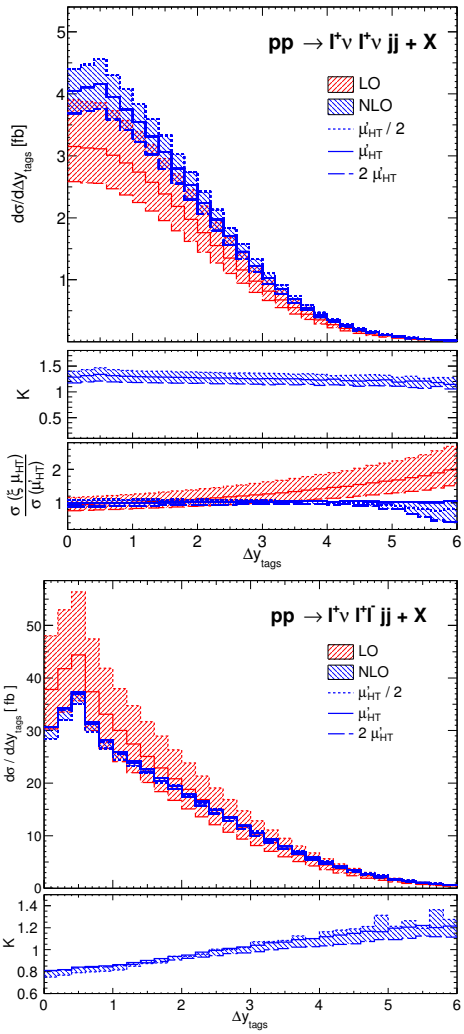

Figure 15: Similar to Fig. 14 but for the rapidity separation $\Delta y_{\rm tags}$.

constant at large energies up to 2.2 TeV. However, there is a striking difference at low energies in the K factors between the two processes. For W^+W^+jj production, the K factor is larger than 2 for $m_{jj} < 30\,\text{GeV}$. This can be understood as follows. At LO, there are two quark jets, which are well separated, because there is a finite IR cutoff due to the W mass. The m_{jj} distribution has a peak at about 150 GeV at LO. The position of the peak is shifted to a smaller value at NLO, leading to a large K factor at small m_{jj}. This is due to a new kinematic configuration opening up at NLO, where a final-state quark splits into a quark-gluon pair, resulting in two jets with low invariant mass. The second quark can either be unobserved or be combined in the quark jet. We have explicitly verified this by computing that contribution separately. For W^+Zjj production, there is no new kinematic configuration opening up at NLO, therefore the K factor is more regular.

Concerning the $\Delta y_{\rm tags}$ distributions for the scale choice $\mu'_{\rm HT}$, we observe an obvious difference in the K factors of the two processes. For same-sign W^+W^+jj production, the K factor is rather constant, while it is increasing for W^+Zjj production. Indeed, for all the other processes similar to the latter, we find that the K factors always increase with $\Delta y_{\rm tags}$ for the two scale choices $\mu'_{\rm HT}$ and

$\mu_{\rm ET}$. These are considered to be the best choices, since they take into account both the transverse momenta of the jets and the invariant mass of the tagging-jet system. For W^+W^+jj production, we also display the ratio of $\sigma(\xi\mu_{\rm HT})$ over $\sigma(\mu'_{\rm HT})$ at LO and NLO in Fig. 15 (top). At LO, the two scale choices produce very different results. However, the results are much closer at NLO and they show much narrower scale variation bands, reflecting the substantially improved reliability of the NLO predictions.

We now discuss processes with a photon in the final state. For photon isolation, the Frixione cut as specified above is used. We choose a representative process, namely $Z\gamma jj$ production with the Z boson decaying into charged leptons. The NLO QCD corrections are similar to the W^+Zjj case. We therefore focus here on the issue of how to separate $Z\gamma$ production from radiative Z decays where the photon is radiated off a charged decay lepton. Fortunately, this background can be reduced using a cut on the invariant mass of the $l^+l^-\gamma$ system, named $m_{Z\gamma}$ for short. The optimum value of the cut is a priori uncertain. We therefore use the $\bar{\nu}\nu\gamma jj$ channel, where the background is absent, to determine it.

In the left panel of Fig. 16, we plot the integrated NLO cross sections as functions of the $m_{Z\gamma}$ cut for the $l^+l^-\gamma jj$ and $\bar{\nu}\nu\gamma jj$ channels, the latter being multiplied by the ratio of the charged-lepton versus neutrino branching ratios of the Z, $\mathrm{BR}(Z \to l^+l^-)/\mathrm{BR}(Z \to \bar{\nu}\nu) = 0.506$. The LO cross section is also shown for the charged-lepton channel. In the bottom panel, the ratios of the modified neutrino cross sections to the LO and NLO charged-lepton cross sections are plotted. They do not converge to one in the tails due to the different cuts imposed on charged leptons versus neutrinos, see Ref. [21] for details. As expected, for the charged-lepton case, one observes that the cross section sharply decreases when the cut value is greater than the Z mass. In the middle panel, the K factors are plotted. We observe that $m^{\rm cut}_{Z\gamma} = 120\,\mathrm{GeV}$ is a good value, since the K factor exhibits a plateau and the slope of the cross section curves are approximately equal for both processes beyond this value (see bottom panel). This is confirmed in the right panel of Fig. 16, where the normalized differential distributions of the reconstructed rapidity-azimuthal angle separation of the $Z\gamma$ system are plotted for the two channels. One observes that the cut $m_{Z\gamma} > m_Z + \Gamma_Z$ reduces considerably the effect of the radiative decay in the charged-lepton channel, but some remnant is still clearly visible by comparing to the neutrino channel. Increasing the cut value to 120 GeV makes the NLO distribution of the $l^+l^-\gamma jj$ channel very similar to the corresponding $\bar{\nu}\nu\gamma jj$ one. This is better seen in the bottom panel, where the ratios of the normalized differential distributions between the two channels are plotted. The ratio of the $m^{\rm cut}_{Z\gamma} = 120\,\mathrm{GeV}$ curve versus the $\bar{\nu}\nu\gamma jj$ distribution is rather flat and close to one, until $R_{Z\gamma}$ reaches values of around 3 and then decreases. This difference is probably again due to the different cuts applied to the charged leptons and the neutrinos.

3.3. Tri-boson production

NLO QCD corrections have been calculated for all possible combinations of three electroweak gauge bosons [24–29, 82–84]. Leptonic decays of the gauge bosons as well as all spin correlations and off-shell contributions are included in the results shown in the following. For simplicity we will refer to all processes by their on-shell name, e.g., "$W^+W^-Z_\ell$" stands for $\ell^+_1\nu_{\ell_1}\ell^-_2\bar{\nu}_{\ell_2}\ell^+_3\ell^-_3$ production. Additionally, we will also show results where one of the gauge bosons decays hadronically [30]. Also effects due to intermediate Higgs boson exchange are correctly taken into account. An example set of Feynman diagrams for the "W^+ZZ" production process is depicted in Fig. 17. NLO EW corrections are available only for the "W^+W^-Z" and "$W^+W^-\gamma$" production processes and only with on-shell final-state gauge bosons or in the narrow-width approximation [42, 85].

For the numerical results in this sub-section, we use the input parameters and cuts defined in Eqs. (38), (39) and (40). Any effects arising from top quarks are neglected throughout. Bottom-quark contributions are only taken into account for those processes where their inclusion does not lead to diagrams with intermediate top quarks, i.e. all processes which contain neutral gauge bosons only. The bottom and all other light quarks are assumed to be massless, and we use the approximation where the CKM matrix is the identity matrix. As parton distribution functions we choose the CTEQ6L1 [75] set at LO and the CT10 set [76] with $\alpha_s(m_Z) = 0.1180$ at NLO. As central scale, we take the invariant mass of all final-state leptons and photons as factorization and renormalization scale. For the semileptonic decay modes, the quarks originating from the decays of the massive gauge bosons are included as well:

$$\mu_{\rm F} = \mu_{\rm R} = \mu_0 = \sqrt{\left(\sum_\ell p_\ell + \sum_\nu p_\nu + \sum_\gamma p_\gamma + \sum_{q_{\rm decay}} p_{q_{\rm decay}}\right)^2}\,. \quad (66)$$

For the tree-level process, this corresponds to the partonic center-of-mass energy of the process.

In Table 3, we present results for the integrated cross sections of the various tri-boson production processes

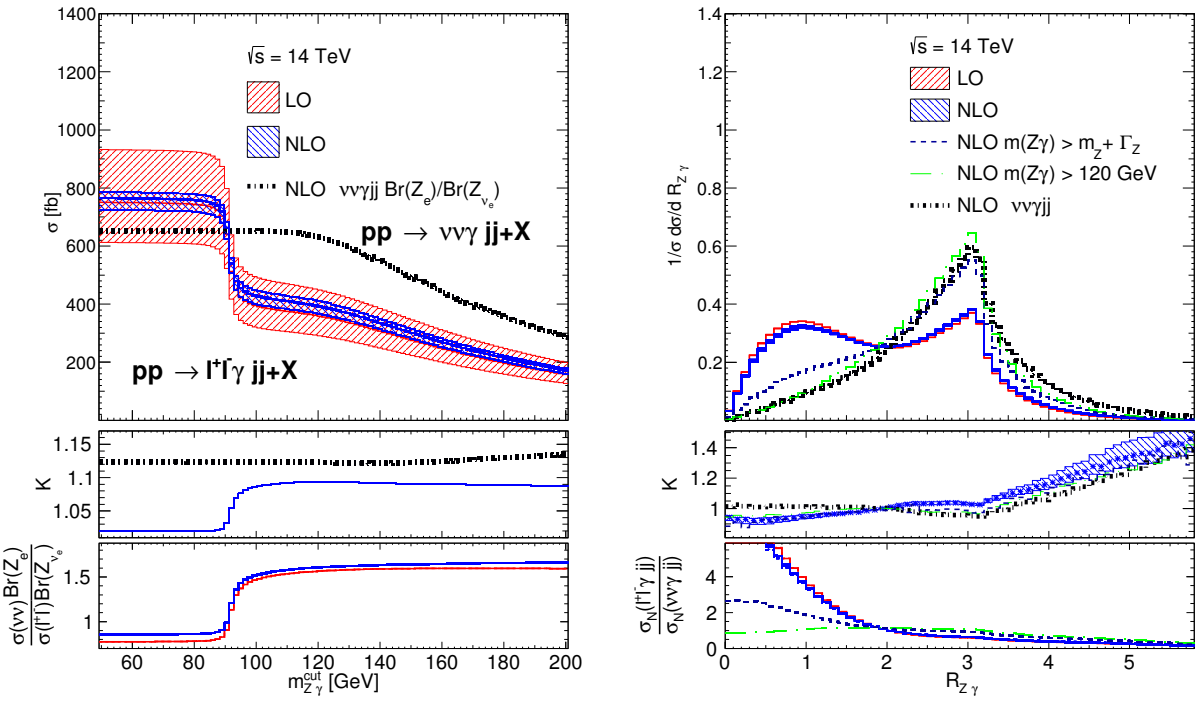

Figure 16: Left: Integrated cross section for different values of the reconstructed $Z\gamma$ invariant mass cut. The neutrino curve is multiplied by the ratio of the charged-lepton versus neutrino branching ratios. The middle panel shows the K factor and the lower one the ratios of the modified neutrino cross section versus the LO and NLO electron cross sections. Right: Normalized differential distributions of the rapidity-azimuthal angle separation $R_{Z\gamma}$ for different values of $m_{Z\gamma}^{\text{cut}}$. The middle and lower panels show the differential K factor plots and the ratios of the normalized charged-lepton versus neutrino pair production channels. The scale choice is $\mu_F = \mu_R = \mu_{ET}$, as defined in Eq. (64).

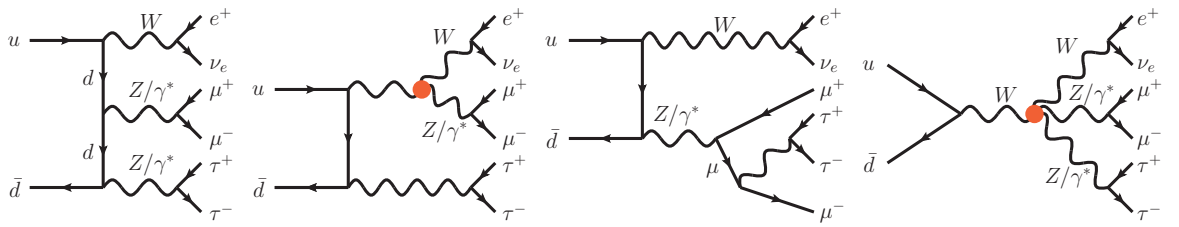

Figure 17: Example set of tree-level Feynman diagrams for the "W^+ZZ" production process. The triple and quartic gauge coupling vertices are marked with a red dot.

for the LHC at a center-of-mass energy of 8 and 14 TeV. Results are given summed over all three lepton generations. In doing so, we set all lepton masses to zero and ignore interference effects from identical leptons in the final state, since interference contributions are small.

We see that the processes cover a wide range of different cross sections. All production channels are dominated by approximately on-shell production of the vector bosons, which is of order $O\left(\alpha^3\right)$. Off-shell effects lead to corrections, but do not lead to large changes in the inclusive cross sections. For the massive vector bosons we then must add the relevant branching ratios. These are approximately 30% for the leptonic decay channels of the W boson. For the Z boson the numbers are 10% for decays in all pairs of charged leptons and 20% into neutrinos. The branching ratio into quarks in contrast is roughly 70% for both cases, explaining the typically larger cross sections for the semi-leptonic decay modes compared to the fully leptonic ones.

NLO QCD corrections are fairly large for this process class, with K factors ranging from 1.4 to 2.2 for the fully leptonic decay modes. This is due to new partonic sub-processes as well as new topologies opening up at NLO. This important feature will be discussed in detail

LHC	$\sqrt{s}$ = 8 TeV			$\sqrt{s}$ = 14 TeV		
Process	$\sigma_{\rm LO}$	$\sigma_{\rm NLO}$	K	$\sigma_{\rm LO}$	$\sigma_{\rm NLO}$	K
$pp \to \ell_1^+\nu_{\ell_1}\ell_2^-\bar{\nu}_{\ell_2}\ell_3^+\ell_3^-$ ("$W^+W^-Z_\ell$")	0.28514(16) fb	0.4400(3) fb	1.54	0.6287(4) fb	1.0597(13) fb	1.69
$pp \to \ell_1^+\nu_{\ell_1}\ell_2^+\ell_2^-\ell_3^+\ell_3^-$ ("$W^+Z_\ell Z_\ell$")	10.342(7) ab	17.578(19) ab	1.70	21.567(15) ab	42.20(5) ab	1.96
$pp \to \ell_1^-\bar{\nu}_{\ell_1}\ell_2^+\ell_2^-\ell_3^+\ell_3^-$ ("$W^-Z_\ell Z_\ell$")	4.775(3) ab	8.804(9) ab	1.84	11.957(8) ab	25.14(3) ab	2.10
$pp \to \ell_1^+\nu_{\ell_1}\ell_2^-\bar{\nu}_{\ell_2}\ell_3^+\nu_{\ell_3}$ ("$W^+W^-W^+$")	1.1724(14) fb	1.713(4) fb	1.46	2.263(3) fb	3.514(8) fb	1.55
$pp \to \ell_1^-\bar{\nu}_{\ell_1}\ell_2^+\nu\ell_2\ell_3^-\bar{\nu}_{\ell_3}$ ("$W^-W^+W^-$")	0.5957(7) fb	0.901(2) fb	1.51	1.3500(15) fb	2.171(5) fb	1.61
$pp \to \ell_1^+\ell_1^-\ell_2^+\ell_2^-\ell_3^+\ell_3^-$ ("$Z_\ell Z_\ell Z_\ell$")	1.675(2) ab	2.358(11) ab	1.41	3.720(6) ab	5.29(2) ab	1.42
$pp \to \ell_1^+\nu_{\ell_1}\ell_2^-\bar{\nu}_{\ell_2}\gamma$ ("$W^+W^-\gamma$")	7.7706(17) fb	12.706(5) fb	1.64	15.262(4) fb	26.856(12) fb	1.76
$pp \to \ell_1^+\ell_1^-\ell_2^+\ell_2^-\gamma$ ("$Z_\ell Z_\ell\gamma$")	0.19214(6) fb	0.2726(2) fb	1.42	0.36998(12) fb	0.5288(4) fb	1.43
$pp \to \ell_1^+\ell_1^-\nu_{\ell_2}\bar{\nu}_{\ell_2}\gamma$ ("$Z_\ell Z_\nu\gamma$")	0.7450(2) fb	1.0585(5) fb	1.42	1.5182(4) fb	2.1679(12) fb	1.43
$pp \to \ell_1^+\nu_{\ell_1}\ell_2^+\ell_2^-\gamma$ ("$W^+Z_\ell\gamma$")	0.7354(2) fb	1.3347(6) fb	1.81	1.3315(4) fb	2.7334(13) fb	2.05
$pp \to \ell_1^-\bar{\nu}_{\ell_1}\ell_2^+\ell_2^-\gamma$ ("$W^-Z_\ell\gamma$")	0.40445(11) fb	0.7929(3) fb	1.96	0.8653(2) fb	1.8950(8) fb	2.19
$pp \to \ell^+\nu_\ell\gamma\gamma$ ("$W^+\gamma\gamma$")	4.4161(12) fb	11.654(5) fb	2.64	7.586(2) fb	23.806(9) fb	3.14
$pp \to \ell^-\bar{\nu}_\ell\gamma\gamma$ ("$W^-\gamma\gamma$")	2.9949(7) fb	9.105(3) fb	3.04	5.8381(14) fb	20.260(7) fb	3.47
$pp \to \ell^+\ell^-\gamma\gamma$ ("$Z_\ell\gamma\gamma$")	5.4817(11) fb	8.236(5) fb	1.50	9.636(2) fb	14.655(9) fb	1.52
$pp \to \nu_\ell\bar{\nu}_\ell\gamma\gamma$ ("$Z_\nu\gamma\gamma$")	4.6966(8) fb	7.163(4) fb	1.53	8.7147(16) fb	13.533(6) fb	1.55
$pp \to \gamma\gamma\gamma$ ("$\gamma\gamma\gamma$")	12.959(4) fb	31.680(17) fb	2.44	22.175(7) fb	58.58(3) fb	2.64
$pp \to q\bar{q}\ell_1^-\bar{\nu}_{\ell_1}\ell_2^+\ell_2^-$ ("$W^+_{\rm had}W^-Z_\ell$")	0.20306(18) fb	0.5400(6) fb	2.66	0.4655(4) fb	1.527(2) fb	3.28
$pp \to \ell_1^+\nu_{\ell_1}q\bar{q}\ell_3^+\ell_3^-$ ("$W^+W^-_{\rm had}Z_\ell$")	0.20221(16) fb	0.5256(5) fb	2.60	0.4609(4) fb	1.4619(16) fb	3.17
$pp \to \ell_1^+\nu_{\ell_1}\ell_2^-\bar{\nu}_{\ell_2}q\bar{q}$ ("$W^+W^-Z_{\rm had}$")	1.3936(10) fb	2.789(3) fb	2.00	3.175(3) fb	7.448(8) fb	2.35
$pp \to q\bar{q}\ell_2^+\ell_2^-\ell_3^+\ell_3^-$ ("$W^+_{\rm had}Z_\ell Z_\ell$")	11.060(10) ab	27.16(4) ab	2.46	24.31(2) ab	74.21(8) ab	3.05
$pp \to \ell_1^+\nu_{\ell_1}q\bar{q}\ell_2^+\ell_2^-$ ("$W^+Z_{\rm had}Z_\ell$")	0.08786(9) fb	0.2168(3) fb	2.47	0.1895(2) fb	0.5891(8) fb	3.11
$pp \to q\bar{q}\ell_1^+\ell_1^-\ell_2^+\ell_2^-$ ("$W^-_{\rm had}Z_\ell Z_\ell$")	4.974(4) ab	13.040(14) ab	2.62	12.869(11) ab	41.49(4) ab	3.22
$pp \to \ell_1^-\bar{\nu}_{\ell_1}q\bar{q}\ell_2^+\ell_2^-$ ("$W^-Z_{\rm had}Z_\ell$")	0.04070(4) fb	0.11087(14) fb	2.72	0.10598(12) fb	0.3538(7) fb	3.34
$pp \to q\bar{q}\ell_1^-\bar{\nu}_{\ell_1}\ell_2^+\nu_{\ell_2}$ ("$W^+_{\rm had}W^-W^+$")	2.075(4) fb	4.448(10) fb	2.14	4.206(8) fb	10.56(2) fb	2.51
$pp \to \ell_1^+\nu_{\ell_1}q\bar{q}\ell_2^+\nu_{\ell_2}$ ("$W^+W^-_{\rm had}W^+$")	0.8280(15) fb	1.947(4) fb	2.35	1.657(3) fb	4.568(10) fb	2.76
$pp \to \ell_1^-\bar{\nu}_{\ell_1}q\bar{q}\ell_2^-\bar{\nu}_{\ell_2}$ ("$W^-W^+_{\rm had}W^-$")	0.3941(7) fb	1.007(2) fb	2.56	0.9229(16) fb	2.762(6) fb	2.99
$pp \to q\bar{q}\ell_1^+\nu\ell_1\ell_2^-\bar{\nu}_{\ell_2}$ ("$W^-_{\rm had}W^+W^-$")	1.0661(17) fb	2.324(6) fb	2.18	2.537(4) fb	6.359(15) fb	2.51
$pp \to q\bar{q}\ell_1^+\ell_1^-\ell_2^+\ell_2^-$ ("$Z_{\rm had}Z_\ell Z_\ell$")	21.10(4) ab	38.90(12) ab	1.84	48.85(17) ab	97.2(6) ab	1.99
$pp \to q\bar{q}\ell^-\bar{\nu}_\ell\gamma$ ("$W^+_{\rm had}W^-\gamma$")	5.804(2) fb	15.243(8) fb	2.63	11.987(4) fb	37.054(16) fb	3.09
$pp \to \ell^+\nu_\ell q\bar{q}\gamma$ ("$W^+W^-_{\rm had}\gamma$")	5.949(2) fb	14.759(7) fb	2.48	12.271(4) fb	35.593(17) fb	2.90
$pp \to q\bar{q}\ell^+\ell^-\gamma$ ("$Z_{\rm had}Z_\ell\gamma$")	1.1982(6) fb	2.191(2) fb	1.83	2.4454(12) fb	4.753(5) fb	1.94
$pp \to q\bar{q}\ell^+\ell^-\gamma$ ("$W^+_{\rm had}Z_\ell\gamma$")	0.6727(3) fb	1.8122(10) fb	2.69	1.3085(6) fb	4.194(2) fb	3.21
$pp \to \ell^+\nu_\ell q\bar{q}\gamma$ ("$W^+Z_{\rm had}\gamma$")	1.9704(9) fb	5.426(3) fb	2.75	3.9296(18) fb	13.160(8) fb	3.35
$pp \to q\bar{q}\ell^+\ell^-\gamma$ ("$W^-_{\rm had}Z_\ell\gamma$")	0.38156(15) fb	1.0739(7) fb	2.81	0.8740(4) fb	2.876(2) fb	3.29
$pp \to \ell^-\bar{\nu}_\ell q\bar{q}\gamma$ ("$W^-Z_{\rm had}\gamma$")	1.0121(4) fb	3.192(2) fb	3.15	2.3662(10) fb	8.950(7) fb	3.78

Table 3: Integrated cross sections for tri-boson production processes for the LHC running at a center-of-mass energy of 8 and 14 TeV. Results are given summed over all three lepton generations and, in case of quarks, all combinations which do not involve a top quark. The error in brackets is the statistical error from Monte Carlo integration.

in Section 3.5. Two processes, however, lead to even larger corrections. The first one is triple photon production. Here the relatively low invariant mass of the triple photon system gives rise to significant additional contributions from quark-gluon- and antiquark-gluon-initiated real-emission processes. Due to the steep rise of the gluon densities towards smaller x, this has a significant impact, as the typical energy scale for the photons is

set by its transverse momentum cut of 20 GeV, which is much smaller than the W and Z boson masses. The $W\gamma\gamma$ production process exhibits a particular feature at leading order not present in any of the other processes, a so-called radiation zero. This feature will be discussed separately at the end of this subsection.

The lower half of Table 3 shows the cross sections and K factors for the semi-leptonic production modes, where one of the massive gauge bosons or virtual photons decays into a pair of quarks. Similarly to the leptonic decays, the contributions of all combinations except those involving top quarks are summed. The Feynman diagrams for the semi-leptonic production modes are, after replacing the lepton with the corresponding quark, the same as those in the fully leptonic case. The decay quarks are required to appear as two additional jets in the final state, with transverse momentum, rapidity and R separation criteria as given in Eq. (40). NLO QCD corrections are only considered for the production side of the processes, the decays are simulated at leading order. In particular, gluon radiation off the decay quarks is not included. In general, the semileptonic processes exhibit much larger K factors than the corresponding fully leptonic process. The reason for this lies in the real emission part [30]. If the additional parton is hard and central enough and well separated from other objects, it forms an additional jet. On the other hand, the required number of final-state jets need not exceed the leading order one, so that soft and collinear extra emission is correctly simulated and the Cancelation of the divergences not spoiled. Hence, if the real emission generates an additional jet, the two decay quarks do not need to form two separate jets. One of them can fail the jet cuts, or both are clustered into a single jet. Additionally, the real-emission parton and a quark from the hadronic decay can cluster and form a single jet, while the decay quark alone might not have passed the jet cuts. These additional possibilities open up new regions of phase-space, and therefore lead to an enhancement of the real-emission cross section and thus to the enhanced K factors.

In Fig. 18, we show the dependence on the factorization and renormalization scale exemplarily for the $W^+Z\gamma$ production process. At leading order, this process shows only a mild dependence on the variation of the factorization scale, while there is no dependence on the renormalization scale as there is no strong coupling constant present. Varying the scale by a factor of 2 around the central value μ_0 gives a change in the cross section by 5.5%. Including NLO QCD corrections, we observe a large increase in the cross section, which is clearly outside the LO scale variation. The scale dependence on the factorization scale alone decreases slightly, as expected when going from LO to NLO. Simultaneously, however, a large dependence on the renormalization scale appears, which also dominates the joint variation of both scales. As α_s now appears in the NLO QCD contributions to the cross section, we observe the typical leading renormalization scale dependence. Varying both scales again by a factor 2 yields a change of 8.2% for the NLO cross section.

On the right-hand side of Fig. 18, we present the combined factorization and renormalization scale dependence for the individual contributions. The split into the different virtual contributions is according to the procedure described in Section 2, where all parts proportional to the Born matrix element are grouped together in the "Virtual-Born" contribution and the "Virtual-box" and "Virtual-pentagon" parts only contain the finite piece from BoxLine and PenLine contributions. We also note that only the total cross section is a physical observable and the split into individual contributions is scheme-dependent. Nevertheless, it is instructive to see that we obtain almost all the scale dependence of the NLO result from the real emission part, which contains the actual real-emission cross section, the dipole terms of the Catani-Seymour subtraction scheme and also the collinear counter terms. In contrast, the Born amplitude and the parts of the virtual corrections which are proportional to it yield the bulk of the NLO cross section. At the central scale choice, its value is twice as large as the real emission. The finite remainders of the box and pentagon diagrams give only a small contribution.

In Fig. 19, we present the scale variation of a semi-leptonic tri-boson production process, taking $W^+W^+W^-_{\text{had}}$ production as an example. The situation is very similar to the fully leptonic case shown before. At LO, only a mild dependence on the factorization scale of 2.8% is present, while at NLO the leading order-type renormalization scale behaviour exhibits a much larger dependence. For a joint variation by a factor of 2 up and down, the NLO cross section changes by 12.5%. Looking at the contribution of the individual pieces on the right-hand side of Fig. 19, the situation is also very similar to that of Fig. 18. The only significant difference is the larger size of the real-emission part compared to the Born cross section and virtual corrections proportional to it. As explained before, this is due to the appearance of additional phase-space regions opening up. The criterion of two final-state jets can also be partly fulfilled by the extra emission of the real radiation process, allowing one of the decay quarks outside the jet definition regions.

As a last example in Fig. 20, we also investigate the scale dependence for leptonic $W^+\gamma\gamma$ production, which is associated with a larger K factor compared to the other

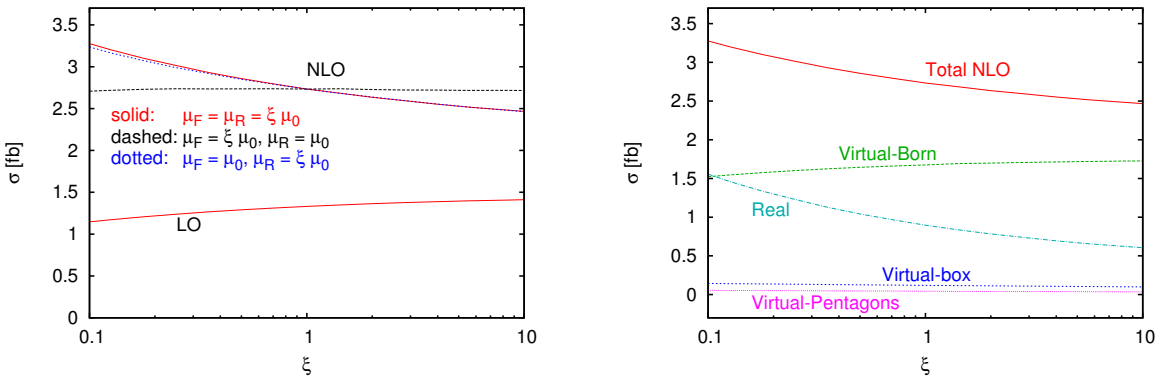

Figure 18: *Left:* Scale dependence of the total LHC cross section at $\sqrt{s} = 14\,\text{TeV}$ for fully leptonic $W^+Z\gamma$ production at LO and NLO. The renormalization and factorization scales are varied together or independently in the range from $0.1 \cdot \mu_0$ to $10 \cdot \mu_0$. *Right:* Joint factorization and renormalization dependence of the individual NLO contributions.

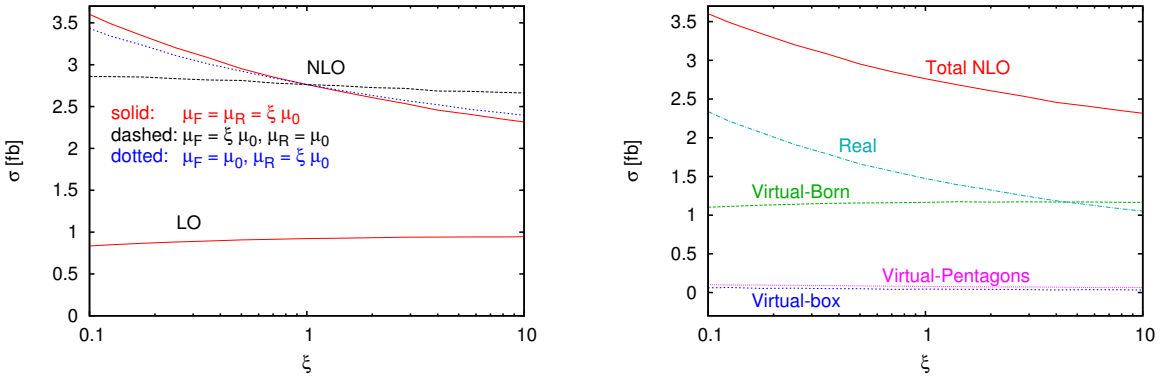

Figure 19: Similar to Fig. 18 but for semi-leptonic $W^+W^+W^-_{\text{had}}$ production.

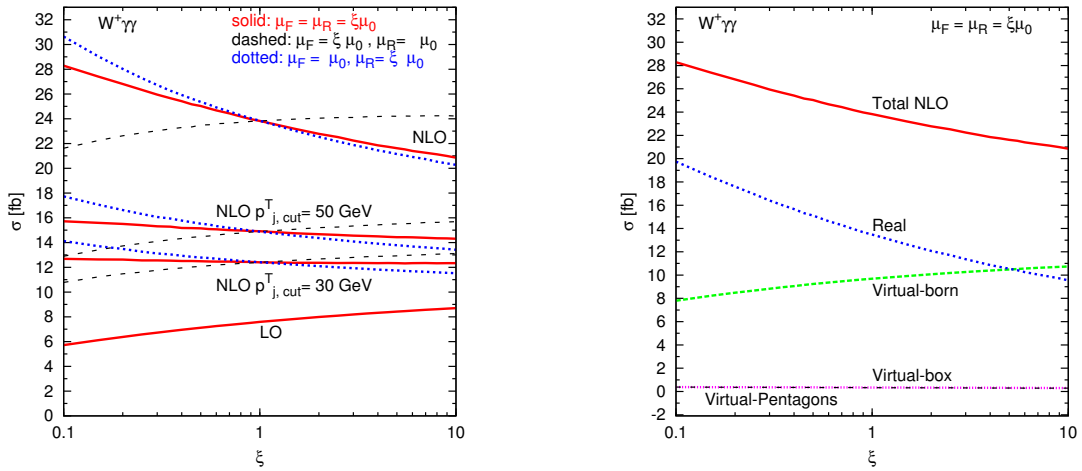

Figure 20: Similar to Fig. 18 but for leptonic $W^+\gamma\gamma$ production. Figures adapted from Ref. [28].

fully leptonic channels. On the left-hand side, we present the dependence on the factorization and renormalization scales individually and also for a joint variation. For the NLO case in the left panel, in addition to the case where extra parton emission is not restricted, we also show two sets of curves where a jet veto is applied, rejecting any events with identified jets with a transverse momentum larger than 50 and 30 GeV, respectively. The general picture is similar to the cases already discussed above. The scale uncertainty at NLO is about 10% when varying the factorization and renormalization scales jointly up and down by a factor of two. It is largely driven by the renormalization scale dependence, which has a negative slope with increasing scale, while the factorization scale dependence exhibits the opposite behavior. The NLO K-factor is significantly larger than the scale variation band at leading order. Comparing with the two curves which include a jet veto, we see that real emission gives a significant contribution to the total NLO cross section. Also the dependence on the renormalization scale is much reduced in this case. However, this should not be interpreted as a smaller uncertainty of the vetoed cross section [86]. Cancelation from different regions of phase space is the main source of this reduction, and therefore the small variation is cut-dependent. On the right-hand side of Fig. 20, the individual contributions to the unvetoed case are plotted separately. Consistent with our previous findings, the real emission part yields a significant contribution to the total cross section and is mainly responsible for its scale dependence. Similar to earlier cases, the finite remainders of the virtual box and pentagon diagrams are again small and show only a very mild scale dependence.

Finally, we investigate the impact of the NLO QCD corrections on differential distributions. As an example the fully leptonic $W^+W^-Z_\ell$ production process is chosen. In Fig. 21, we show the differential cross section with respect to the momentum of the leading charged lepton, i.e. the one with the largest transverse momentum. On the left-hand side, we present the results for the LO and NLO cross sections. For the latter, we also give results for the case where we have imposed a veto on all jets with a transverse momentum larger than 50 GeV. On the right-hand side, the differential K factor as defined in Eq. (7) is plotted, again for the two cases without and including an additional jet veto. We observe that the K factor without jet veto is not constant, but shows a strong dependence on the momentum scale. For small values, where the bulk of the cross section lies, it is close to the integrated one. For larger transverse momenta, we see much bigger K factors, which extend up to values of two. When including an additional jet veto, the situation looks different. For small transverse momentum, the effect of the jet veto is moderate. At larger values, configurations where the leading lepton recoils against the jet from the real emission process are now removed, and therefore the differential K factor decreases again. Depending on the value of the jet veto cut, the vetoed NLO cross section can become smaller than the LO one. In both cases, approximating the NLO QCD corrections with the LO distributions multiplied with the inclusive K factor is not a good estimate. For a reliable modeling of the distributions, one needs a full NLO calculation of the differential distribution. The leading-lepton distribution shown here is not a special case. Many distributions exhibit a similar behavior.

As another example, we consider the invariant mass of the four charged leptons in the same process. The results are shown in Fig. 22. We observe the largest effect for fairly small invariant four-lepton masses below the peak of the differential cross section at 200 GeV. The K factor shows structure in the threshold region, as the position of the cross section maximum shifts when going from LO to NLO. The reason for this is lepton recoil against the extra parton emission, which makes it easier to satisfy lepton transverse momentum cuts. This can also be observed when looking at the curve with an additional jet veto. While the basic features are similar, the amplitude of the effect is much smaller. Above 300 GeV, the K factor curves only show a mild dependence on the invariant 4-lepton mass, with slightly decreasing values when going to larger invariant masses.

$W\gamma\gamma$ production

As mentioned before, the $W^\pm\gamma\gamma$ production process takes a special role due to the appearance of a so-called radiation zero. Following the discussion given in Ref. [28], we start with the general theorem of Ref. [87]. It implies that the SM amplitude for the process $q\bar{Q} \to W^\pm\gamma\gamma$ vanishes for $\cos\theta^*_W = \pm\frac{1}{3}$, when the two photons are collinear. Here, θ^*_W denotes the angle between the incoming quark and the W boson in the partonic center-of-mass frame. Extra emission only preserves this radiation zero when it is electromagnetically neutral (e.g. gluonic), and collinear to the two photons. Therefore, the gluon-induced channels in the real-emission part do not exhibit this feature. Due to the steep rise of the gluon PDFs towards smaller proton momentum fraction x, these channels form an important contribution at the LHC. Hence, the additional QCD emission appearing as NLO contribution to $W^\pm\gamma\gamma$ production is expected to spoil the radiation zero. The same feature has also been observed in the $W^\pm\gamma$ process [88].

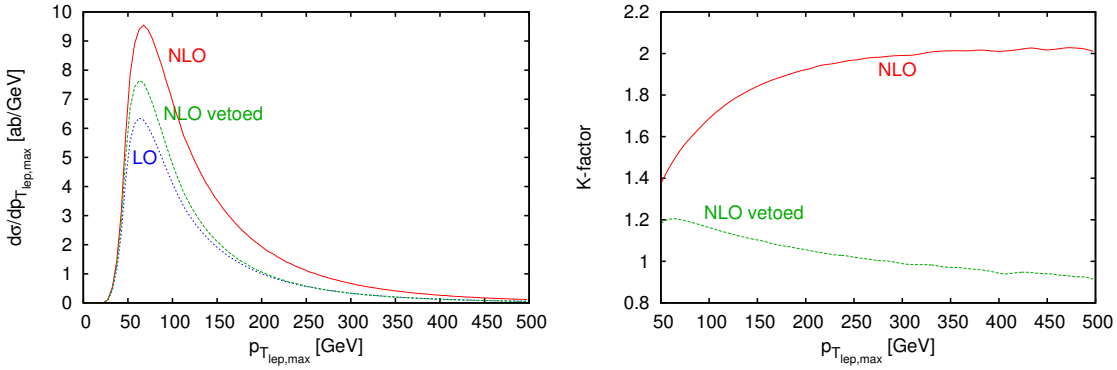

Figure 21: *Left:* Transverse momentum distribution of the charged lepton with the highest transverse momentum at LO, NLO and NLO with additional jet veto for the fully leptonic $W^+W^-Z_\ell$ production process at the LHC at $\sqrt{s} = 14\,\text{TeV}$. *Right:* Differential K factor as defined in Eq. (7) for the inclusive case and with an additional veto on jets with $p_{T,j} > 50\,\text{GeV}$.

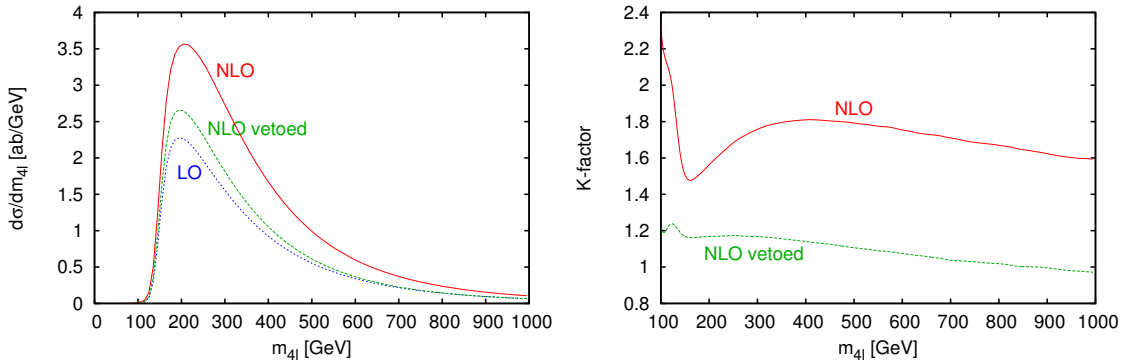

Figure 22: Same as Fig. 21, but for the invariant mass of the four charged leptons.

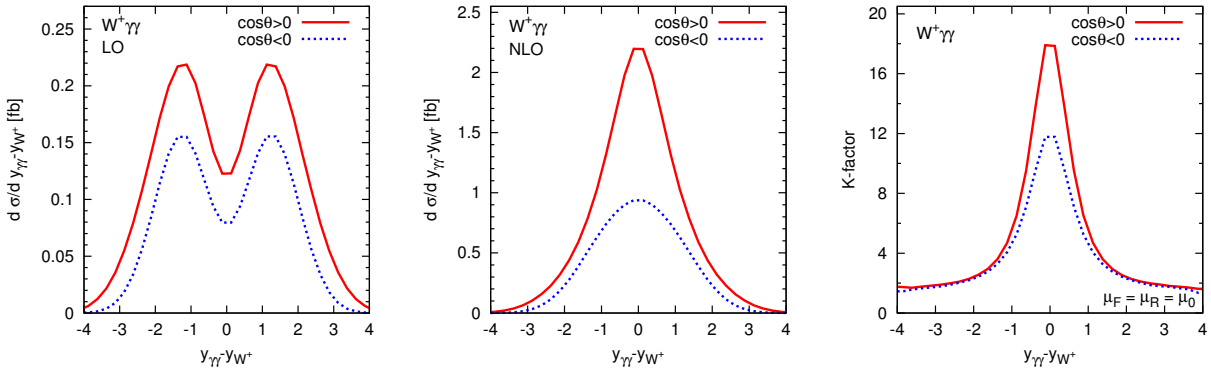

Figure 23: Distribution in rapidity separation between the W and the photon pair, with the photons in the same ($\cos\theta > 0$) or opposite ($\cos\theta < 0$) hemispheres, at LO (left), NLO (center) and K factor (right) for the fully leptonic $W^+\gamma\gamma$ production process at the LHC at $\sqrt{s} = 14\,\text{TeV}$. Besides the cuts of Eq. (40), an additional cut on $M_{T,l\nu} > 70\,\text{GeV}$ is applied. Figures adapted from Ref. [28].

Around $\cos\theta^*_W = \pm\frac{1}{3}$, real radiation therefore leads to a strong increase in the cross section, contributing to the large total K factor for this process.

Following Ref. [89], we can investigate the radiation zero by looking at the rapidity difference of the photon pair system and the W, $y_{\gamma\gamma} - y_W$. The rapidity of the W is reconstructed from the observed charged lepton and the missing transverse momentum originating from the neutrino. To suppress photon radiation off the charged final-state lepton, we impose an additional cut on the transverse mass of the charged lepton and the neutrino, $M_{T,\ell\nu} > 70\,\text{GeV}$. This is close to the kinematical limit for on-shell Ws and strongly reduces final-state photon emission. Results for $W^+\gamma\gamma$ production are shown in Fig. 23. $W^-\gamma\gamma$ production behaves similarly.

As the LHC is a proton-proton collider, quark and anti-quark will originate equally likely from proton 1 and proton 2, and at the position of the radiation zero the finite contribution of the other possibility gets superimposed. Therefore, we do not expect to see an actual radiation zero, but a dip at zero separation. The degeneracy could be lifted by signing the quark direction according to the overall boost of the event along the beam axis [90], but this option is not pursued further here. At LO, depicted in Fig. 23 on the left, we indeed observe the expected strong dip at zero rapidity separation, both for photons lying in the same ($\cos\theta > 0$) and opposite ($\cos\theta < 0$) hemispheres in the laboratory frame. Moving on to NLO shown in Fig. 23 in the middle, the dip is completely filled in by the extra radiation, leading now to a peak at zero rapidity separation. The same effect is also visible in the K factor plot on the right, where huge differential K factors appear. These are in a region where the bulk of the cross section is, thereby giving also rise to large integrated K factors as observed in Table 3. This behavior is in contrast to the other processes, see e.g. Fig. 21, where large K factors are associated with phase space regions contributing only marginally to the total cross section.

3.4. Multi-boson production with one jet

In this section, we report results at NLO QCD for several processes involving one jet, namely [31–37],

$$pp \to j l_1^\pm \nu_{l_1} H + X \qquad (\text{“}W^\pm H j\text{”}), \qquad (67)$$
$$pp \to j l_1^+ \nu_{l_1} l_2^- \nu_{l_2} + X \qquad (\text{“}WWj\text{”}), \qquad (68)$$
$$pp \to j l_1^\pm \nu_{l_1} l_2^+ l_2^- + X \qquad (\text{“}W^\pm Z j\text{”}), \qquad (69)$$
$$pp \to j l_1^\pm \nu_{l_1} \gamma + X \qquad (\text{“}W^\pm \gamma j\text{”}), \qquad (70)$$
$$pp \to j l_1^\pm \nu_{l_1} \gamma\gamma + X \qquad (\text{“}W^\pm \gamma\gamma j\text{”}), \qquad (71)$$

We will refer to them by the on-shell name for simplicity. Results for the remaining di-boson+ jet production processes are also known at NLO QCD [91–101]. For this class of processes, the virtual amplitudes can be computed using the abelian and non-abelian building blocks and the closed quark-loop diagrams described in Section 2.3. Due to the use of leptonic tensors (see Section 2.2), the QCD calculation can be shared among a subset of processes facilitating the validation of the calculation. A representative set of the contributing virtual diagrams for “$W^\pm H j$” production is shown in Fig. 24.

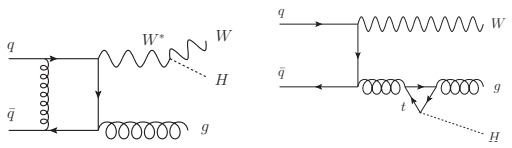

Figure 24: The virtual contributions to WHj production at NLO QCD can be divided into two classes. For Drell-Yan like diagrams (left) the Higgs boson is radiated off a W boson. The Higgs boson may also be attached to a heavy-quark loop, as shown on the right.

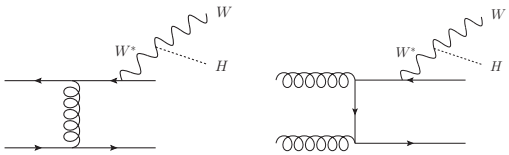

Figure 25: Representative diagrams for real emission contributions to WHj production at NLO QCD. External partons are either four quarks (left) or two quarks and two gluons (right).

Note that for the processes (67-71), as part of the real corrections, new sub-processes appear for the first time, in particular the gg initiated sub-processes and also sub-processes with two quark lines (see Fig. 25 for “$W^\pm H j''$ production). Thus, potentially large NLO corrections could appear not only due to the completely new contributing sub-processes, but also due to the fact that phase space regions can be populated by opening up new topologies at NLO, for example, double soft and collinear weak emissions (see Fig. 26).

For the numerical results in this section, we use the input parameters and cuts defined in Eqs. (38), (39) and (40). For the jet definition we slightly lower the required

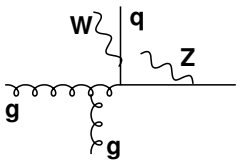

Figure 26: Example of new subchannel and topology appearing at NLO for WZj production.

LHC $\sqrt{s} = 8\,\text{TeV}$	Inclusive			Exclusive	
Process	σ_{LO}	σ_{NLO}	K	σ_{NLO}	K
$pp \to \ell_1^+ \nu_{\ell_1} \ell_2^- \bar{\nu}_{\ell_2} j$ ("$W^+W^- j$")	879.17(5) fb	1253.8(3) fb	1.43	1155.0(3) fb	1.31
$pp \to \ell_1^+ \nu_{\ell_1} \ell_2^+ \ell_2^- j$ ("W^+Zj")	72.954(9) fb	101.78(5) fb	1.40	90.13(4) fb	1.24
$pp \to \ell_1^- \bar{\nu}_{\ell_1} \ell_2^+ \ell_2^- j$ ("W^-Zj")	43.402(7) fb	62.47(2) fb	1.44	55.42(2) fb	1.28
$pp \to \ell^+ \nu_\ell \gamma j$ ("$W^+\gamma j$")	3984.7(5) fb	5570(2) fb	1.40	5082(3) fb	1.28
$pp \to \ell^- \bar{\nu}_\ell \gamma j$ ("$W^-\gamma j$")	3043.9(2) fb	4424(1) fb	1.45	4073(2) fb	1.34
$pp \to \ell^+ \nu_\ell \gamma\gamma j$ ("$W^+\gamma\gamma j$")	5.8895(3)fb	8.619(3) fb	1.43	7.380(2) fb	1.27
$pp \to \ell^- \bar{\nu}_\ell \gamma\gamma j$ ("$W^-\gamma\gamma j$")	4.411(1) fb	6.828(4) fb	1.55	5.979(5) fb	1.35
$pp \to \ell^+ \nu_\ell H j$ ("W^+Hj")	38.1866(13) fb	49.731(5) fb	1.30	47.149(4) fb	1.23
$pp \to \ell^- \bar{\nu}_\ell H j$ ("W^-Hj")	19.3204(6) fb	26.214(2) fb	1.36	24.859(2) fb	1.29

Table 4: Integrated cross sections for di-boson and $W\gamma\gamma$ plus one jet production processes for the LHC running at a center-of-mass energy of 8 TeV. Results are given summed over all three lepton generations. The error in brackets is the statistical error from Monte Carlo integration.

LHC $\sqrt{s} = 14\,\text{TeV}$	Inclusive			Exclusive	
Process	σ_{LO}	σ_{NLO}	K	σ_{NLO}	K
$pp \to \ell_1^+ \nu_{\ell_1} \ell_2^- \bar{\nu}_{\ell_2} j$ ("$W^+W^- j$")	2059.7(1) fb	2850.7(6) fb	1.38	2517.4(4) fb	1.22
$pp \to \ell_1^+ \nu_{\ell_1} \ell_2^+ \ell_2^- j$ ("W^+Zj")	168.84(2) fb	228.48(3) fb	1.35	189.75(5) fb	1.14
$pp \to \ell_1^- \bar{\nu}_{\ell_1} \ell_2^+ \ell_2^- j$ ("W^-Zj")	116.75(1) fb	161.43(2) fb	1.38	135.14(3) fb	1.16
$pp \to \ell^+ \nu_\ell \gamma j$ ("$W^+\gamma j$")	8243.2(4) fb	11339(1) fb	1.38	9989(1) fb	1.21
$pp \to \ell^- \bar{\nu}_\ell \gamma j$ ("$W^-\gamma j$")	6893.8(3) fb	9728(2) fb	1.41	8675(2) fb	1.26
$pp \to \ell^+ \nu_\ell \gamma\gamma j$ ("$W^+\gamma\gamma j$")	13.9215(5) fb	19.902(2) fb	1.43	16.042(8) fb	1.15
$pp \to \ell^- \bar{\nu}_\ell \gamma\gamma j$ ("$W^-\gamma\gamma j$")	11.4093(2) fb	16.932(3) fb	1.48	14.037(7) fb	1.23
$pp \to \ell^+ \nu_\ell H j$ ("W^+Hj")	90.379(3) fb	113.06(10) fb	1.25	104.205(9) fb	1.15
$pp \to \ell^- \bar{\nu}_\ell H j$ ("W^-Hj")	51.748(2) fb	67.120(5) fb	1.30	61.914(6) fb	1.20

Table 5: Integrated cross sections for di-boson and $W\gamma\gamma$ plus one jet production processes for the LHC running at a center-of-mass energy of 14 TeV. Results are given summed over all three lepton generations. The error in brackets is the statistical error from Monte Carlo integration.

minimum transverse momentum to

$$p_{T,j} > 20\,\text{GeV}\,. \tag{72}$$

As PDFs, the CTEQ6L1 [75] set at LO and the CT10 set [76] with $\alpha_s(m_Z) = 0.1180$ at NLO are used. The CKM matrix is assumed diagonal and the calculation is performed in the five-flavor scheme, where the five lightest quarks are taken as massless and included in the running of α_s and the gluon-to-quark splitting. As discussed in Section 3.3 for tri-boson production, processes with external top quarks are not considered. For WHj production, we have also computed the effects of a non-diagonal CKM matrix and the effect of considering the four-flavor scheme instead of the five-flavor scheme, where the bottom quark is taken as massive. The changes due to these approximations are below 2% at NLO. Anomalous couplings as given in Section 2.6 are implemented for all processes, except for WWj production. As renormalization and factorization scales, we use the invariant mass of the electroweak system, i.e.

$$\mu_{\text{F}} = \mu_{\text{R}} = \mu_0 = \sqrt{\left(\sum_{i\in\ell,\nu,\gamma,H} p_i\right)^2}\,, \tag{73}$$

if not stated otherwise. As in the previous section, numerical results are summed over all three lepton generations, neglecting interference effects from identical leptons in the final state, which are small.

The scale variation for WHj production is shown in Fig. 27. We only provide results for on-shell Higgs production, since off-shell effects contribute at the per mille level. Choosing different scale definitions gives

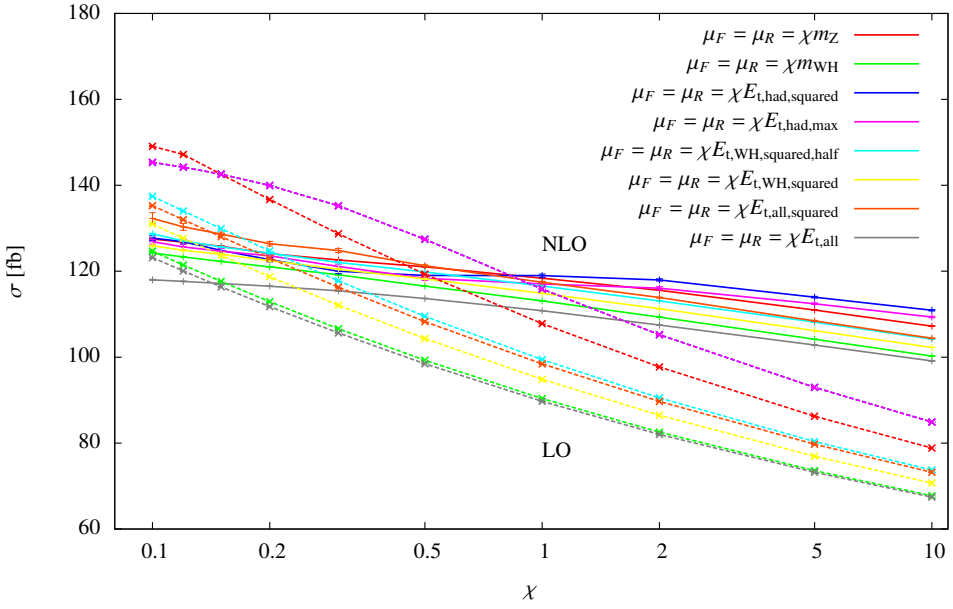

Figure 27: The LO and NLO cross section for WHj production is shown with different choices for $\mu_F = \mu_R = \mu_0$. The scale choices are based on common choices for di-boson production, including linear sums or sums of squares of the transverse energy of the electroweak particles and/or jets in the final state. The choice of a different scale will typically lead to a deviation on the same order as varying the scale by a factor $2^{\pm 1}$, such that a conservative estimate of the scale dependence should consider multiple scale definitions.

additional insight on the scale dependence compared to the typical variation of a given scale by a factor $2^{\pm 1}$. One can see that the fixed scale of $\mu_0 = M_Z$ is an outlier compared to the dynamical scales and overestimates the result. Among the dynamical scales, our default choice, the invariant mass of the electroweak system, which in this case is the WH invariant mass, yields a rather average value, making it a reasonable scale choice. Going from LO to NLO reduces both the dependence on the choice of scale and the variation for any given scale. Considering the WH invariant mass, the $\mu = 2^{\pm 1}\mu_0$ estimate gives a scale variation of the cross section of 19% and 6% at LO and NLO, respectively.

In Fig. 28 we present the scale variation plots for the "$W^+\gamma\gamma j$" production process, taking as central scale our default choice of the invariant mass of the electroweak system. In the left panel, in addition to the LO and NLO curves, the different parts contributing at NLO are given. "Virtuals + born" gather the virtual corrections plus the LO cross section evaluated with NLO PDFs. The "Reals" contain the real-emission contribution, the dipole terms from the Catani-Seymour subtraction scheme and the finite collinear terms. "Reals-veto" is the same, but rejecting events in which the second jet has a transverse momentum larger than 50 GeV. Correspondingly, "NLO-veto" denotes the total cross section at NLO applying a veto on additional jets. It is also called "exclusive" sample as opposed to the "inclusive" one where the jet veto is not applied. We observe in the plot that the strong scale dependence of the "Virtuals + born" and "Reals" contribution partly cancels in the sum. The cancelation is even stronger for the vetoed sample. This, however, as we will see below and as mentioned in the previous section, should not be taken as a stabilization of perturbation theory in the exclusive sample, but rather as an accidental cancelation between different regions of phase space, which are cut dependent. Differential distributions will show that the jet veto results in unreliable predictions in the tails of kinematic distributions. In the right panel, the LO and NLO cross sections are depicted with independent variations of the renormalization and factorization scales. They show that the renormalization scale drives most of the remaining scale uncertainty, with only a very mild factorization scale dependence. Overall, the scale uncertainty decreases at NLO down to the 10% level for the inclusive sample. For the 1-jet exclusive sample, as mentioned before, a naive scale uncertainty based on the typical variation of a factor $2^{\pm 1}$ around the central scale underestimates the theoretical errors. A more detailed discussion on how to address the scale uncertainties in exclusive samples can be found in Ref. [86].

In Tables 4 and 5 the LO and NLO cross section val-

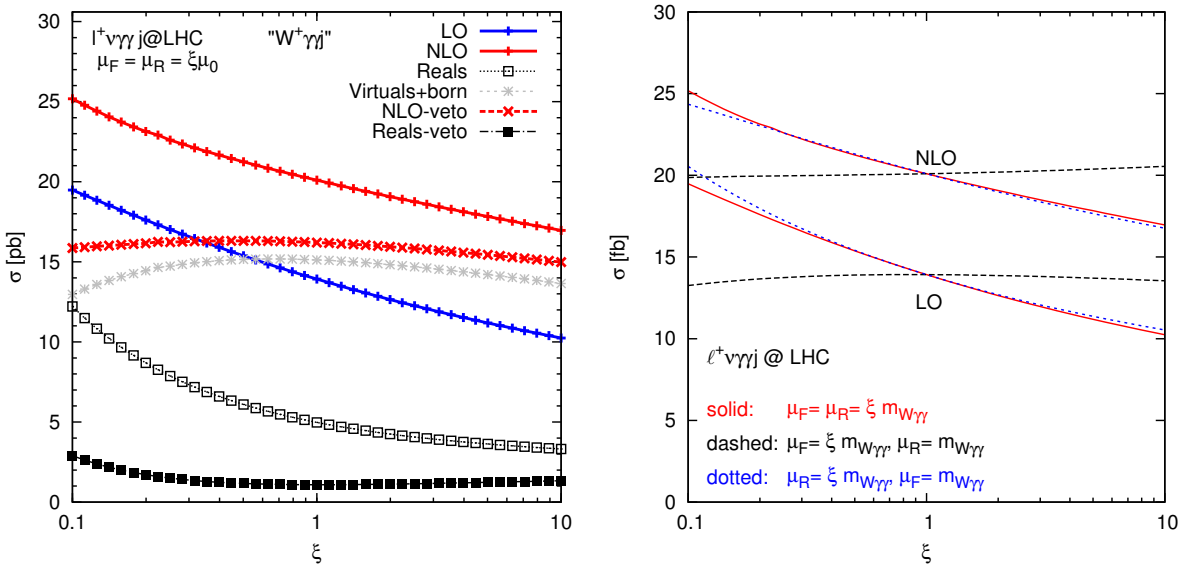

Figure 28: *Left:* Scale dependence of the total LHC cross section at $\sqrt{s} = 14\,\text{TeV}$ for $W^+\gamma\gamma j$ production at LO and NLO jointly varying the renormalization and factorization scales in the range from $0.1\,m_{W\gamma\gamma}$ to $10\,m_{W\gamma\gamma}$ for the individual contributions. *Right:* Scale variation at LO and NLO comparing a simultaneous variation of μ_R and μ_F with separate variation of the two scales.

ues at the central scale for the LHC operating at a center of mass energy of 8 TeV and 14 TeV, respectively, are given. The numbers in parentheses denote the statistical error. The size of the NLO corrections at the total cross section level is on the order of 40%. Note that contrary to the large K factor showing up in $W\gamma\gamma$ production due to the radiation zero, the size of the corrections for $W\gamma\gamma j$ exhibits a size comparable to the other processes. This indicates on the one hand that the radiation zero is not present in LO $W\gamma\gamma j$ events and suggests convergence of perturbation theory, with smaller corrections as the multiplicity of the number of jets increases and all possible sub-processes and kinematical configurations are already covered at LO.

In the following, for the LHC at a center-of-mass energy of 14 TeV, we show differential distributions for several observables at LO and NLO, including the effect of applying a veto on the second jet. For the charged EW final states, results will be given for the positive charge channel. Similar features apply for the charge-conjugated ones. In Fig. 29, jet observables are considered for the "$W^+\gamma j$","W^+Zj" and "W^+W^-j" production processes. In the top panels, the transverse momentum distributions of the hardest jet are shown. The NLO inclusive K factor ranges from 1.3 to 1.7, with a homogeneous distribution of the scale uncertainty in the whole spectrum. For the vetoed distributions, the corrections are large and negative, with K factors below 0.5, and strong variations in the scale uncertainties. They range from 0%, which is unrealistic, close to 120 GeV due to the crossing of the $2\mu_0$ and $0.5\mu_0$ bands, to 200% in the tail of the differential distributions, where the presence of large logarithms of the type $\log(Q/p^j_{T,cut})$, with Q a typical scale of the hard process, spoils the convergence of perturbation theory. In the lower row, the rapidity distribution of the leading jet is plotted, yielding K factors ranging from 1.3 to 3.5. The non-trivial phase space dependence exhibited by the NLO corrections highlights their relevance and the fact that LO differential distributions rescaled by integrated total K factors might result in large errors. Analogously, in Fig. 30, the transverse momentum distribution of the hardest lepton is plotted with K factors ranging from 1.5 to 1.3.

Finally, in Fig. 31, $W\gamma\gamma j$ production is considered and the distributions of the transverse momentum of the hardest jet (left), the invariant mass of the electroweak system (middle) and the separation of the two photons (right) are plotted. Again, the NLO corrections show a non-trivial phase space dependence. Particularly large K factors appear for values of the separation of the two photons larger than π. In this phase space region, the electroweak system favors recoil against additional jet emissions opening up at NLO.

In the following, for "WHj" and "WZj" production, we study in more detail the phase space dependence of the jets and the electroweak system and their relative

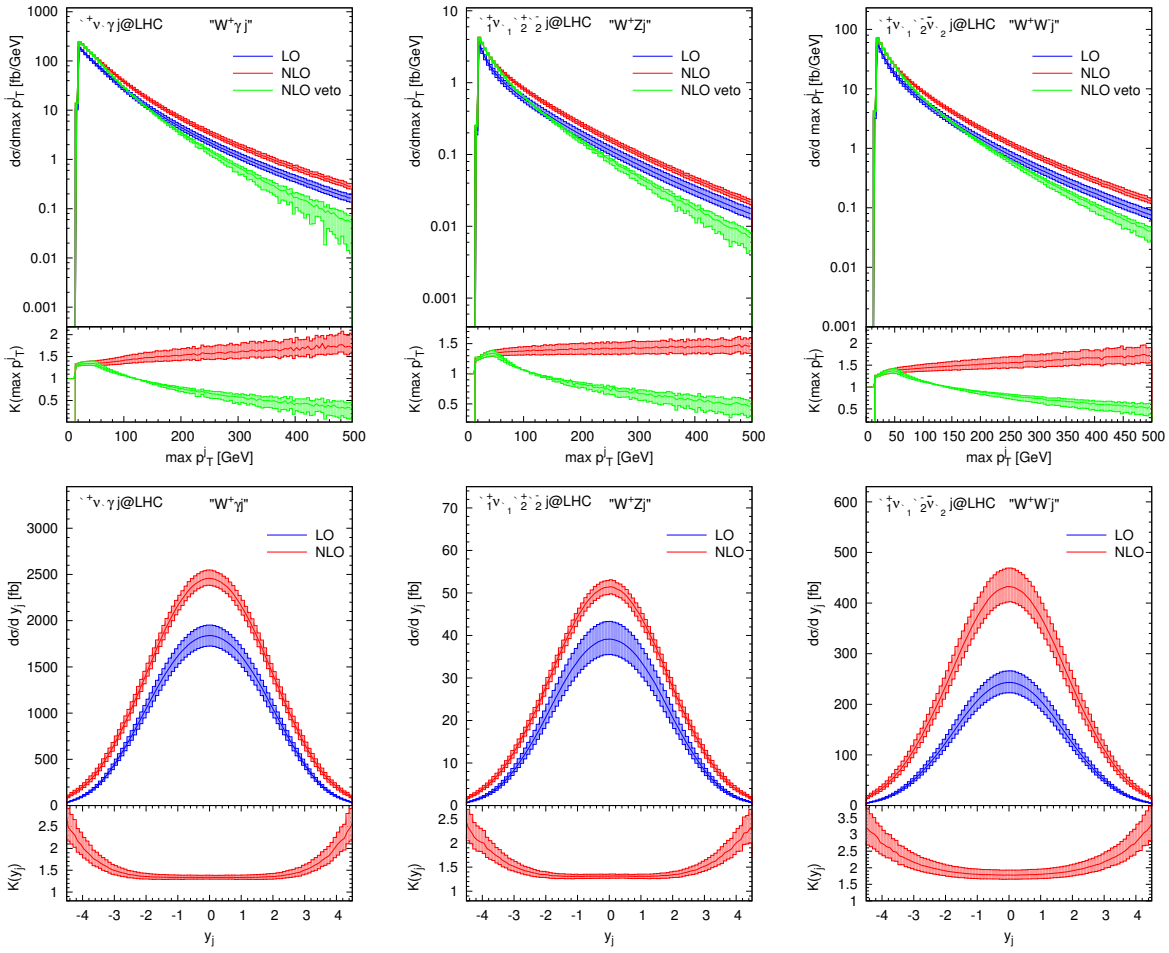

Figure 29: Differential cross sections for $pp \to \ell^+ \nu_\ell \gamma j + X$ (left panels), for $pp \to \ell_1^+ \nu_{\ell_1} \ell_2^+ \ell_2^- j + X$ (middle panels) and for $pp \to \ell_1^+ \nu_{\ell_1} \ell_2^- \bar{\nu}_{\ell_2} j + X$ (right panels) showing the distribution of the transverse momentum (top row) and the rapidity (bottom row) of the leading jet. The bands in the big panels describe scale variations by a factor of two around the central scale. The K factor bands are due to the scale variation of the NLO results with respect to $\sigma_{LO}(\mu_0)$. For the top row we also include one-jet exclusive results at NLO.

hardness, closely following the discussion in Ref. [31]. This is important in connection with AC searches, since the sensitivity to BSM physics increases for large invariant masses of the electroweak system. To visualize the phase space dependence for WVj events, it is necessary to consider their transverse momenta in aggregate. Only two variables out of the four independent transverse momentum components are needed after discarding an overall rotation in the transverse plane and anticipating approximate invariance of radiation patterns under rescaling at very high energies. We choose them to be the transverse energies of two of the three objects, normalized to the sum for all three, i.e. we take

$$x_{\rm jet} = \frac{\sum_{\rm jets} \mathrm{E}_{\mathrm{T},i}}{\sum_{\rm jets} \mathrm{E}_{\mathrm{T},i} + \sum_{W,Z/H} \mathrm{E}_{\mathrm{T},i}} \tag{74}$$

and, similarly, for $V \in (W, Z, H)$ we define

$$x_V = \frac{E_{TV}}{\sum_{\rm jets} \mathrm{E}_{\mathrm{T},i} + \sum_{W,Z/H} \mathrm{E}_{\mathrm{T},i}} \,. \tag{75}$$

Note that $x_{\rm jet} < 0.5$ at LO, where a single massless parton forms the jet system, which recoils against the other two objects, and that $x_{\rm jet} + x_W + x_{Z/H} = 1$. A value close to 0.5 for the $x_{\rm jet(H,Z)}$ observable would indicate that the given object has half of the total transverse energy of the system, recoiling against the rest, while values close to zero indicate that the particle is soft. Thus, we can use these observables to distinguish phase space regions with soft EW bosons from regions with soft jets in 2-dimensional Dalitz-like plots.

In Fig. 32, we show the NLO double differential distributions for WZj (left) and WHj (right) production

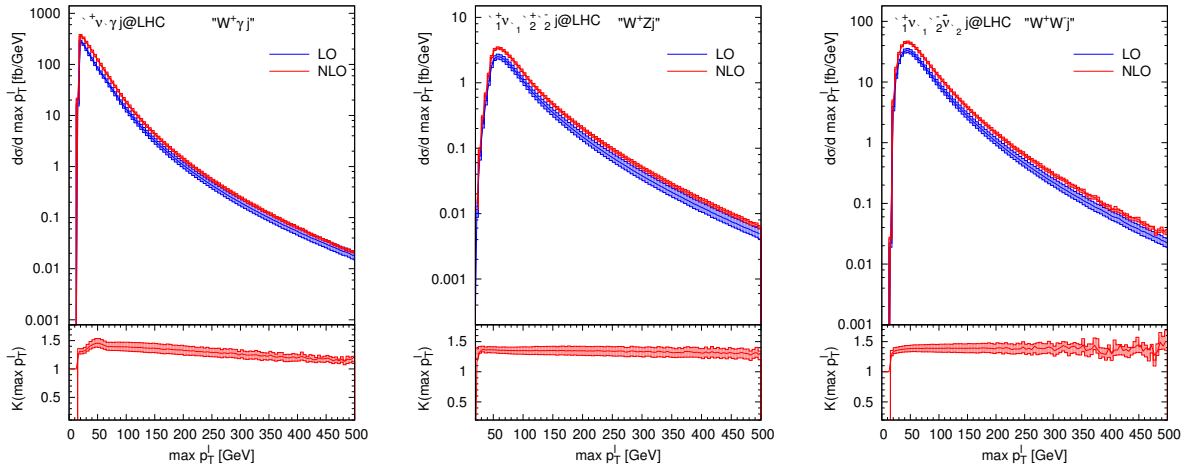

Figure 30: Differential cross sections for $pp \to \ell^+ \nu_\ell \gamma j + X$ (left panels), for $pp \to \ell_1^+ \nu_{\ell_1} \ell_2^+ \ell_2^- j + X$ (middle panels) and for $pp \to \ell_1^+ \nu_{\ell_1} \ell_2^- \bar{\nu}_{\ell_2} j + X$ (right panels) showing the distribution of the transverse momentum of the hardest lepton. The bands in the big panels describe scale variations by a factor of two around the central scale. The K factor bands are due to the scale variation of the NLO results with respect to $\sigma_{LO}(\mu_0)$.

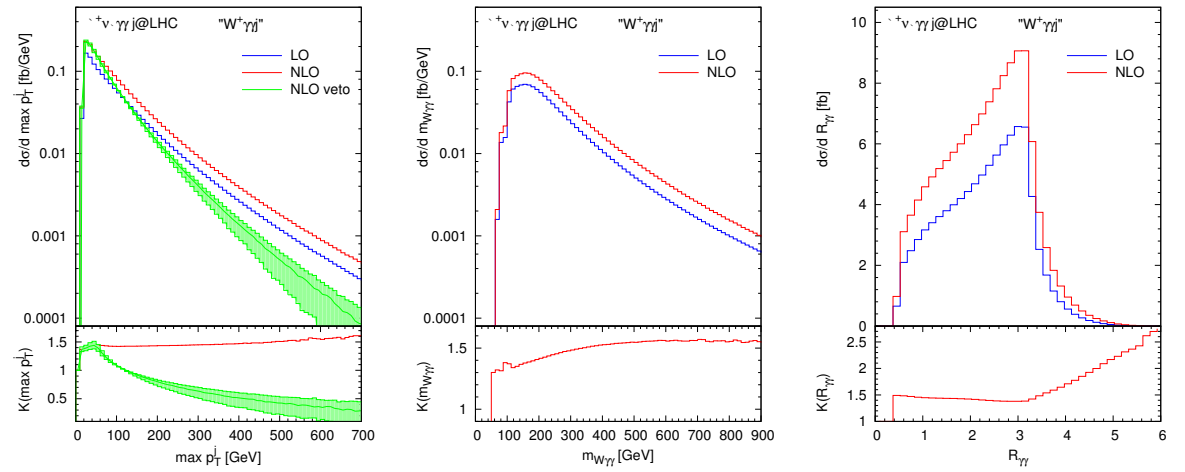

Figure 31: Differential cross sections for $pp \to \ell^+ \nu_\ell \gamma\gamma j + X$ showing the distribution of the transverse momentum of the leading jet (left), of the electroweak invariant mass (middle) and of the separation of the two photons (right). The bands of the p_T^j-distribution with a veto on additional jets are defined analogously to the ones of Fig. 29.

with respect to x_{jet} and $x_{Z/H}$. In the upper row, results for the inclusive cuts are shown. One observes that WZj production allows for harder jets, while WHj production is dominated by back-to-back WH pairs with only soft jets. In the lower row, simulating experimental WH searches, the boosted regime is plotted requiring that $p_{T,Z/H} > 200\,\text{GeV}$. With this cut, one can clearly observe the different radiation patterns of the WHj and WZj processes, which manifest the different partial wave decompositions of the WH/WZ final state. While WH production is mostly restricted to $J = 1$, since it arises from a virtual W, this is only a small contribution to WZ production. For WHj production, soft QCD radiation is preferred, while in the WZj case there are two equally important phase space regions, those with soft jets at small x_{jet} and those with a soft W boson at large x_{jet}. The latter kind of events can be considered as EW correction to Vj production. With a small invariant mass of the electroweak system, they are less sensitive to AC effects. An upper bound, e.g. $x_{\text{jet}} < 0.3$, provides a dynamical jet veto on these Vj production events and avoids potentially large logarithms of the form $\alpha_s^n \ln^{2n}(s/p_{\text{T},j,\text{veto}}^2)$, which must be expected for a fixed veto of jets above a minimal transverse momentum. In Section 4 we inves-

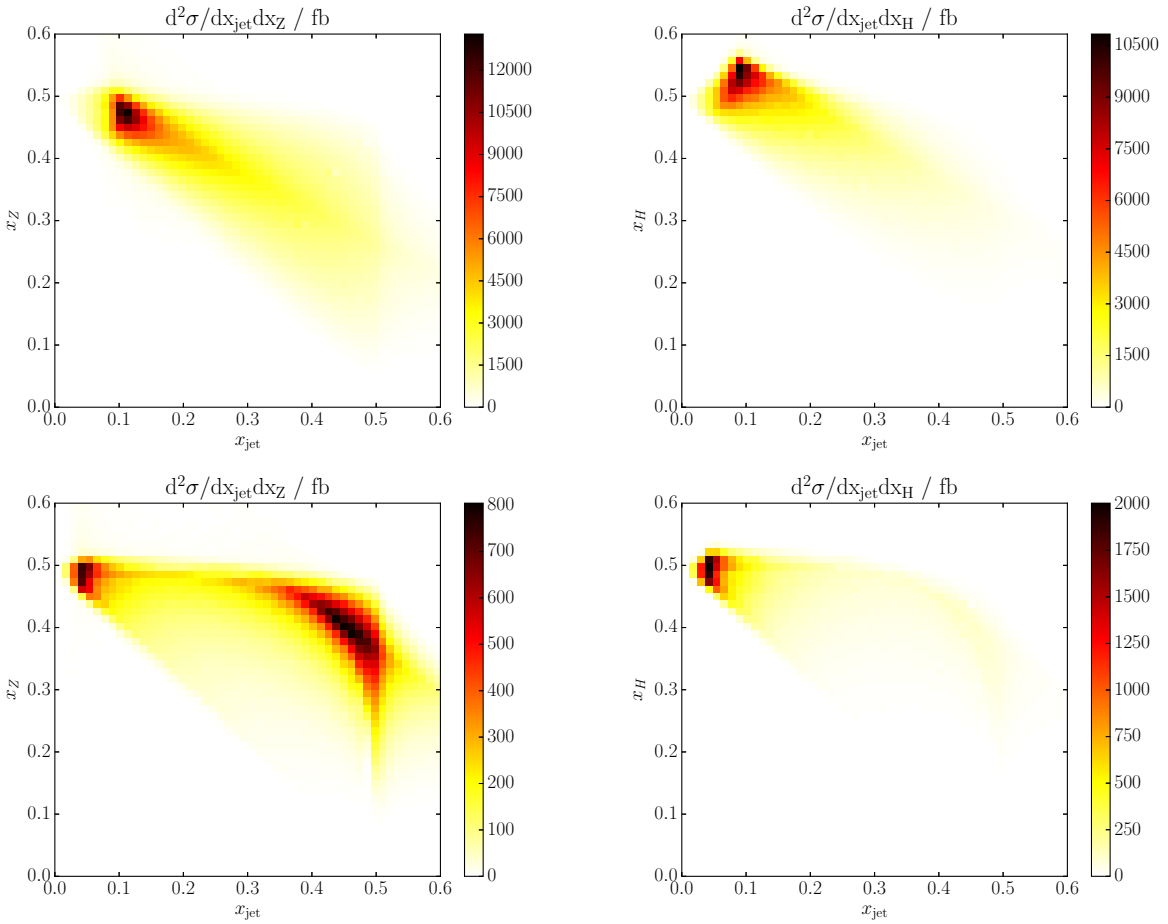

Figure 32: NLO double differential distributions for $e^+\nu_e\mu^+\mu^- j$ ($e^+\nu_e H j$) production on the left (on the right) with respect to $x_{\rm jet}$ and x_Z (x_H). Inclusive cuts are used in the upper row and boosted cuts ($p_{T,H(Z)} > 200\,\text{GeV}$) in the bottom panels.

tigate the effect of the dynamical jet veto in anomalous coupling searches for specific processes.

3.5. NLO electroweak corrections to multi-boson production

In this section, we report on NLO EW corrections to the production of a pair of massive gauge bosons (i.e. ZZ, W^+W^- and $W^\pm Z$) and, for the case of tri-boson, the production of W^+W^-Z. The final-state gauge bosons are assumed to be on-shell. This approximation provides a very good prediction of the total cross section and is very instructive to understand important effects, as the calculation is much simpler compared to the full calculation with leptonic decays. In the following, we apply no cuts at the level of on-shell $W^\pm$ and Z, since these will decay. The discussion presented below is based on Refs. [41, 42, 102].

The method to calculate NLO EW corrections follows similar steps to that of QCD corrections and has been well established. We use the Catani-Seymour subtraction method [4, 103] to deal with IR divergences. Concerning renormalization, we employ the G_F scheme, where the coupling α is calculated from the Fermi coupling constant and the gauge boson masses. We performed independent calculations with the help of automated tools. We used the programs `FeynArts/FormCalc` [104, 105] to generate the one-loop amplitudes. The one-loop integrals are calculated with the in-house library `LoopInts` based on Ref. [42], which agrees with another in-house implementation [106]. Our loop integrals have also been cross-checked against the program `LoopTools` [105, 107, 108] at the integrated cross section level for diboson production. `MadGraph` [109] and `HELAS` [48] routines are also used to compute tree-level amplitudes. Further details about the calculation and the precise defini-

tions of the various contributions discussed in the next section can be found in Refs. [41, 42]. In the following we highlight important phenomenological results we have obtained.

As a representative example, we show in Fig. 33 various EW corrections to the transverse momentum distribution of the W^+ for the case of W^+W^- (left) and of a Z for the case of ZZ (right) production. The full NLO EW correction is split into three components: the virtual correction including all the loop diagrams (with UV counter terms) and the endpoint contribution (which acts as an infrared counter term and is defined in Ref. [103]), the photon-quark induced contribution (labeled as γ induced in the plot) and the remainder of the photon radiated correction. We note that these subcorrections are UV and IR finite but dependent on the regularization scheme. Nevertheless, this separation is very instructive to see important effects. The first important effect is due to the virtual correction, which behaves like $-\alpha \log^2(p_{T,V}^2/M_V^2)$ with $V = W^+, Z$ and reaches about -30% for W^+W^- and -35% for ZZ at 600 GeV. This is the well-known Sudakov double logarithm arising from the exchange of a virtual massive gauge boson in the loops. This is in contrast to QCD corrections where a large distortion in a distribution is usually due to real-emission corrections with new kinematical configurations opening up. Photon-quark induced channels form a second important contribution to the EW correction. It behaves like $+\alpha \log^2(p_{T,W}^2/M_W^2)$ and reaches about $+25\%$ for the W^+W^- case at 600 GeV, which is just opposite to the virtual correction. This looks like an accidental cancelation and is unexpected because this contribution is proportional to the photon PDF, which is much smaller than the quark PDFs. It turns out that there is a new mechanism, which enhances the photon-quark induced contribution. This enhancement is due to the large amplitude of the process $\gamma u \to W^+ d$, which includes a t-channel W-exchange diagram. An additional soft W^- radiation on top of this hard amplitude produces the above double-logarithm behavior. This enhancement mechanism, which can also be seen as due to the $\gamma \to W^+W^-$ splitting, occurs also in the $W^\pm Z$ cases, but not in the ZZ case as can be seen from the right plot. Therefore, the photon-quark induced contribution is negligible in the latter. For the W^+W^- production, the photon-photon induced contribution, calculated at NLO, is also plotted. This contribution is smaller than 5%.

The above striking difference between the charged and neutral currents motivated us to re-examine the NLO QCD corrections to ZZ, W^+W^- and $W^\pm Z$ production modes. The full NLO QCD corrections to these processes have been calculated long time ago in Refs. [111–116]. These authors have found that the NLO QCD corrections are large, and for $p_{T,V}$ distributions, the corrections can reach a few hundred percent at large energies. The main reason is due to the gluon-quark induced sub-processes, where the hard process is $gq \to q'V$, producing a massive gauge boson with a large transverse momentum recoiling against a hard jet. Another soft gauge boson is then radiated on top of this hard process, as above mentioned. The large QCD corrections are due to the large cross section of the hard process and the Sudakov double-logarithm correction from a soft gauge boson emission. These important mechanisms are obviously common to all the three production modes, and hence one would expect that the NLO QCD corrections are of similar size. This turns out to be not the case, as can be seen from Fig. 34. There, we observe a hierarchy in the gluon-quark induced contribution, $\delta_{ZZ}^{gq} = \frac{1}{3}\delta_{WW}^{gq} = \frac{1}{6}\delta_{WZ}^{gq} \approx 120\%$ at 700 GeV. The first explanation presented in Ref. [114] takes into account the above important mechanisms, but the soft gauge boson is only radiated off the final-state quark. This provides a qualitative prediction of the large QCD corrections, but cannot explain the hierarchy as noted in Ref. [116]. We have extended this explanation by including all the possibilities of radiating a soft gauge boson, not only off the final-state quark but also off the initial-state quark and the hard gauge boson. This is indeed the full leading-logarithmic approximation. With this approach we can explain not only the above QCD hierarchy but also the more pronounced hierarchy in the photon-quark induced correction mentioned in the previous paragraph. Full analytical results of the leading-logarithmic approximation for the gluon-quark and photon-quark induced subprocesses have been presented in Ref. [41]. The calculation for the NLO EW case is quite involved, but simple results are obtained owing to similar behavior of the W, Z and γ in the high energy limit (i.e. $p_T \gg M_Z$).

As another example to show the importance of the photon-photon induced contribution, we plot in Fig. 35 the invariant mass of the W^+W^-Z system for the case of tri-boson production. We observe that the photon-photon contribution is important at large energies, reaching about $+10\%$ at $M_{WWZ} = 1.4$ TeV. Similar behavior is also found for W^+W^- production [41, 43]. This plot again shows the importance of the virtual and photon-quark induced corrections, with opposite behaviors. The total NLO EW correction is however very small due to the accidental cancelation between the virtual and photon-quark induced corrections, as in the case of W^+W^- production discussed above.

The above discussion shows the importance of the photon PDF, which is very weakly constrained at the present.

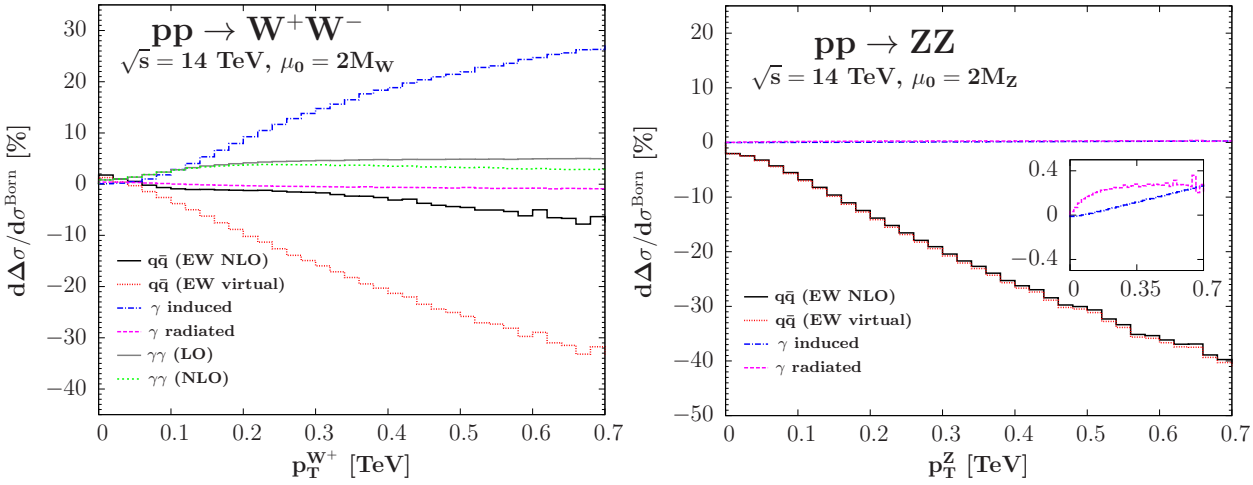

Figure 33: W^+ (left) and Z (right) transverse momentum distributions of the NLO EW corrections in W^+W^- and ZZ production modes, respectively. The MRST2004QED PDF set [110] is used. Figures taken from Ref. [41].

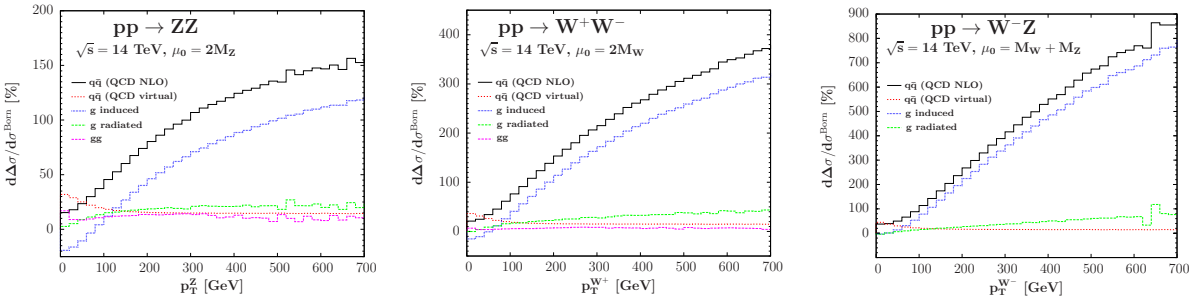

Figure 34: Z (left) W^+ (middle) and W^- (right) transverse momentum distributions of the NLO QCD corrections in ZZ, W^+W^- and W^-Z production modes, respectively. The MRST2004QED PDF set [110] is used. Figures taken from Ref. [102].

In the near future, when the LHC experimental errors of the di-boson analyses are reduced to the level of a few percent, the above photon induced contributions will be important. Together with dilepton production modes, the W^+W^- channel can provide strong constraints on the photon PDF, assuming the absence of new physics.

4. Anomalous coupling searches

In many of the processes discussed above, BSM effects in the electroweak sector have been included in the form of anomalous couplings of W, Z, photon and Higgs boson [2, 3]. In this section, we will show their effects, using $W\gamma j$, WZj and VBF Hjj production as examples. To measure and to distinguish different AC effects, all contributing operators have to be considered jointly. For simplicity, however, we will focus on a few selected operators in this section, namely the CP-even dimension-6 operators

$$\begin{aligned} O_W &= (D_\mu\Phi)^\dagger \widehat{W}^{\mu\nu}(D_\nu\Phi) \\ O_{WW} &= \Phi^\dagger\, \widehat{W}_{\mu\nu}\widehat{W}^{\mu\nu}\, \Phi \\ O_B &= (D_\mu\Phi)^\dagger \widehat{B}^{\mu\nu}(D_\nu\Phi) \\ O_{WWW} &= \mathrm{Tr}\left[\widehat{W}_{\mu\nu}\widehat{W}^{\nu\rho}\widehat{W}_\rho{}^{\mu}\right] \end{aligned} \tag{76}$$

which are given in the notation discussed in Section 2.6, and their CP-odd counterparts $O_{\tilde{WW}}$ and $O_{\tilde{WWW}}$, where one W-field strength is replaced by its dual. The global fit of Ref. [117] bounds the couplings in the range $f_W/\Lambda^2 \in [-5.6, 9.6]$ TeV^{-2}, $f_{WW}/\Lambda^2 \in [-3.2, 8.2]$ TeV^{-2} and $f_B/\Lambda^2 \in [-28, 11]$ TeV^{-2}, which is slightly more restrictive than the fit presented in Ref. [118]. The bounds for $f_{WWW}/\Lambda^2 \in [-14, 4.1]$ TeV^{-2} are obtained from LEP data [119].

In Fig. 36, for W^+Zj production, we show the differential distribution at NLO of the variable x_{jet}, defined in Eq. (74), for the SM and for different values of the anomalous f_W/Λ^2 coefficient. The LO SM predictions

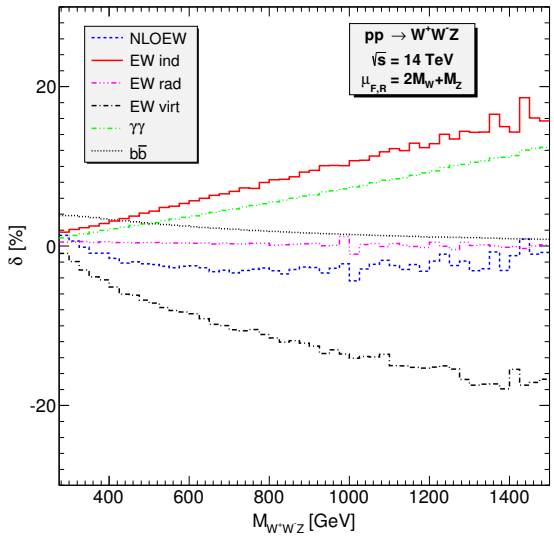

Figure 35: NLO EW corrections to the W^+W^-Z invariant mass in W^+W^-Z production. The photon PDF is calculated using the MRST2004QED program, while the quark and gluon PDFs are from MSTW2008 [80]. From Ref. [42].

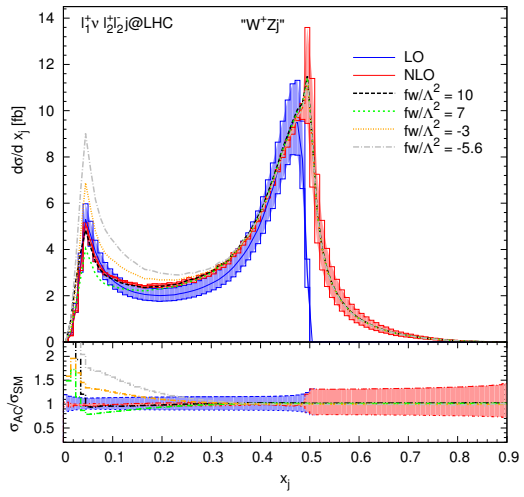

Figure 36: $x_{\rm jet}$ distribution for W^+Zj production with different values of anomalous couplings at NLO. Additionally, the LO and NLO SM results have been included for comparison. The bands correspond to a $\mu = \mu_{\rm F} = \mu_{\rm R}$ variation by a factor of 2 of the LO and NLO SM cross sections. In the lower panel, the ratio of the AC to the SM predictions at NLO and for the central scale is shown. Here, the bands correspond to the SM LO and NLO scale uncertainties with respect to μ_0, the invariant mass of the four decay leptons. The boosted cuts specified in Section 3.4 are used.

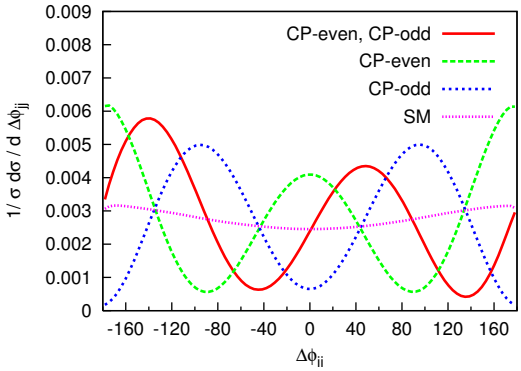

Figure 38: Normalized distribution of the azimuthal angle $\Delta\phi_{jj}$ for a Higgs mass of 120 GeV and a mixed CP scenario ($d = \tilde{d} = 0.18$, red solid curve), a CP-even anomalous coupling ($d = 0.18$, $\tilde{d} = 0$, green dashed curve), a CP-odd coupling ($d = 0$, $\tilde{d} = 0.18$, blue dotted curve) and the SM case (purple narrow dotted line). From Ref. [120].

are also shown to highlight the reduction of the scale uncertainties via the NLO corrections. In the figure, it is clearly visible that the sensitivity to AC effects is in the low $x_{\rm jet}$ region, corroborating that additional hard radiation dilutes the sensitivity to AC searches. Note the change on the sign of the AC contributions: For small values of f_W/Λ^2, its sign is important since the dominant term is the interference between SM and AC contributions. There is constructive/destructive interference for negative/positive couplings. For positive values, the cross section is suppressed at low transverse momenta. At high p_T, where the AC effects strongly dominate over the SM contributions, an increase in the cross section is generally expected.

In Fig. 37, we show the NLO transverse momentum distribution of the hardest lepton for $W^+\gamma j$ (left) and W^+Zj (right) production, applying boosted cuts and vetoing events with $x_{\rm jet} > 0.3$. Once again, the SM LO predictions are included for comparison. Note that the vetoed samples exhibit uniform, modest scale uncertainties in the whole spectrum. For $W^+\gamma j$ production, we vary simultaneously the anomalous coupling parameters f_{WWW} and f_B, while for W^+Zj the same set of parameters as used in Fig. 36 has been selected. Deviations from the SM are clearly visible, reaching enhancement factors up to 2 for W^+Zj and 10 for $W^+\gamma j$ production in the tails of the distributions, highlighting the potential of these processes to improve the constraints on AC couplings at the LHC.

AC coupling effects have been implemented in almost all of the VBF processes. As an example of the potential that these processes offer to quantify deviations from the SM predictions, results for VBF Hjj produc-

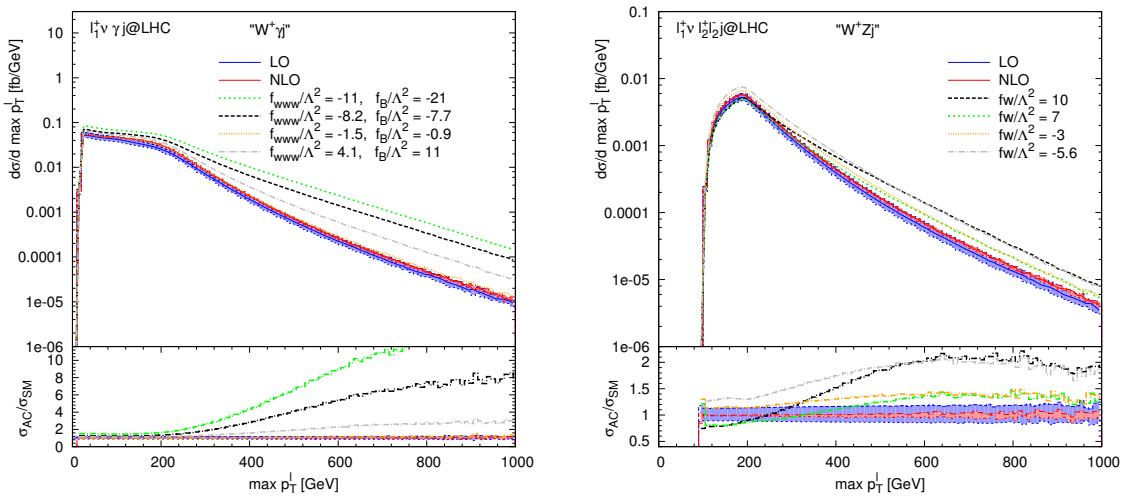

Figure 37: Differential distribution of the transverse momentum of the hardest lepton for $W^+\gamma j$ (left) and W^+Zj (right) events for different values of the AC at NLO. The bands in the big panels describe scale variations by a factor of two around the central scale. In the lower panel, the ratio of the AC to the SM predictions at the central scale at NLO are shown. Here, the bands correspond to the SM LO and NLO scale uncertainties with respect to μ_0. In addition to the boosted cuts specified in Section 3.4, $x_{\rm jet} < 0.3$ is required.

tion are shown as a final example. In Fig. 38, taken from Ref. [120], the normalized azimuthal angle distribution $d\sigma/d\Delta\phi_{jj}$ of the two tagging jets, defined by the difference of the azimuthal angles of the more-forward and the more-backward of the two tagging jets ($\Delta\phi_{jj} = \phi_{\rm F} - \phi_{\rm B}$), is plotted for the SM predictions and three purely AC scenarios. For the latter, the SM component a_1 of the general tensor structure of the HVV vertex, defined by

$$\begin{aligned} T^{\mu\nu}(q_1,q_2) =& a_1(q_1,q_2)\; g^{\mu\nu} + \\ & a_2(q_1,q_2)\; [q_1\cdot q_2 g^{\mu\nu} - q_2^\mu q_1^\nu] + \\ & a_3(q_1,q_2)\; \varepsilon^{\mu\nu\rho\sigma} q_{1\rho} q_{2\sigma}\;, \end{aligned} \tag{77}$$

has been set to zero. The CP-even (CP-odd) components correspond to non-zero values of a_2 (a_3) and are given by the $\tilde{d}$ parameter, $\tilde{d} = -m_W^2/\Lambda^2 f_{\widetilde{WW}}$ and show the characteristic dips at ±90 (0, ±180) degrees. For the mixed scenario, the dips are shifted. The fundamentally different distributions for the three principal cases highlight the potential of these processes to pin down the tensor structure of the HVV couplings.

5. Conclusion

Over the last decades, an enormous effort has been invested and great progress has been achieved by the theory community in the calculation of higher-order predictions for many complex, multi-particle processes at hadron colliders. Presently, NLO QCD corrections exist for most of the relevant signal and background processes needed not only at the LHC, but also at the Tevatron. To this program, we have contributed extensively in project B5. In this report, we have shown results for selected processes, namely, VBF Higgs and di-boson production, QCD-induced di-boson production in association with two jets, tri-boson and multi-boson plus one jet production processes. For all processes, we implemented leptonic decays of the vector bosons including all off-shell effects and spin correlations. Furthermore, for selected processes, we also consider semi-leptonic channels, which produce an experimentally more challenging signature, but one can benefit from larger branching fractions. Additionally, we have included BSM effects in most of the processes. This includes triple and quartic anomalous couplings.

NLO EW corrections will also be important for di- and tri-boson production at the LHC. We have also performed a detailed study of NLO EW effects for on-shell ZZ, W^+W^-, $W^\pm Z$ and W^+W^-Z production, thereby providing results for the total cross sections as well as various kinematical distributions. We found that while the NLO EW corrections are negligible for the total cross sections, they can be relevant for some distributions such as transverse momentum and invariant mass distributions. We also found that for processes with final-state W bosons, there is an accidental cancelation between the negative virtual and positive photon-quark induced corrections. In practice, the strength of this cancelation depends on the photon PDF, which is very weakly constrained at present. To predict NLO EW corrections reliably, we therefore

need a precise determination of the photon PDF.

In all cases, the NLO QCD corrections are essential to reduce the scale uncertainties to below 10%, reaching the few percent level in VBF processes. By studying different scales, we clearly observe that LO uncertainties are larger than the one provided by a naive variation of the scales by a factor two around the central value, while NLO predictions agree well with one another. This effect is more dramatic in differential distributions where discrepancies up to a factor two are observed.

The size of the inclusive NLO corrections highly depends on the considered process and the number of jets. For processes with no or one jet at LO, the NLO contributions bring new partonic sub-processes, which can access the large gluonic PDFs, and also new phase-space regions which are logarithmically enhanced. This can not be captured by the LO scale uncertainty, which fails to predict the large K factor of these processes, highlighting the relevance of the NLO predictions. K factors typically range from 1.4 to 2 for the tri-boson production processes. Exceptionally large K factors of about 3 appear for $W\gamma\gamma$ production, which are driven by the suppression of the LO cross section due to a radiation zero. For multi-boson production processes with an accompanying jet, the NLO corrections are around 40%. Finally, for VBF Higgs production and di-boson production in association with two jets, both for the VBF and the QCD-induced production modes, the size of the NLO corrections range from a few percent up to 10%, when the LO scales are chosen in an optimal fashion. In these processes, all possible sub-processes appear already at LO, and thus the size of the NLO corrections is of the order of α_s. The only exception is the $W^\pm W^\pm jj$ production process, which first appears at this jet multiplicity. Hence, gluon-initiated processes open up at NLO, contributing to larger NLO corrections up to around 30% for the QCD-induced mechanism.

The NLO QCD corrections in general exhibit a non-trivial phase-space dependence in differential distributions. The size of the corrections highly depends on the observable and to some extent on the jet multiplicity of the process. In processes with zero or one jet at LO, the presence of additional jets as part of the real corrections allows for new kinematical configurations, where the jet recoils against some of the vector bosons, while the other vector bosons can be soft. This can result in logarithmically enhanced contributions in these phase-space regions. As a consequence, generally the re-scaling of the LO distributions by the total integrated K factor is imprecise and, thus, for precise measurements, not only the total cross section is needed at NLO, but also all the kinematical distributions. This is essential because unless the differential QCD corrections are properly included in experimental analyses, an excess in a particular region of the phase space when comparing with data could easily be misinterpreted as non-Standard Model physics.

Acknowledgments

It is a pleasure to thank K. Arnold, J. Baglio, J. Bellm, G. Bozzi, M. Brieg, C. Englert, B. Feigl, J. Frank, T. Figy, F. Geyer, N. Greiner, C. Hackstein, V. Hankele, B. Jäger, N. Kaiser, S. Kallweit, G. Klämke, M. Kubocz, D. T. Nhung, C. Oleari, S. Palmer, S. Plätzer, S. Prestel, H. Rzehak, F. Schissler, O. Schlimpert, M. Spannowsky, M. M. Weber, and M. Worek for their collaboration in the research presented in this chapter or in the development of the `VBFNLO` program. We would like to thank the Deutsche Forschungsgemeinschaft for their support of the SFB/TR-9 “Computational Particle Physics”.

References

[1] T. Figy, C. Oleari, D. Zeppenfeld, Next-to-leading order jet distributions for Higgs boson production via weak boson fusion, Phys.Rev. D68 (2003) 073005. arXiv:hep-ph/0306109, doi:10.1103/PhysRevD.68.073005.

[2] K. Arnold, M. Bahr, G. Bozzi, F. Campanario, C. Englert, et al., VBFNLO: A Parton level Monte Carlo for processes with electroweak bosons, Comput.Phys.Commun. 180 (2009) 1661–1670. arXiv:0811.4559, doi:10.1016/j.cpc.2009.03.006.

[3] J. Baglio, J. Bellm, F. Campanario, B. Feigl, J. Frank, et al., Release Note - VBFNLO 2.7.0, arXiv:1404.3940.

[4] S. Catani, M. Seymour, A General algorithm for calculating jet cross-sections in NLO QCD, Nucl.Phys. B485 (1997) 291–419. arXiv:hep-ph/9605323, doi:10.1016/S0550-3213(96)00589-5.

[5] B. Jager, C. Oleari, D. Zeppenfeld, Next-to-leading order QCD corrections to W+W- production via vector-boson fusion, JHEP 0607 (2006) 015. arXiv:hep-ph/0603177, doi:10.1088/1126-6708/2006/07/015.

[6] B. Jager, C. Oleari, D. Zeppenfeld, Next-to-leading order QCD corrections to Z boson pair production via vector-boson fusion, Phys.Rev. D73 (2006) 113006. arXiv:hep-ph/0604200, doi:10.1103/PhysRevD.73.113006.

[7] B. Jager, C. Oleari, D. Zeppenfeld, Next-to-leading order QCD corrections to W+ W+ jj and W- W- jj production via weak-boson fusion, Phys.Rev. D80 (2009) 034022. arXiv:0907.0580, doi:10.1103/PhysRevD.80.034022.

[8] G. Bozzi, B. Jager, C. Oleari, D. Zeppenfeld, Next-to-leading order QCD corrections to W+ Z and W- Z production via vector-boson fusion, Phys.Rev. D75 (2007) 073004. arXiv:hep-ph/0701105, doi:10.1103/PhysRevD.75.073004.

[9] A. Denner, L. Hosekova, S. Kallweit, NLO QCD corrections to W+ W+ jj production in vector-boson fusion at the LHC, Phys.Rev. D86 (2012) 114014. arXiv:1209.2389, doi:10.1103/PhysRevD.86.114014.

[10] F. Campanario, N. Kaiser, D. Zeppenfeld, $W\gamma$ production in vector boson fusion at NLO in QCD, Phys.Rev. D89 (2014) 014009. arXiv:1309.7259, doi:10.1103/PhysRevD.89.014009.

[11] T. Melia, K. Melnikov, R. Rontsch, G. Zanderighi, Next-to-leading order QCD predictions for W^+W^+jj production

at the LHC, JHEP 1012 (2010) 053. arXiv:1007.5313, doi:10.1007/JHEP12(2010)053.

[12] T. Melia, K. Melnikov, R. Rontsch, G. Zanderighi, NLO QCD corrections for W^+W^- pair production in association with two jets at hadron colliders, Phys.Rev. D83 (2011) 114043. arXiv:1104.2327, doi:10.1103/PhysRevD.83.114043.

[13] N. Greiner, G. Heinrich, P. Mastrolia, G. Ossola, T. Reiter, et al., NLO QCD corrections to the production of W+ W- plus two jets at the LHC, Phys.Lett. B713 (2012) 277–283. arXiv:1202.6004, doi:10.1016/j.physletb.2012.06.027.

[14] F. Campanario, M. Kerner, L. D. Ninh, D. Zeppenfeld, WZ Production in Association with Two Jets at Next-to-Leading Order in QCD, Phys.Rev.Lett. 111 (2013) 052003. arXiv:1305.1623, doi:10.1103/PhysRevLett.111.052003.

[15] F. Campanario, M. Kerner, L. D. Ninh, D. Zeppenfeld, Next-to-leading order QCD corrections to W^+W^+ and W^-W^- production in association with two jets, Phys.Rev. D89 (2014) 054009. arXiv:1311.6738, doi:10.1103/PhysRevD.89.054009.

[16] T. Gehrmann, N. Greiner, G. Heinrich, Precise QCD predictions for the production of a photon pair in association with two jets, Phys.Rev.Lett. 111 (2013) 222002. arXiv:1308.3660, doi:10.1103/PhysRevLett.111.222002.

[17] S. Badger, A. Guffanti, V. Yundin, Next-to-leading order QCD corrections to di-photon production in association with up to three jets at the Large Hadron Collider, JHEP 1403 (2014) 122. arXiv:1312.5927, doi:10.1007/JHEP03(2014)122.

[18] F. Campanario, M. Kerner, L. D. Ninh, D. Zeppenfeld, Next-to-leading order QCD corrections to $W\gamma$ production in association with two jets, Eur.Phys.J. C74 (2014) 2882. arXiv:1402.0505, doi:10.1140/epjc/s10052-014-2882-7.

[19] Z. Bern, L. Dixon, F. Febres Cordero, S. Hoeche, H. Ita, et al., Next-to-Leading Order Gamma Gamma + 2-Jet Production at the LHC, Phys.Rev. D90 (2014) 054004. arXiv:1402.4127, doi:10.1103/PhysRevD.90.054004.

[20] F. Campanario, M. Kerner, L. D. Ninh, D. Zeppenfeld, Next-to-leading order QCD corrections to ZZ production in association with two jets, JHEP 1407 (2014) 148. arXiv:1405.3972, doi:10.1007/JHEP07(2014)148.

[21] F. Campanario, M. Kerner, L. D. Ninh, D. Zeppenfeld, $Z\gamma$ production in association with two jets at next-to-leading order QCD, Eur.Phys.J. C74 (9) (2014) 3085. arXiv:1407.7857, doi:10.1140/epjc/s10052-014-3085-y.

[22] CMS Collaboration, Search for supersymmetry in events with photons and missing energy.

[23] The ATLAS Collaboration, Search for Diphoton Events with Large Missing Transverse Momentum in 8 TeV pp Collision Data with the ATLAS Detector.

[24] V. Hankele, D. Zeppenfeld, QCD corrections to hadronic WWZ production with leptonic decays, Phys.Lett. B661 (2008) 103–108. arXiv:0712.3544, doi:10.1016/j.physletb.2008.02.014.

[25] F. Campanario, V. Hankele, C. Oleari, S. Prestel, D. Zeppenfeld, QCD corrections to charged triple vector boson production with leptonic decay, Phys.Rev. D78 (2008) 094012. arXiv:0809.0790, doi:10.1103/PhysRevD.78.094012.

[26] G. Bozzi, F. Campanario, V. Hankele, D. Zeppenfeld, NLO QCD corrections to W+W- gamma and Z Z gamma production with leptonic decays, Phys.Rev. D81 (2010) 094030. arXiv:0911.0438, doi:10.1103/PhysRevD.81.094030.

[27] G. Bozzi, F. Campanario, M. Rauch, H. Rzehak, D. Zeppenfeld, NLO QCD corrections to $W^\pm Z\gamma$ production with leptonic decays, Phys.Lett. B696 (2011) 380–385. arXiv:1011.2206, doi:10.1016/j.physletb.2010.12.051.

[28] G. Bozzi, F. Campanario, M. Rauch, D. Zeppenfeld, $W^{+-}\gamma\gamma$ production with leptonic decays at NLO QCD, Phys.Rev. D83 (2011) 114035. arXiv:1103.4613, doi:10.1103/PhysRevD.83.114035.

[29] G. Bozzi, F. Campanario, M. Rauch, D. Zeppenfeld, $Z\gamma\gamma$ production with leptonic decays and triple photon production at next-to-leading order QCD, Phys.Rev. D84 (2011) 074028. arXiv:1107.3149, doi:10.1103/PhysRevD.84.074028.

[30] B. Feigl, Electroweak Processes in the Standard Model and Beyond: Backgrounds to Higgs Physics and Semileptonic Decay Modes, Ph.D. thesis, KIT, Karlsruhe (2013).

[31] F. Campanario, R. Roth, D. Zeppenfeld, QCD radiation in WH and WZ production and anomalous coupling measurements, arXiv:1410.4840.

[32] F. Campanario, M. Rauch, S. Sapeta, W^+W^- production at high transverse momenta beyond NLO, Nucl.Phys. B879 (2014) 65–79. arXiv:1309.7293, doi:10.1016/j.nuclphysb.2013.12.001.

[33] F. Campanario, C. Englert, S. Kallweit, M. Spannowsky, D. Zeppenfeld, NLO QCD corrections to WZ+jet production with leptonic decays, JHEP 1007 (2010) 076. arXiv:1006.0390, doi:10.1007/JHEP07(2010)076.

[34] F. Campanario, C. Englert, M. Spannowsky, QCD corrections to non-standard WZ+jet production with leptonic decays at the LHC, Phys.Rev. D82 (2010) 054015. arXiv:1006.3090, doi:10.1103/PhysRevD.82.054015.

[35] F. Campanario, C. Englert, M. Spannowsky, D. Zeppenfeld, NLO-QCD corrections to W gamma j production, Europhys.Lett. 88 (2009) 11001. arXiv:0908.1638, doi:10.1209/0295-5075/88/11001.

[36] F. Campanario, C. Englert, M. Spannowsky, Precise predictions for (non-standard) $W\gamma$ + jet production, Phys.Rev. D83 (2011) 074009. arXiv:1010.1291, doi:10.1103/PhysRevD.83.074009.

[37] F. Campanario, C. Englert, M. Rauch, D. Zeppenfeld, Precise predictions for $W\gamma\gamma$ +jet production at hadron colliders, Phys.Lett. B704 (2011) 515–519. arXiv:1106.4009, doi:10.1016/j.physletb.2011.09.072.

[38] S. Chatrchyan, et al., Search for the standard model Higgs boson produced in association with a W or a Z boson and decaying to bottom quarks, Phys.Rev. D89 (1) (2014) 012003. arXiv:1310.3687, doi:10.1103/PhysRevD.89.012003.

[39] G. Aad, et al., Search for the $b\bar{b}$ decay of the Standard Model Higgs boson in associated $(W/Z)H$ production with the ATLAS detector, arXiv:1409.6212.

[40] J. Butterworth, G. Dissertori, S. Dittmaier, D. de Florian, N. Glover, et al., Les Houches 2013: Physics at TeV Colliders: Standard Model Working Group Report, arXiv:1405.1067.

[41] J. Baglio, L. D. Ninh, M. M. Weber, Massive gauge boson pair production at the LHC: a next-to-leading order story, Phys.Rev. D88 (2013) 113005. arXiv:1307.4331, doi:10.1103/PhysRevD.88.113005.

[42] D. T. Nhung, L. D. Ninh, M. M. Weber, NLO corrections to WWZ production at the LHC, JHEP 1312 (2013) 096. arXiv:1307.7403, doi:10.1007/JHEP12(2013)096.

[43] A. Bierweiler, T. Kasprzik, J. H. Kühn, S. Uccirati, Electroweak corrections to W-boson pair production at the LHC, JHEP 1211 (2012) 093. arXiv:1208.3147, doi:10.1007/JHEP11(2012)093.

[44] A. Bierweiler, T. Kasprzik, J. H. Kühn, Vector-boson pair production at the LHC to $O(\alpha^3)$ accuracy, JHEP 1312 (2013) 071. arXiv:1305.5402, doi:10.1007/JHEP12(2013)071.

[45] M. Billoni, S. Dittmaier, B. Jäger, C. Speckner, Next-to-leading order electroweak corrections to $pp \to W^+W^- \to 4$ leptons at the LHC in double-pole approximation, JHEP 1312 (2013) 043. arXiv:1310.1564, doi:10.1007/JHEP12(2013)043.

[46] K. Hagiwara, D. Zeppenfeld, Helicity Amplitudes for Heavy Lepton Production in e+ e- Annihilation, Nucl.Phys. B274 (1986) 1–32. doi:10.1016/0550-3213(86)90615-2.

[47] K. Hagiwara, D. Zeppenfeld, Amplitudes for Multiparton Processes Involving a Current at e+ e-, e+- p, and Hadron Col-

liders, Nucl.Phys. B313 (1989) 560–594. doi:10.1016/0550-3213(89)90397-0.

[48] H. Murayama, I. Watanabe, K. Hagiwara, HELAS: HELicity amplitude subroutines for Feynman diagram evaluations, .

[49] A. Denner, S. Dittmaier, M. Roth, D. Wackeroth, Predictions for all processes $e^+e^- \to$ 4fermions + γ, Nucl.Phys. B560 (1999) 33–65. arXiv:hep-ph/9904472, doi:10.1016/S0550-3213(99)00437-X.

[50] C. Englert, B. Jager, D. Zeppenfeld, QCD Corrections to Vector-Boson Fusion Processes in Warped Higgsless Models, JHEP 0903 (2009) 060. arXiv:0812.2564, doi:10.1088/1126-6708/2009/03/060.

[51] J. Frank, M. Rauch, D. Zeppenfeld, Spin-2 Resonances in Vector-Boson-Fusion Processes at NLO QCD, Phys.Rev. D87 (2013) 055020. arXiv:1211.3658, doi:10.1103/PhysRevD.87.055020.

[52] J. Frank, M. Rauch, D. Zeppenfeld, Higgs Spin Determination in the WW channel and beyond, Eur.Phys.J. C74 (2014) 2918. arXiv:1305.1883, doi:10.1140/epjc/s10052-014-2918-z.

[53] F. Campanario, Towards pp → VVjj at NLO QCD: Bosonic contributions to triple vector boson production plus jet, JHEP 1110 (2011) 070. arXiv:1105.0920, doi:10.1007/JHEP10(2011)070.

[54] G. Passarino, M. Veltman, One Loop Corrections for e+ e- Annihilation Into mu+ mu- in the Weinberg Model, Nucl.Phys. B160 (1979) 151. doi:10.1016/0550-3213(79)90234-7.

[55] A. Denner, S. Dittmaier, Reduction schemes for one-loop tensor integrals, Nucl.Phys. B734 (2006) 62–115. arXiv:hep-ph/0509141, doi:10.1016/j.nuclphysb.2005.11.007.

[56] G. P. Lepage, A New Algorithm for Adaptive Multidimensional Integration, J.Comput.Phys. 27 (1978) 192. doi:10.1016/0021-9991(78)90004-9.

[57] S. Frixione, Isolated photons in perturbative QCD, Phys.Lett. B429 (1998) 369–374. arXiv:hep-ph/9801442, doi:10.1016/S0370-2693(98)00454-7.

[58] W. Buchmuller, D. Wyler, Effective Lagrangian Analysis of New Interactions and Flavor Conservation, Nucl.Phys. B268 (1986) 621–653. doi:10.1016/0550-3213(86)90262-2.

[59] K. Hagiwara, S. Ishihara, R. Szalapski, D. Zeppenfeld, Low-energy effects of new interactions in the electroweak boson sector, Phys.Rev. D48 (1993) 2182–2203. doi:10.1103/PhysRevD.48.2182.

[60] B. Grzadkowski, M. Iskrzynski, M. Misiak, J. Rosiek, Dimension-Six Terms in the Standard Model Lagrangian, JHEP 1010 (2010) 085. arXiv:1008.4884, doi:10.1007/JHEP10(2010)085.

[61] K. Arnold, J. Bellm, G. Bozzi, M. Brieg, F. Campanario, et al., VBFNLO: A Parton Level Monte Carlo for Processes with Electroweak Bosons – Manual for Version 2.5.0, arXiv:1107.4038.

[62] VBFNLO utility to calculate form factors, version 1.3.0. URL `https://www.itp.kit.edu/~vbfnloweb/wiki/doku.php?id=download:formfactor`

[63] S. Catani, Y. L. Dokshitzer, M. Seymour, B. Webber, Longitudinally invariant K_t clustering algorithms for hadron hadron collisions, Nucl.Phys. B406 (1993) 187–224. doi:10.1016/0550-3213(93)90166-M.

[64] S. D. Ellis, D. E. Soper, Successive combination jet algorithm for hadron collisions, Phys.Rev. D48 (1993) 3160–3166. arXiv:hep-ph/9305266, doi:10.1103/PhysRevD.48.3160.

[65] C. Oleari, D. Zeppenfeld, QCD corrections to electroweak nu(l) j j and l+ l- j j production, Phys.Rev. D69 (2004) 093004. arXiv:hep-ph/0310156, doi:10.1103/PhysRevD.69.093004.

[66] T. Figy, V. Hankele, D. Zeppenfeld, Next-to-leading order QCD corrections to Higgs plus three jet production in vector-boson fusion, JHEP 0802 (2008) 076. arXiv:0710.5621, doi:10.1088/1126-6708/2008/02/076.

[67] T. Figy, Next-to-leading order QCD corrections to light Higgs Pair production via vector boson fusion, Mod.Phys.Lett. A23 (2008) 1961–1973. arXiv:0806.2200, doi:10.1142/S0217732308028181.

[68] K. Arnold, T. Figy, B. Jager, D. Zeppenfeld, Next-to-leading order QCD corrections to Higgs boson production in association with a photon via weak-boson fusion at the LHC, JHEP 1008 (2010) 088. arXiv:1006.4237, doi:10.1007/JHEP08(2010)088.

[69] J. Baglio, A. Djouadi, R. Grber, M. Mhlleitner, J. Quevillon, et al., The measurement of the Higgs self-coupling at the LHC: theoretical status, JHEP 1304 (2013) 151. arXiv:1212.5581, doi:10.1007/JHEP04(2013)151.

[70] M. Ciccolini, A. Denner, S. Dittmaier, Strong and electroweak corrections to the production of Higgs + 2jets via weak interactions at the LHC, Phys.Rev.Lett. 99 (2007) 161803. arXiv:0707.0381, doi:10.1103/PhysRevLett.99.161803.

[71] M. Ciccolini, A. Denner, S. Dittmaier, Electroweak and QCD corrections to Higgs production via vector-boson fusion at the LHC, Phys.Rev. D77 (2008) 013002. arXiv:0710.4749, doi:10.1103/PhysRevD.77.013002.

[72] T. Figy, S. Palmer, G. Weiglein, Higgs Production via Weak Boson Fusion in the Standard Model and the MSSM, JHEP 1202 (2012) 105. arXiv:1012.4789, doi:10.1007/JHEP02(2012)105.

[73] P. Bolzoni, F. Maltoni, S.-O. Moch, M. Zaro, Higgs production via vector-boson fusion at NNLO in QCD, Phys.Rev.Lett. 105 (2010) 011801. arXiv:1003.4451, doi:10.1103/PhysRevLett.105.011801.

[74] P. Bolzoni, F. Maltoni, S.-O. Moch, M. Zaro, Vector boson fusion at NNLO in QCD: SM Higgs and beyond, Phys.Rev. D85 (2012) 035002. arXiv:1109.3717, doi:10.1103/PhysRevD.85.035002.

[75] J. Pumplin, D. Stump, J. Huston, H. Lai, P. M. Nadolsky, et al., New generation of parton distributions with uncertainties from global QCD analysis, JHEP 0207 (2002) 012. arXiv:hep-ph/0201195, doi:10.1088/1126-6708/2002/07/012.

[76] H.-L. Lai, M. Guzzi, J. Huston, Z. Li, P. M. Nadolsky, et al., New parton distributions for collider physics, Phys.Rev. D82 (2010) 074024. arXiv:1007.2241, doi:10.1103/PhysRevD.82.074024.

[77] J. M. Campbell, R. K. Ellis, Next-to-leading order corrections to W^+ 2 jet and Z^+ 2 jet production at hadron colliders, Phys.Rev. D65 (2002) 113007. arXiv:hep-ph/0202176, doi:10.1103/PhysRevD.65.113007.

[78] G. Aad, et al., Evidence for Electroweak Production of $W^\pm W^\pm jj$ in pp Collisions at $\sqrt{s} = 8$ TeV with the ATLAS Detector, Phys.Rev.Lett. 113 (2014) 141803. arXiv:1405.6241, doi:10.1103/PhysRevLett.113.141803.

[79] V. Khachatryan, et al., Study of vector boson scattering and search for new physics in events with two same-sign leptons and two jets, arXiv:1410.6315.

[80] A. Martin, W. Stirling, R. Thorne, G. Watt, Parton distributions for the LHC, Eur.Phys.J. C63 (2009) 189–285. arXiv:0901.0002, doi:10.1140/epjc/s10052-009-1072-5.

[81] M. Cacciari, G. P. Salam, G. Soyez, The Anti-k(t) jet clustering algorithm, JHEP 0804 (2008) 063. arXiv:0802.1189, doi:10.1088/1126-6708/2008/04/063.

[82] A. Lazopoulos, K. Melnikov, F. Petriello, QCD corrections to tri-boson production, Phys.Rev. D76 (2007) 014001. arXiv:hep-ph/0703273, doi:10.1103/PhysRevD.76.014001.

[83] T. Binoth, G. Ossola, C. Papadopoulos, R. Pittau, NLO QCD corrections to tri-boson production, JHEP 0806 (2008) 082. arXiv:0804.0350, doi:10.1088/1126-6708/2008/06/082.

[84] U. Baur, D. Wackeroth, M. M. Weber, Radiative corrections to W gamma gamma production at the LHC, PoS RADCOR2009 (2010) 067. arXiv:1001.2688.

[85] C. Chen, W.-G. Ma, R.-Y. Zhang, Y. Zhang, L.-W. Chen, et al., Electroweak radiative corrections to $W^+W^-\gamma$ production at the ILC, Eur.Phys.J. C74 (11) (2014) 3166. arXiv:1409.4900, doi:10.1140/epjc/s10052-014-3166-y.

[86] I. W. Stewart, F. J. Tackmann, Theory Uncertainties for Higgs and Other Searches Using Jet Bins, Phys.Rev. D85 (2012) 034011. arXiv:1107.2117, doi:10.1103/PhysRevD.85.034011.

[87] R. W. Brown, K. Kowalski, S. J. Brodsky, Classical Radiation Zeros in Gauge Theory Amplitudes, Phys.Rev. D28 (1983) 624. doi:10.1103/PhysRevD.28.624.

[88] U. Baur, T. Han, J. Ohnemus, QCD corrections to hadronic $W\gamma$ production with nonstandard $WW\gamma$ couplings, Phys.Rev. D48 (1993) 5140–5161. arXiv:hep-ph/9305314, doi:10.1103/PhysRevD.48.5140.

[89] U. Baur, T. Han, N. Kauer, R. Sobey, D. Zeppenfeld, $W\gamma\gamma$ production at the Fermilab Tevatron collider: Gauge invariance and radiation amplitude zero, Phys.Rev. D56 (1997) 140–150. arXiv:hep-ph/9702364, doi:10.1103/PhysRevD.56.140.

[90] M. Dobbs, Prospects for probing triple gauge-boson couplings at the LHC, AIP Conf.Proc. 753 (2005) 181–192. arXiv:hep-ph/0506174, doi:10.1063/1.1896700.

[91] V. Del Duca, F. Maltoni, Z. Nagy, Z. Trocsanyi, QCD radiative corrections to prompt diphoton production in association with a jet at hadron colliders, JHEP 0304 (2003) 059. arXiv:hep-ph/0303012, doi:10.1088/1126-6708/2003/04/059.

[92] S. Dittmaier, S. Kallweit, P. Uwer, NLO QCD corrections to WW+jet production at hadron colliders, Phys.Rev.Lett. 100 (2008) 062003. arXiv:0710.1577, doi:10.1103/PhysRevLett.100.062003.

[93] J. M. Campbell, R. K. Ellis, G. Zanderighi, Next-to-leading order predictions for WW + 1 jet distributions at the LHC, JHEP 0712 (2007) 056. arXiv:0710.1832, doi:10.1088/1126-6708/2007/12/056.

[94] S. Dittmaier, S. Kallweit, P. Uwer, NLO QCD corrections to pp/ppbar → WW+jet+X including leptonic W-boson decays, Nucl.Phys. B826 (2010) 18–70. arXiv:0908.4124, doi:10.1016/j.nuclphysb.2009.09.029.

[95] T. Binoth, T. Gleisberg, S. Karg, N. Kauer, G. Sanguinetti, NLO QCD corrections to ZZ+ jet production at hadron colliders, Phys.Lett. B683 (2010) 154–159. arXiv:0911.3181, doi:10.1016/j.physletb.2009.12.013.

[96] T. Melia, K. Melnikov, R. Rontsch, M. Schulze, G. Zanderighi, Gluon fusion contribution to W+W- + jet production, JHEP 1208 (2012) 115. arXiv:1205.6987, doi:10.1007/JHEP08(2012)115.

[97] F. Campanario, Q. Li, M. Rauch, M. Spira, ZZ+jet production via gluon fusion at the LHC, JHEP 1306 (2013) 069. arXiv:1211.5429, doi:10.1007/JHEP06(2013)069.

[98] J. M. Campbell, H. B. Hartanto, C. Williams, Next-to-leading order predictions for $Z\gamma$+jet and Z $\gamma\gamma$ final states at the LHC, JHEP 1211 (2012) 162. arXiv:1208.0566, doi:10.1007/JHEP11(2012)162.

[99] P. Agrawal, A. Shivaji, Di-Vector Boson + Jet Production via Gluon Fusion at Hadron Colliders, Phys.Rev. D86 (2012) 073013. arXiv:1207.2927, doi:10.1103/PhysRevD.86.073013.

[100] P. Agrawal, A. Shivaji, Production of γZg and associated processes via gluon fusion at hadron colliders, JHEP 1301 (2013) 071. arXiv:1208.2593, doi:10.1007/JHEP01(2013)071.

[101] T. Gehrmann, N. Greiner, G. Heinrich, Photon isolation effects at NLO in $\gamma\gamma$ + jet final states in hadronic collisions, JHEP 1306 (2013) 058. arXiv:1303.0824, doi:10.1007/JHEP06(2014)076, 10.1007/JHEP06(2013)058.

[102] J. Baglio, L. D. Ninh, M. M. Weber, Full NLO massive gauge boson pair production at the LHC, arXiv:1310.3972.

[103] S. Dittmaier, A General approach to photon radiation off fermions, Nucl.Phys. B565 (2000) 69–122. arXiv:hep-ph/9904440, doi:10.1016/S0550-3213(99)00563-5.

[104] T. Hahn, Generating Feynman diagrams and amplitudes with FeynArts 3, Comput.Phys.Commun. 140 (2001) 418–431. arXiv:hep-ph/0012260, doi:10.1016/S0010-4655(01)00290-9.

[105] T. Hahn, M. Perez-Victoria, Automatized one loop calculations in four-dimensions and D-dimensions, Comput.Phys.Commun. 118 (1999) 153–165. arXiv:hep-ph/9807565, doi:10.1016/S0010-4655(98)00173-8.

[106] M. M. Weber, private communication.

[107] G. van Oldenborgh, FF: A Package to evaluate one loop Feynman diagrams, Comput.Phys.Commun. 66 (1991) 1–15. doi:10.1016/0010-4655(91)90002-3.

[108] T. Hahn, M. Rauch, News from FormCalc and LoopTools, Nucl.Phys.Proc.Suppl. 157 (2006) 236–240. arXiv:hep-ph/0601248, doi:10.1016/j.nuclphysbps.2006.03.026.

[109] J. Alwall, P. Demin, S. de Visscher, R. Frederix, M. Herquet, et al., MadGraph/MadEvent v4: The New Web Generation, JHEP 0709 (2007) 028. arXiv:0706.2334, doi:10.1088/1126-6708/2007/09/028.

[110] A. Martin, R. Roberts, W. Stirling, R. Thorne, Parton distributions incorporating QED contributions, Eur.Phys.J. C39 (2005) 155–161. arXiv:hep-ph/0411040, doi:10.1140/epjc/s2004-02088-7.

[111] B. Mele, P. Nason, G. Ridolfi, QCD radiative corrections to Z boson pair production in hadronic collisions, Nucl.Phys. B357 (1991) 409–438. doi:10.1016/0550-3213(91)90475-D.

[112] J. Ohnemus, J. Owens, An Order $\alpha^- s$ calculation of hadronic ZZ production, Phys.Rev. D43 (1991) 3626–3639. doi:10.1103/PhysRevD.43.3626.

[113] J. Ohnemus, An Order $\alpha^- s$ calculation of hadronic $W^\pm Z$ production, Phys.Rev. D44 (1991) 3477–3489. doi:10.1103/PhysRevD.44.3477.

[114] S. Frixione, P. Nason, G. Ridolfi, Strong corrections to W Z production at hadron colliders, Nucl.Phys. B383 (1992) 3–44. doi:10.1016/0550-3213(92)90668-2.

[115] S. Frixione, A Next-to-leading order calculation of the cross-section for the production of W+ W- pairs in hadronic collisions, Nucl.Phys. B410 (1993) 280–324. doi:10.1016/0550-3213(93)90435-R.

[116] J. Ohnemus, Hadronic ZZ, W^-W^+, and $W^\pm Z$ production with QCD corrections and leptonic decays, Phys.Rev. D50 (1994) 1931–1945. arXiv:hep-ph/9403331, doi:10.1103/PhysRevD.50.1931.

[117] T. Corbett, O. Eboli, J. Gonzalez-Fraile, M. Gonzalez-Garcia, Robust Determination of the Higgs Couplings: Power to the Data, Phys.Rev. D87 (2013) 015022. arXiv:1211.4580, doi:10.1103/PhysRevD.87.015022.

[118] E. Masso, V. Sanz, Limits on Anomalous Couplings of the Higgs to Electroweak Gauge Bosons from LEP and LHC, Phys.Rev. D87 (3) (2013) 033001. arXiv:1211.1320, doi:10.1103/PhysRevD.87.033001.

[119] S. Schael, et al., Electroweak Measurements in Electron-Positron Collisions at W-Boson-Pair Energies at LEP, Phys.Rept. 532 (2013) 119–244. arXiv:1302.3415, doi:10.1016/j.physrep.2013.07.004.

[120] V. Hankele, G. Klamke, D. Zeppenfeld, T. Figy, Anomalous Higgs boson couplings in vector boson fusion at the CERN LHC, Phys.Rev. D74 (2006) 095001. arXiv:hep-ph/0609075, doi:10.1103/PhysRevD.74.095001.